Peter Fürk, BSc

01430509

Enhancing the Permittivity of Perylene-Linker-Perylene Acceptors for Application in Organic Solar Cells

MASTER'S THESIS

to achieve the university degree of

Diplom-Ingenieur

Master's degree programme: Technical Chemistry

submitted to

Graz University of Technology

Supervisor

Univ.-Prof. Dipl.-Ing. Dr.techn. Gregor Trimmel

Institute for Chemistry and Technology of Materials

Graz, February 2020

Affidavit

I declare that I have authored this thesis independently, that I have not used other than the declared sources/resources, and that I have explicitly indicated all material which has been quoted either literally or by content from the sources used. The text document uploaded to TUGRAZonline is identical to the present master's thesis.

Ich erkläre an Eides statt, dass ich die vorliegende Arbeit selbstständig verfasst, andere als die angegebenen Quellen/Hilfsmittel nicht benutzt, und die den benutzten Quellen wörtlich und inhaltlich entnommenen Stellen als solche kenntlich gemacht habe. Das in TUGRAZonline hochgeladene Textdokument ist mit der vorliegenden Masterarbeit identisch.

Date Signature

Acknowledgements

I would like to say thanks to my supervisor, Professor Gregor Trimmel, for offering me this position in the institute and making it possible to write my thesis in this interesting field. Within the department, I thank all my colleagues, who supported me with insights, practical help and the one or other motivation boost in form of a well placed coffee break. Especially, I want to thank Dr. Matiss Reinfels and Dipl.Ing. Stefan Weber, for sharing their greater experience in the field of organic synthetic chemistry and organic solar cells.

Besides my working group, I thank Dr. Petra Kaschnitz, Ing. Josefine Hobisch, Ing. Karin Bartl and Dr. Thomas Rath, for helping me with measurements and their subsequent interpretation.

Outside university, I would like to thank my friends, who helped me recharge batteries by taking my mind off the thesis in my spare time. And last but not least, I thank my family, for their untiring support. For all the kind words, patient listening and food packages, I want to say: Danke, Mutti und Vati!

Abstract

A major difference between organic solar cells (OSC) and their inorganic counterpart, is the significantly lower permittivity ε of the used organic semiconductor materials. This leads, inter alia, to limited current densities and thus limited performances of OSCs. Major improvement steps to diminish these limitations are the combination of two materials, an electron donor and electron acceptor, and mixing them in a bulk-heterojunction. This already greatly enhances charge carrier extraction and thus the achievable current densities. However, finding ways to increase ε could enable even higher performances. Therefore, raising ε was attempted in this work.

Herein, new acceptor materials for organic solar cells were prepared. They were designed with acceptor-donor-acceptor (A-D-A) structure, comprising fluorene or carbazole as donor/linker and *N*-(2,6-diisopropylphenyl) perylene monoimide (PMI) as acceptor. The linkers were altered by introduction of polar side chains 2-(2-(ethoxy)ethoxy)ethyl (DEG) and 2,2,3,3,4,4,5,5,6,6,7,7,8,8,8-pentadecafluorooctyl ($\mathrm{Oct_F}$(2H)). This should lead to an increase of the compound's permittivity. Three A-D-A molecules were successfully synthesized, PMI-F(DEG)-PMI, PMI-C(DEG)-PMI and PMI-C($\mathrm{Oct_F}$(2H))-PMI. They were characterized by NMR spectroscopy and high-resolution mass spectrometry. Futhermore, their optical and thermal properties were determined. In parallel, the geometric and optic properties of the A-D-A molecules were calculated with density functional theory methods (Gaussian09). Two compounds, PMI-F(DEG)-PMI and PMI-C(DEG)-PMI, were applied in bulk heterojunctions together with PBDB-T as donor polymer in OSCs. Their performance was determined by current-voltage and quantum yield measurements. Furthermore, the crystallinity and miscibility behaviour of the acceptors in pure and bulk heterojunction films was examined.

Both tested acceptors worked in OSCs. The PMI-F(DEG)-PMI cells achieved a power conversion efficiency (PCE) of $0.9 - 1.2$ %, which slightly increased after light soaking. PMI-C(DEG)-PMI cells reached $1.4 - 2.0$ %, which increased after both, light soaking and annealing up to 3.92 %. The synthetic routes can be further improved, since all products were usually obtained in low yields. Characterization of their electric properties is still ongoing.

Zusammenfassung

Ein wesentlicher Unterschied zwischen organischen und anorganischen Solarzellen ist die signifikant niedrigere Permittivität ε der organischen Halbleiter. Das führt unter anderem zu limitierten Stromdichten und folglich limitierten Effizienzen von organischen Photovoltaikzellen. Bedeutende Verbesserungen, um diese Einschränkungen zu verringern, sind die Kombination zweier Materialien, eines Elektronendonors und -akzeptors, in einer Bulk-Heterojunction. Das verbessert die Ladungsträgerextraktion bereits sehr, und folglich die erreichbaren Stromdichten. Wege, ε zu erhöhen, könnten jedoch noch höhere Effizienzen ermöglichen. Deshalb wurde in dieser Arbeit versucht, ε zu steigern.

In dieser Arbeit wurden neue Akzeptoren für organische Solarzellen entwickelt. Sie wurden mit Akzeptor-Donor-Akzeptor (A-D-A) Struktur entworfen, bestehend aus Fluoren oder Carbazol als Donor/Linker und *N*-(2,6-Diisopropylphenyl)perylenmonoimid (PMI) als Akzeptor. Die Linker wurde durch Einführung von polaren Seitenketten 2-(2-(Ethoxy)ethoxy)ethyl (DEG) und 2,2,3,3,4,4,5,5,6,6,7,7,8,8,8-pentadecafluorooctyl ($\mathrm{Oct_F(2H)}$) variiert. Das soll die Permittivität der Stoffe erhöhen. Drei A-D-A Moleküle wurden erfolgreich hergestellt, PMI-F(DEG)-PMI, PMI-C(DEG)-PMI and PMI-C($\mathrm{Oct_F(2H)}$)-PMI, charakterisiert mittels NMR Spektroskopie und Hochauflösungs-Massenspektrometrie. Weiters wurden ihre optischen und thermischen Eigenschaften bestimmt. Nebenbei wurden die geometrischen und optischen Eigenschaften der A-D-A Moleküle mittels Dichtefunktionaltheorie (Gaussian09) berechnet. Zwei Stoffe, PMI-F(DEG)-PMI und PMI-C(DEG)-PMI, wurden zusammen mit PBDB-T als Donor-Polymer in Bulk-Heterojunctions in Solarzellen verbaut. Ihre Leistung wurde mittels Strom-Spannungs- und Quanteneffizienzmessungen bestimmt. Des Weiteren wurden Kristallinität und Mischungsverhalten der Akzeptoren in Rein- und Bulk-Heterojunction-Dünnfilmen untersucht.

Beide Akzeptoren funktionierten in Solarzellen. Die PMI-F(DEG)-PMI Zellen erreichten eine PCE von $0.9 - 1.2$ %, die sich nach Light-Soaking leicht verbesserte. PMI-C(DEG)-PMI Zellen erzielten $1.4 - 2.0$ %, was sich nach sowohl Light-Soaking, als auch Tempern auf bis zu 3.92 % verbesserte. Da bei allen Produkten niedrige Ausbeuten erzielt wurden, könnten die Syntheserouten noch weiters optimiert werden.

Contents

List of Figures

List of Tables

Abbreviations

A-D-A	acceptor-donor-acceptor
AM	air mass
BHJ	bulk heterojunction
CB	chlorobenzene
DEG-OH	2-(2-(ethoxy)ethoxy)ethan-1-ol
ECD	electronic circuit diagram
ETL	electron transport layer
EQE	external quantum efficiency
FF	fill factor
HTL	hole transport layer
J_{mpp}	current density at maximum power point
J_{sc}	short-circuit current density
MPP	maximum power point
MS	mass spectrometry
NFA	non-fullerene acceptor
Oct_F(2H)-OH	2,2,3,3,4,4,5,5,6,6,7,7,8,8,8-pentadecafluorooctan-1-ol
Oct_F(4H)-I	1,1,1,2,2,3,3,4,4,5,5,6,6-tridecafluoro-8-iodooctane
OPV	organic photovoltaics
OSC	organic solar cell
PCE	power conversion efficiency
PBDB-T	Poly[[4,8-bis[5-(2-ethylhexyl)-2-thienyl]benzo[1,2-b:4,5-b´]dithiophene-2,6-diyl]-2,5-thiophenediyl[5,7-bis(2-ethylhexyl)-4,8-dioxo-4H,8H-benzo[1,2-c:4,5-c´]dithiophene-1,3-diyl]] polymer
PV	photovoltaics
SC	solar cell
RT	room temperature
TBAB	tetrabutyl ammoniumbromide
TEG_F-OH	2,2-difluoro-2-(1,1,2,2-tetrafluoro-2-(1,1,2,2-tetrafluoro-2-(trifluoromethoxy)ethoxy)ethoxy)ethan-1-ol
THF	tetrahydrofuran
TLC	thin layer chromatograph / chromatogramm
V_{mpp}	voltage at maximum power point
V_{oc}	open-circuit voltage

1 Introduction

The direct generation of electric energy from sunlight is an attractive concept. It has no necessity for detours, pre- or post-transformations. Thus, no high apparative effort is necessary like e.g. in hydropower plants. Also, reducing the amount of energy conversion steps lowers the number of possible loss contributors. This makes photovoltaics (PV) an interesting option for electric energy production.

The evolution of photovoltaic cells goes back to the 19th century with the experimental observation of the photovoltaic effect by Alexandre Edmond Becquerel in 1839.[1] Over a century later, in 1954, the first silicon based solar battery was built at Bell laboratories.[2] Another leap was the creation of the first dye-sensitized solar cell (SC) by Grätzel *et al.* in 1988. This for the first time introduced organic molecules to PV cells.[3] Today, the diverse field of photovoltaic technologies is often divided into three generations. The first consists of mono- and polycrystalline silicon SCs, the second includes amorphous silicon and other thin film technologies while the latest, generation three, consists of emerging PV technologies, including organic solar cells.[4][5]

Organic photovoltaic (OPV) cells are highly interesting because they can potentially be mass produced via roll-to-roll processes, can be designed flexible, light-weight and semi-transparent.[5][6][7] This would be an attractive alternative to the heavier and rigid silicon based PV cells. To really make OSCs a serious alternative to silicon PV cells, high efforts have been put into increasing their performances over the last decades. Today, power conversion efficiencies (PCE) of over 16 % have been reported by Cui *et al.*, making OPVs a competitive technology.[6] The best certified efficiency is currently being held with 17.4 %(state January 2020).[8]

A major difference between the conventional inorganic and organic semiconductors is the magnitude of their permittivity ε. Their relative permittivities ε_r often lie in a range of 3-4 [9], which is significantly lower than for inorganic semiconductors (ε_r $10 - 15$).[10] This leads to high exciton binding energies, short exciton diffusion lengths ($\sim$10 nm) and short exciton lifetimes ($\sim$1 ns), which cause a high recombination rate of charge carriers.[11] The high exciton recombination losses then lower the fill factor FF and short-circuit voltage J_{sc} of the

OSC.[11] To overcome these limitations, early solar cells were limited to be produced with thin active layers, so a bigger fraction of excitons could reach the separating donor-acceptor interface within their lifetimes. However, the thin layers limit the achievable light absorption. A big improvement step was the development of the first bulk heterojunction solar cell, introduced by Hiramoto *et al.* Intermixing the donor and acceptor materials to forme fine, interwebed structures, led to a higher interface area and shorter pathlengths, resulting in more excitons reaching the dissociation site. This instantly doubled the photocurrent compared to the bilayer PV cell with the same materials.[12]

Despite these improvements, the short exciton diffusion lengths are still a limiting factor. In 2012, Koster *et al.* suggested the permittivity ε as a central parameter for efficient solar cells. The use it as pathway to identify ways towards solar cells with PCEs of over 20 %.[13] Increasing ε could have a wide-ranging influence on many processes within the solar cell, e.g. reduction of exciton binding energy[14] and bimolecular[15] and trap-assisted[16] recombinations.

Regarding material development, a prominent research topic in the last decades was the use of fullerenes as acceptor material in OSCs. In 1995, Hummelen *et al.* presented the first bulk heterojunction solar cell comprising fullerenes. It was built from a blend of an organic semiconducting polymer as donor and fullerenes as acceptor. They reached a PCE of 2.9 %, which was by 2 orders of magnitude higher than when using the donor alone at the investigated wavelength of 430 nm.[17] From then on, the interest in fullerene solar cells increased significantly. Dang *et al.* have counted the number of publications with the material combination P3HT:PCBM between 2002 and 2010 to be 1033, which reflects their popularity.[18] This is, amongst other reasons, due to their good charge transport properties.[19] An innovative approach was shown by Yan *et al.*, who used a template-assisted strategy to build active layers with vertically aligned fullerenes. That way they achieved a PCE of 7.3 % with a P3HT:fullerene blend.[20][21] The currently highest performance (status 2017) for fullerene-based OSCs was produced by Heliatek in 2013, who reached a PCE of $\sim$ 12 % with a multijunction solar cell.[22]

Despite their numerous good properties, fullerenes have drawbacks like limited absorption, expensive production, difficult functionalization or modification of energy levels and low

photochemical stability.[19][23] For these reasons, the search for alternative, non-fullerene acceptors (NFAs) has increased strongly. NFAs have the potential advantages of cheap production, simple modification, high thermal stability and strong absorption.[24]

In this work, aim is the synthesis of new non-fullerene acceptors and try to improve their permittivity by introduction of polar and flexible side chains. Futhermore, they should be installed in OSCs with determination of their performance and electric properties.

2 Theoretical Background

2.1 Solar Cells

2.1.1 Working Principle

Photovoltaic cells generate electrical current from electromagnetic irradiation. They do so by absorbing photons with appropriate energies, capable of promoting an electron from the HOMO of the absorbing material to its LUMO or higher. This creates localized electron-hole pairs (Frenkel excitons). Due to the usually low permittivity of organic semiconductors (ε_R is around 3-4 [9]), the excitons are quite tightly bound and do not dissociate freely. Their binding energies range around $0.1 - 1.4$ eV [25]. In SCs with a donor-acceptor heterojunction, the exciton dissociates at the interface, generating free charge carriers. The dissociation happens in significant yield, if the energy difference between $\mathrm{LUMO_{Donor}}$ and $\mathrm{LUMO_{Acceptor}}$ is larger than the exciton binding energy E_b. The free electrons then travel through the acceptor to the cathode and the holes through the donor to the anode. The carrier drift is mostly driven by a built-in electric field, however also diffusion plays a role. After absorption at the respective electrodes, they are then available to the external circuit as electric current. The basic process is depicted in Fig.1.[25][26, p.3-7]

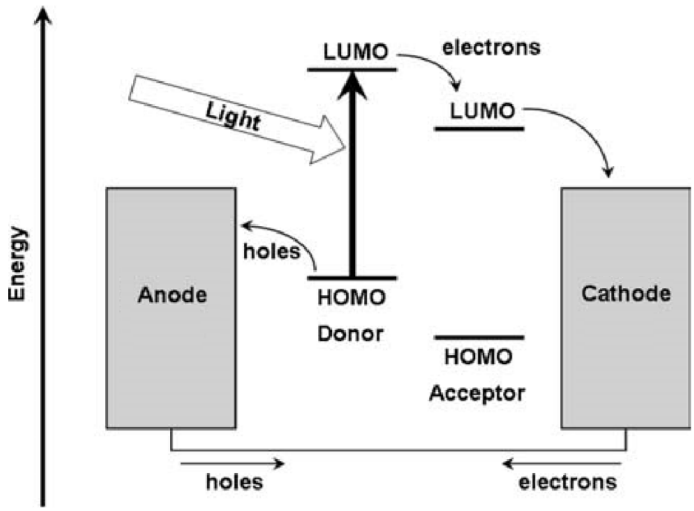

Figure 1: Schematic band structure diagram of an OSC with donor-acceptor heterojunction. Anode and cathode are connected via a short-circuit, therefore their work functions align (this plot is courtesy of Benanti, T. L.; Venkataraman, D. *Photosynthesis Research* **2006**, 87, 73–81, altered for inverted architecture[27]).

2.1.2 J-V Characteristic

The basic J-V curve of a solar cell is shown in Fig.2a. Under illumination, the SC generates current, so the J-V curve shifts to the negative. Different sections can be distinguished [26, p.11]:

1. Negative bias: The applied voltage reinforces the built-in electric field. Exciton dissociation and charge transport are promoted. Drift current dominates.
2. Applied bias approaches zero: Built-in electric field dominates. J_{sc} is produced.
3. Positive bias: Applied voltage opposes built-in field. This is the solar cell's working area. Due to decreased total internal electric field, drift current and overall current decrease.
4. Applied bias equals the built-in bias: V_{oc} is applied. Zero electric field inside the SC. Current becomes zero. Around this point, the diffusion current dominates.
5. Applied bias further increased: Field gradient is reversed. This leads to positive current.

One characteristic point within the fourth quadrant is the maximum power point (MPP, shown as dark grey rectangle in Fig.2a). There, the product of voltage and current density is

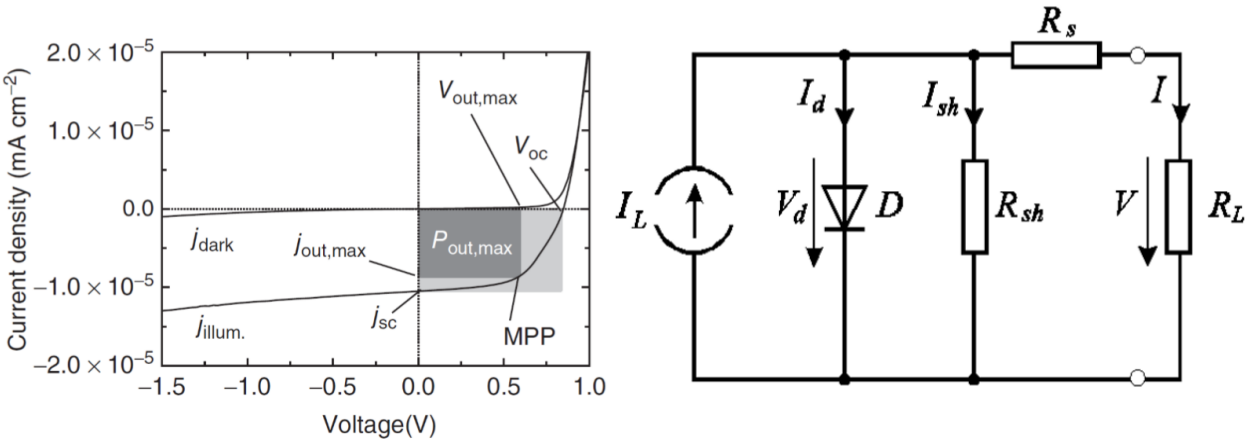

(a) (b)

Figure 2: (a) General J-V caracteristic of a solar cell with and without illumination. Point of maximum power output shown as dark rectangle (this plot is courtesy of Hoffmann, O. T.; Zojer, E. *Organic Semiconductors* (PHT.302UF), Lecture, Graz, University of Technology: Institute of Solid State Physics, **2019**.[28]); (b) Simple equivalent circuit diagram of a solar cell with ideal components: Current source I_L, diode D to add non-linear current-voltage dependence, shunt resistor R_{sh}, series resistor R_s and load resistor R_L (this plot is courtesy of Petritsch, K. *Organic Solar Cell Architectures*, Ph.D. Thesis, Cambridge and Graz, **2000**.[29, p.19]).

highest, so the maximum electric power output is achieved.

To better understand solar cells and possible influences on their performance, they are often translated into electronic *equivalent circuit diagrams* (ECD). ECDs try to mimic the real behaviour of a SC by combining ideal electronic components such as ohmic resistors, current sources and diodes. Dependent on the wanted level of complexity and accuracy, the ECD can be created with more or fewer parts. A simple ECD is depicted in Fig. 2b.[29, p.19-27] It comprises following components [29, p.20]:

- Current source J_L: It creates free charge carriers upon illumination.
- Shunt resistor R_{sh}: It represents exciton recombinations near the dissociation site (or also further away). Its value can be derived from the inverse (I/V) slope around 0 V. Ideally, R_{sh} is as high as possible.
- Series resistor R_s: It represents resistances coming from conductivity and charge carrier mobility in the respective media. High contributors are the interface resistances (e.g. between the active layer and buffer layers). Its value can be derived from the inverse (I/V) slope at $V > V_{oc}$, where the JV curve nears linearity. Ideally, R_s is as low as possible.
- Diode D: It considers the non-linear I-V behaviour.
- Load resistor R_L: Representing the electric load connected to the SC.

Deriving values for these components can be used to determine loss-factors and as way to improve the solar cells.

Quantitatively, OSCs are described by a few characteristic parameters. The most general ones are the open-circuit voltage V_{oc}, the short-circuit current density J_{sc}, the fill factor FF and the power conversion efficiency PCE. The PCE is calculated from the other parameters with

$$PCE = \frac{P_{out}}{P_{in}} = \frac{V_{oc} J_{sc} FF}{P_{solar}} * 100 \tag{2.1}$$

where $P_{in} = P_{solar}$ is the incident solar power density.[26, p.13] For comparability, J-V data are usually measured with a standardized solar spectrum AM1.5 and an intensity of $100\,\mathrm{mW/cm^2}$. The numerator is equal to the electric power density output P_{out} of the SC. If a constant

P_{solar} is assumed, the PCE is therefore dependent on 3 parameters: V_{oc}, J_{sc} and FF.

$\mathbf{V_{OC}}$ is dependent on the difference of orbital energies in bulk heterojunction SCs. The equation is

$$V_{oc} = \frac{E^A_{LUMO} - E^D_{HOMO} - E_b}{q} - C \tag{2.2}$$

where E^A_{LUMO} is the energy of the acceptor's LUMO, E^D_{HOMO} is the energy of the donor's HOMO, E_b is the exciton binding energy, q is the electron charge and C is a constant related to temperature and illumination.[11] Thus, V_{OC} can be increased by careful combination of fitting materials, reduction of exciton binding energies and improving the film morphology.[30]

$\mathbf{J_{SC}}$ is the current density at short-circuit conditions, so when zero external voltage is applied. J_{sc} is dependent on e.g. the molar absorption coefficient, charge carrier mobility, band gap and film-morphology (phase separation etc.).[26, p.12] The current density of electrons j^n and holes j^p, respectively, can generally be divided according to

$$\begin{aligned} j_n &= j^n_{drift} + j^n_{diff} \\ j_p &= j^p_{drift} + j^p_{diff} \end{aligned} \tag{2.3}$$

into drift current j_{drift}, with the electric field in the SC as driving force, and diffusion current j_{diff}, with the charge carrier concentration gradients as driving force.[31, p.43] Depending on the applied voltage, either drift or diffusion can dominate (explained above).

From the ECD (Fig.2b), J_{sc} can be calculated by

$$J_{sc} = J_L - J_{sh} - J_d \tag{2.4}$$

So the achievable J_{sc} can be increased by reducing both leakage currents, J_{sh} through the shunt resistance and J_d through the diode.[29, p.25]

J_{sc} can be further calculated from the external quantum efficiency (EQE) by following equation [26, p.246]

$$J_{sc} = q \int_{\lambda_{min}}^{\lambda_{max}} \Phi(\lambda) EQE(\lambda) d\lambda \tag{2.5}$$

where $\Phi(\lambda)$ is the spectral photon flux (usually AM1.5 or similar, shown in Fig.4a). This

relationship is often used to verify experimentally obtained values for J_{sc} and EQE results.[21]

EQE is the ratio of generated current to incident photons onto the SC. Since it is dependent on the respective wavelength, it is generally given as $EQE(\lambda)$.[29, p.25]

$$EQE(\lambda) = \frac{\text{number of electrons in external circuit at } \lambda}{\text{number of incident photons at } \lambda} \tag{2.6}$$

The EQE can also be formulated as product of all efficiencies along the pathway of the charge carriers, from photon absorption to extraction of the free charge carriers at the electrodes. This pathway can be divided into 5 processes with respective efficiencies [21]:

1. Photon absorption - η_A
2. Exciton diffusion to the heterojunction - η_{diff}
3. Exciton dissociation at the heterojunction - η_{diss}
4. Transport of the free charge carrier to the respective electrode - η_{tr}
5. Collection of the charges at the electrodes - η_{cc}

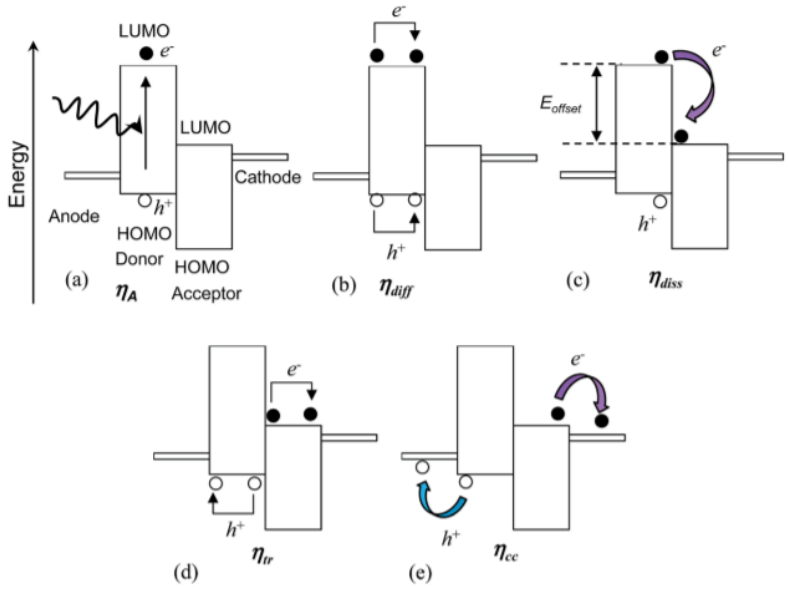

Figure 3: 5 different steps during charge carrier generation with their respective efficiencies: (a) Photon absorption and exciton generation η_A, (b) Diffusion of the bound excitons to the dissociation site (usually the heterojunction) η_{diff}, (c) exciton dissociation η_{diss}, (d) transfer of the free electrons and holes to their respective electrodes η_{tr}, (e) charge collection at the electrodes η_{cc} (Reproduced from Yan, J.; Saunders, B. *R. RSC Adv.* **2014**, 4, 43286–43314 with permission from The Royal Society of Chemistry[21]).

The product of all efficiencies gives the EQE [21]:

$$EQE = \eta_A \, \eta_{diff} \, \eta_{diss} \, \eta_{tr} \, \eta_{cc} \tag{2.7}$$

The respective processes are schematically shown in Fig.3. This relationship also illustrates the difficulty of optimizing EQE over the whole absorbance region, since so many factors play a significant role.[21]

FF The fill factor describes the "squareness" of the J-V curve. It is defined as

$$FF = \frac{V_{mpp} J_{mpp}}{V_{oc} J_{sc}} * 100 \tag{2.8}$$

with voltage and current density at the MPP (V_{mpp}, J_{mpp}). Therefore, FF is the ratio of the real maximum power output to the theoretically achievable maximum power output. Graphically speaking, it defines the shape of the J-V curve. If it is steep in the fourth quadrant, current generation is highly dependent on the internal field and FF is low. Speaking in terms of ECD, the FF is dependent on series resistance R_s and shunt resistance R_{sh} (see ECD above).[26, p.12][32]

Increasing each of these three parameters (V_{oc} , J_{sc} , FF) individually, is generally not feasible since they strongly influence each other. For example, conditions favouring a high EQE (and therefore J_{sc}) may not favour a high V_{oc}. So, a maximum PCE is achieved from an optimal compromise between all influencing parameters.[21]

Often, the Shockley-Queisser limit is used as important design rule for OSCs. In 1960, Shockley and Queisser have calculated the maximum theoretically achievable PCE as a function of the optical band gap. With their assumptions, they calculated an optimum band gap of 1.1 eV to reach the highest PCE of 30 % for a single pn-junction SC.[33] The consideration of a realistic solar spectrum AM1.5 rather than ideal black body radiation changes the original calculations slightly. The result can be seen in Fig.4b.

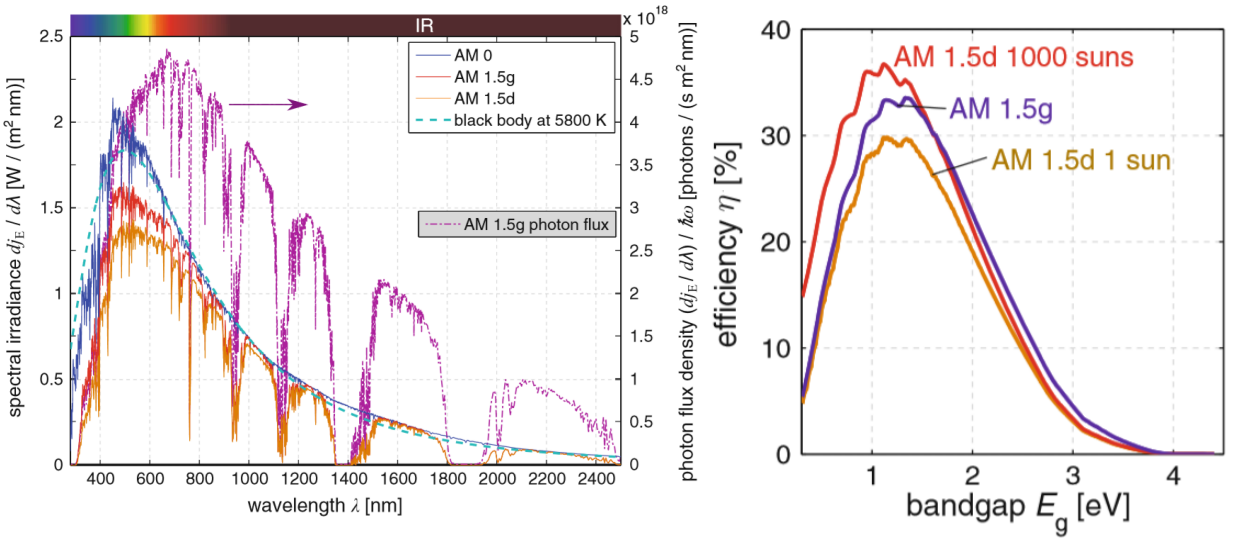

(a) (b)

Figure 4: (a) Solar spectrum (left ordinate) and photon flux density (right ordinate) as a function of wavelength λ. Depicted are different air masses (g...global, d...direct)[31, p. 17]; (b) Maximum achievable PCE as function of the optical band gap, calculated for a single pn-junction with AM1.5 (direct and global).[31, p.54] (reprinted from Tress, W., *Organic Solar Cells*; Springer Series in Materials Science, Vol. 208; Springer International Publishing: Cham, **2014**, [31]).

2.1.3 Architectures

The high effort in research in OSCs has produced many different building types, materials and material combinations. Some possible ways to categorize them are:

- Homojunction vs. heterojunction
- Single junction cells vs. tandem cells
- Normal vs. inverted architecture
- Bilayer vs. bulk heterojunction

In a **homojunction**, a pn-junction is formed by connecting a p-doped area to a n-doped area of the same material (e.g. in silicon solar cells). In a **heterojunction**, on the other hand, the pn-junction is realized by creating an interface of 2 different materials with usually different properties (e.g. different Fermi-energy, ionization energy and electron affinity). These devices are intrinsically selective in the transport direction of electrons and holes.[31, p.51]

Multijunction cells comprise, in contrast to the **singlejunction** solar cells, more than one pn-junction. They are usually assembled in series. An advantage of tandem cells is the

possible overcoming of the Shockley-Queisser limit for single pn-junctions. However, the complexity and thus the production costs of the system increase compared to the single junction cells.[34][33][35]

Normal and **inverted** device architecture differ in their direction of polarity (see Fig. 5a). In normal architecture OSCs, electrons flow from the active layer via an ETL to the back electrode (cathode, usually a reactive metal with low work function, e.g. Al) and holes flow via the HTL to the transparent anode (ITO). In an inverted architecture, the flow is reversed. Now, the ITO functions as electron collecting cathode and the back electrode collects the holes (anode, usually a noble metal with high work function, e.g. Ag, Au or Cu). A benefit of the inverted type is a better long-time stability due to the use of noble metals. Furthermore, inverted structures are more compatible with roll-to-roll processing. An example for the energy level alignment in an inverted SC is depicted in Fig. 5b.[21][36][37]

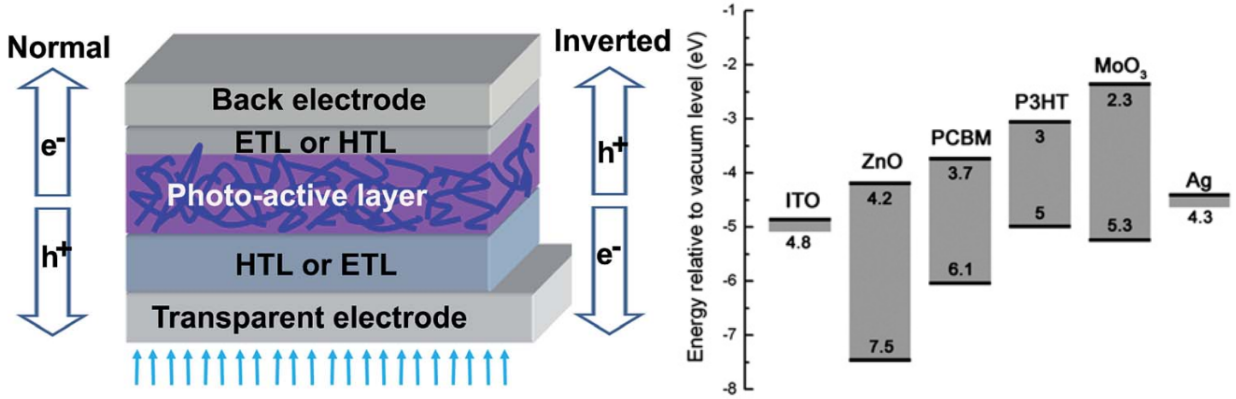

(a) (b)

Figure 5: (a) Normal vs. inverted architecture in OPVs, containing eletron transport layers (ETL) and hole transport layers (HTL) (Reproduced from Zhan, C.; Zhang, X.; Yao, J. *RSC Advances* **2015**, 5, 93002–93026 with permission from The Royal Society of Chemistry, [36]); (b) Energy levels of an inverted architecture SC with ITO (cathode), ZnO (ETL), P3HT (donor), PCBM (acceptor), MoOx (HTL) and Ag (anode) (Reproduced from Wang *et al. J. Mater. Chem.* **2010**, 20, 862–866 with permission from The Royal Society of Chemistry[38]).

Bilayer heterojunction devices consist of separate donor and acceptor phases, deposited on top of each other as layers. This leads to a small interface but the shortest possible pathways for the charge carriers to the respective electrodes. In **bulk** heterojunctions (BHJ), donor and acceptor material form a fine network, which is formed during deposition or drying. That way, the materials share a much greater interface (see Fig. 6). Advantages of the BHJ are shorter

path lengths for excitons to reach the dissociation site (donor acceptor distance in range of 10-20 nm, which is about the same magnitude as usual exciton diffusion lengths [39][11])and a much larger donor-acceptor interface. This leads to a lower exciton recombination rate. The main disadvantage is the generation of many dead-ends in which the donor or acceptor are not connected to the respective electrodes (or transport layers). That way, charge carriers can get trapped and will eventually recombine.[40][21]

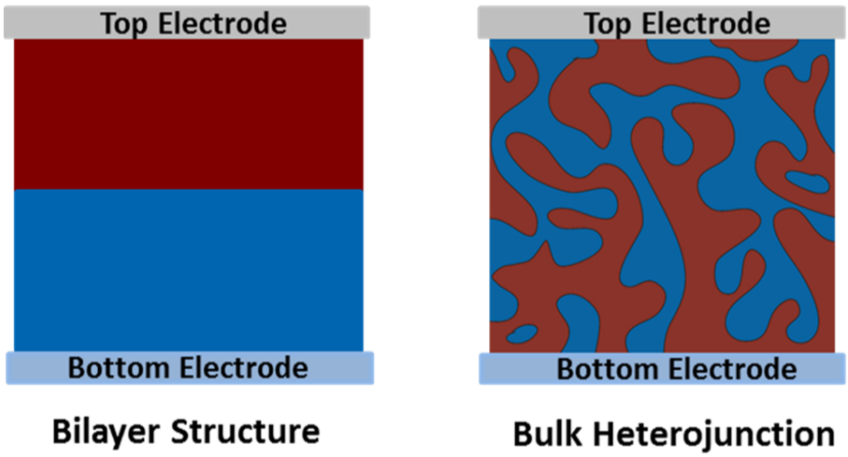

Figure 6: Schematic cross-section of a bilayer (left) and bulk (right) heterojunction (reproduced from Wang, H.-J.; Chen, C.-P.; Jeng, R.-J. *Materials* **2014**, 7, 2411–2439 with permission from MDPI Open Acces Journals[41]).

2.1.4 Materials

Polymer donors Donor materials in OPVs are often polymers with a conjugated backbone with semiconducting properties.[21] Early polymers were polyacetylenes with PCE values of 0.3 % in OSCs.[4, p.12] More efficient polymers were poly-thiophenes or MEH-PVV.[4, p.12][42] The repeating units soon became more complex. One approach to lower the bandgap and thus increase J_{sc} is to alternate electron rich and electron defficient groups within the repeating unit. This favours intramolecular charge transfer and thus, delocalization.[42] Also, it enables the separate tuning of E^D_{HOMO} and E^D_{LUMO}, respectively. [43] Some popular donors are PBDB-T[44], PTB7 or PTB7-Th[36] (see Fig.7).

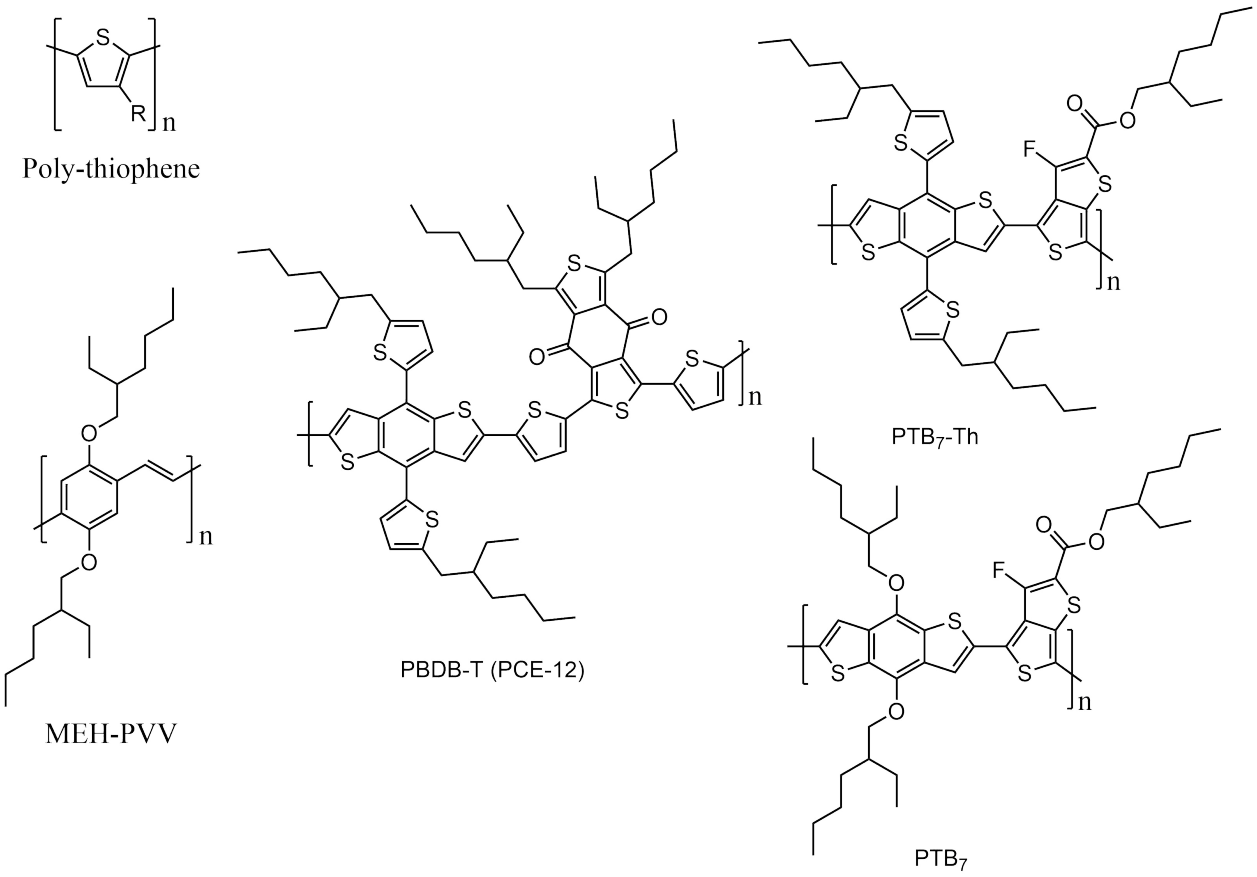

Figure 7: Popular donor polymers in OPVs.

Acceptors In OPV there are 2 major classes for acceptor materials: fullerene acceptors and non-fullerene (or post-fullerene) acceptors (NFAs).

Fullerenes are interesting materials due to their high and isotropic electron mobilities, strong electron accepting capabilities and good miscibilities with many polymeric donors.[36] On the other hand, drawbacks are the difficult tunability of their optoelectronic properties[45], challenging and expensive synthesis[46] and often narrow absorption bands.[36] Also they often exhibit low photochemical stabilities.[23] For these reasons, research for NFAs increased strongly, since they have the advantages of high absorption, high thermal stability, possible low cost production and easy tunability.[24] Some fullerene and non-fullerene acceptors are depicted in Fig.8 and Fig.9.

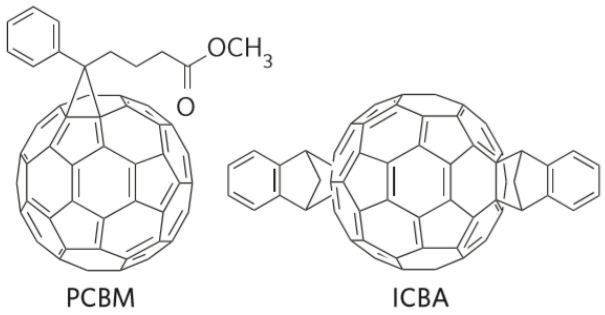

Figure 8: Popular fullerene acceptors (reprinted from Li, G.; Zhu, R.; Yang, Y. *Nature Photon* **2012**, 6, 153–161,[42]).

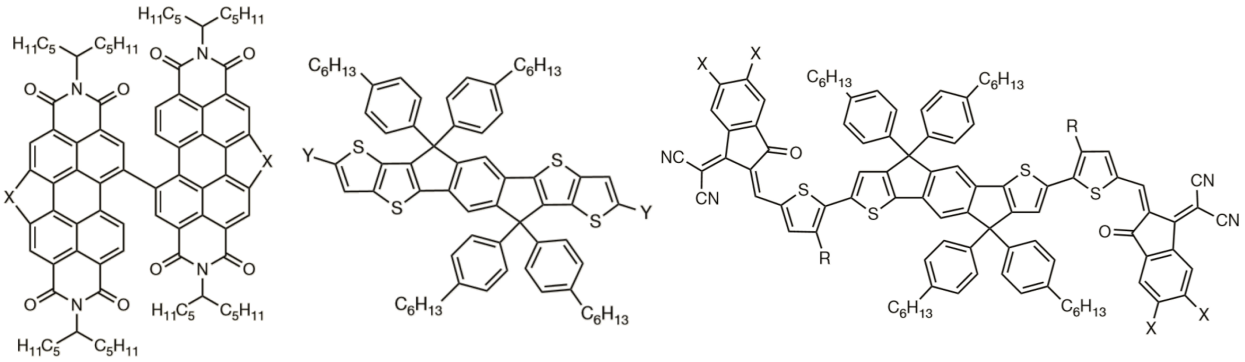

Figure 9: Non-fullerene acceptors: linked rylene dye (left), fused-ring acceptor (middle) and ITIC (right) (reprinted from Yan, C. *et al. Nature Reviews Materials* **2018**, 3,[47]).

2.2 Density Functional Theory

2.2.1 Background

The energy of a molecule's ground state E_0 can be theoretically calculated by solving its Schrödinger equation. The time-independent, non-relativistic Born-Oppenheimer approximation is

$$\hat{\mathcal{H}}\Psi(r_1, r_2, ..., r_{n-1}, r_n) = E\Psi(r_1, r_2, ..., r_{n-1}, r_n) \tag{2.9}$$

where $\hat{\mathcal{H}}$ is the time-independent, electronic Hamilton operator, Ψ is the electronic wavefunction of the molecule with the respective positions of the electrons r_n and E is the electronic energy and eigenvalue of transformation $\hat{\mathcal{H}}$ on function Ψ. Addition of the separated nucleus

energy gives the total energy of the molecule. The Hamilton operator looks like

$$\hat{\mathcal{H}} = -\frac{1}{2}\sum_{i}^{N}\nabla_i^2 + \hat{V}_{ext} + \sum_{i<j}^{N}\frac{1}{|r_i - r_j|} \tag{2.10}$$

where ∇_i^2 is the Laplace operator

$$\nabla_i^2 = \frac{\partial^2}{\partial x_i^2} + \frac{\partial^2}{\partial y_i^2} + \frac{\partial^2}{\partial z_i^2} \tag{2.11}$$

Eq.(2.10) comprises three terms, the kinetic energy of the electrons (first term), the external potential V_{ext}, which is determined by the position and charge of the nuclei (second term), and the electron-electron interaction (third term). N denotes the total number of electrons in the system. Within $\hat{\mathcal{H}}$, only N and V_{ext} contain information about the actual molecule.

In reality, almost any molecule is too complex that an exact solution for the Schrödinger equation would be possible. For that reason, detours were developed over which e.g. the ground state energy E_0 can be approximated. They all rely on extensive computational iterations. On an elementary level, they all base on the *variation principle*.

The **variation principle** states, that by variation of a trial-wave function Ψ_{trial} and applying $\hat{\mathcal{H}}$ on it, an upper limit for the true ground state energy can be found, i.e.,

$$\langle\Psi_{trial}|\hat{\mathcal{H}}|\Psi_{trial}\rangle = E_{trial} \geq E = \langle\Psi|\hat{\mathcal{H}}|\Psi\rangle \tag{2.12}$$

and E_{trial} is only equal to E, if Ψ_{trial} equals Ψ. Transformation leads to

$$E_0 = \min_{\Psi\to N} E[\Psi] = \min_{\Psi\to N}\langle\Psi|\hat{T} + \hat{V}_{Ne} + \hat{V}_{ee}|\Psi\rangle \tag{2.13}$$

where $\hat{T}$, $\hat{V}_{Ne}$ and $\hat{V}_{ee}$ are the operators for the kinetic energy, potential energy in the electric field of the nuclei and electron-electron interaction energy, respectively. Since trying all physically meaningful N-electron wave functions is impossible, the iterations are generally limited to certain subsets of wave functions. This leads, of course, only to approximate wave functions and energies. One often used subset is the Hartree-Fock-approximation, where Ψ is approximated by the antisymmetric *Slater determinant* Φ_{SD}.

As mentioned before, N and V_{ext} contain all information to determine $\hat{\mathcal{H}}$, which itself then can determine E_0 and Ψ. Thus, E_0 can be expressed as a functional of solely N and V_{ext}.

$$E_0 = E[N, V_{ext}] \tag{2.14}$$

This fundamental correlation is exploited for DFT calculation.[48, p.3-10]

2.2.2 Calculation

For conducting the DFT calculation, start approximations have to be made. Two of them are to pick a *functional* and a *basis set*. The calculation will the be conducted according to their approximations and equations.

One popular *functional* in chemistry is the BLYP functional. It is a so-called generalized-gradient approximation (GGA), that, as extension from the simpler local density approximation (LDA), not only considers the electron density $n(r)$ at point r, but also tries to model the temporary inhomogeneity of the electron density by including a gradient $\nabla n(r)$. This gives a new function $f(n(r), \nabla n(r))$. BLYP combines the exchange functional of Becke (1988) with the correlation functional of Lee, Yang and Parr (1988). It generally gives good results for chemical bonds such as covalent, metallic, ionic and hydrogen bridges.[49] However, for van der Waals interactions the popular GGAs fail.[50]

The *basis set* comprises a set of functions which represent the wave function in the DFT calculation. Since the size of the basis set influences the computation time with about the fourth order in a Hartee-Fock calculation, it is generally desired to reduce it as much as possible.[51, p.142]. In the 6-31G basis set, each inner orbital is represented by one basis function comprising 6 primitive Gaussians. Additionally, valence orbitals consist of 2 basis function, each comprising 3 and 1 Gaussians, respectively (so-called split-basis valence set).[52][51, p.144] The 6-31G* set has additional polarization functions with d-symmetry and the 6-31+G* set uses diffuse s- and p-type orbitals.[51, p.144]

3 State of the Art

Efficiencies of OSCs have increased fast over the last two decades. As overview, Fig.10 shows the trend of the best research efficiencies of organic solar cells. Currently, the leading OSC achieved a PCE of 17.4 %.

Due to various drawbacks of fullerenes as electron acceptors in OPV application (see Introduction), the search for alternative acceptors is currently a prominent research topic.[53] One molecule, which has received much attention in this regard, is perylene and its derivatives.

Perylene diimide (**PDI**), for example, is a highly studied dye because of its easy tunability and high thermal stability. Examples are shown in Fig.11.[54] They are usually modified by substitution on the aromatic system, varying N-substituents or linking or fusing multiple PDI units together.[47] Examples are reported e.g. by Hartnett *et al.*, who reported PCE values of 0.65, 1.20 and 3.67 % for PDI acceptors substituted with hexyl, phenethyl and phenyl units at the aromatic system (**PDI-1**,[55]). Zang *et al.* have reported PDI units linked via the bay position, reaching efficiencies of 5.90 % (**PDI-2**,[56]). Even higher performance was achieved by Liang *et al.*, who synthesized PDI trimers linked via the nitrogen atoms, which achieved 7.25 % PCE in bulk heterojunction SCs (**PDI-3**,[57]).

Since PDIs also have drawback, e.g. usually low lying LUMOs (around −4.0 eV) and strong aggregation and therefore bad miscibility with popular donors, perylene monoimides (PMI) have further emerged as interesting acceptor molecules.[58] PMI and its derivatives are now used in various applications, e.g. as dyes, in organic light-emitting diodes (OLED) or as

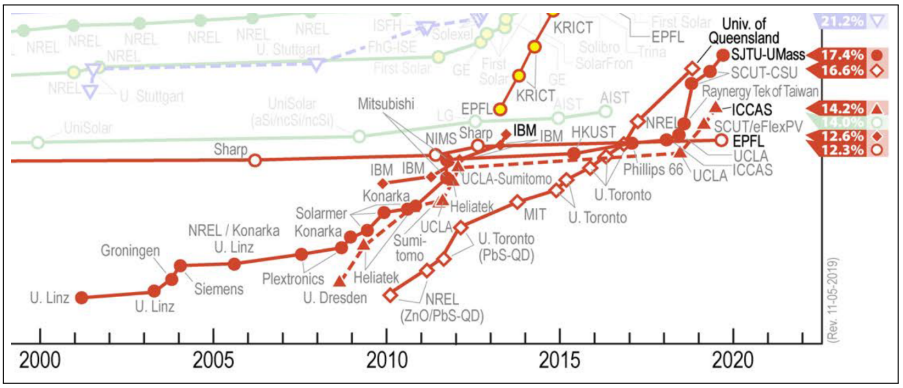

Figure 10: NREL best research-cell-efficiency chart (close-up), organic solar cells shown as full orange circles; this plot is courtesy of the National Renewable Energy Laboratory, Golden, CO.[8]

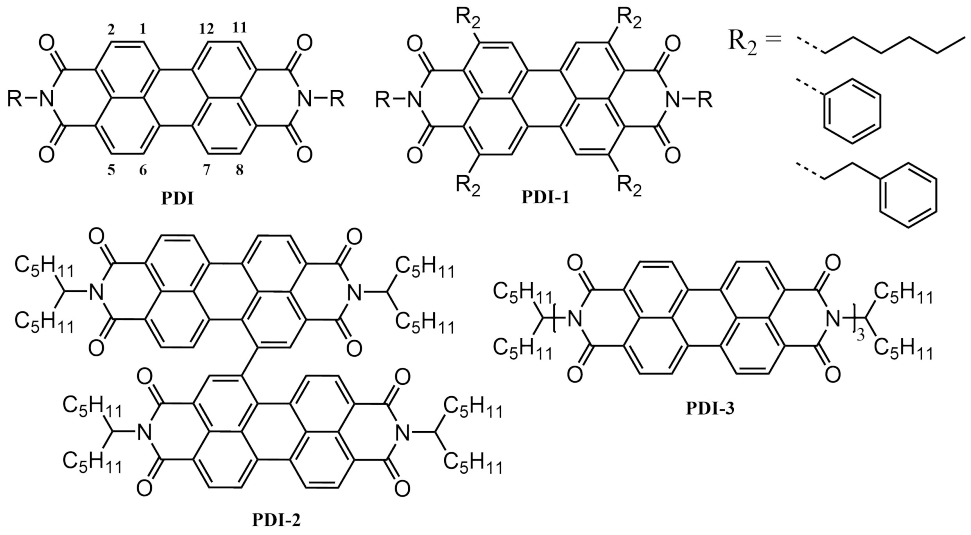

Figure 11: Examples for PDI molecules.

fluorescent probes (examples are shown in Fig.12).[59] Already in 2005, Cremer *et al.* have investigated molecules comprising a PMI unit linked to an oligothiophene chain for use in electronic devices, showing higher LUMO energies (around -3.4 eV) (**PMI-oTh**,[60]). PMIs are often used in acceptor-donor-acceptor (A-D-A, A=PMI) molecules with an electron-rich linker. This molecule-type is interesting because it allows separate fine-tuning of the HOMO and LUMO, by individually altering the donor and acceptor unit.[61] In 2017, Hu *et al.* have tested A-D-A molecules with different linker molecules and PMI as acceptor, e.g. phenylene and single and condensed thiophenes. With PCE-10 as donor, they reached performances of $0.1 - 0.2$ % and a maximum of 1.3 % for the $5,5$-bithiophene linked molecule (**D1, D4, D5, D6, D7**,[59]). Zhang *et al.* have reported a PMI-fluorene-PMI acceptor, achieving 2.30 % efficiency with P3HT as donor (**D2**,[58]). Qin *et al.* used directly linked and acetylene-linked PMI molecules as second acceptor in ternary SCs, achieving a PCE of 9.77 %, increased from 8.35 % for the binary reference SC without PMI acceptor (**D3**,[35]).

Some effort has also been put into increasing the permittivity ε of the organic semiconductors. One general design principle for increasing ε is the introduction of polar/polarizable substituents or side chains.[11] This is based on the relationship between the polarizability of a compound and its permittivity, mathematically expressed with the Clausius-Mossotti equation

$$\frac{\varepsilon_r - 1}{\varepsilon_r + 2} = \frac{N}{3\varepsilon_0}\alpha = \frac{\rho N_A}{3M}\alpha \tag{3.1}$$

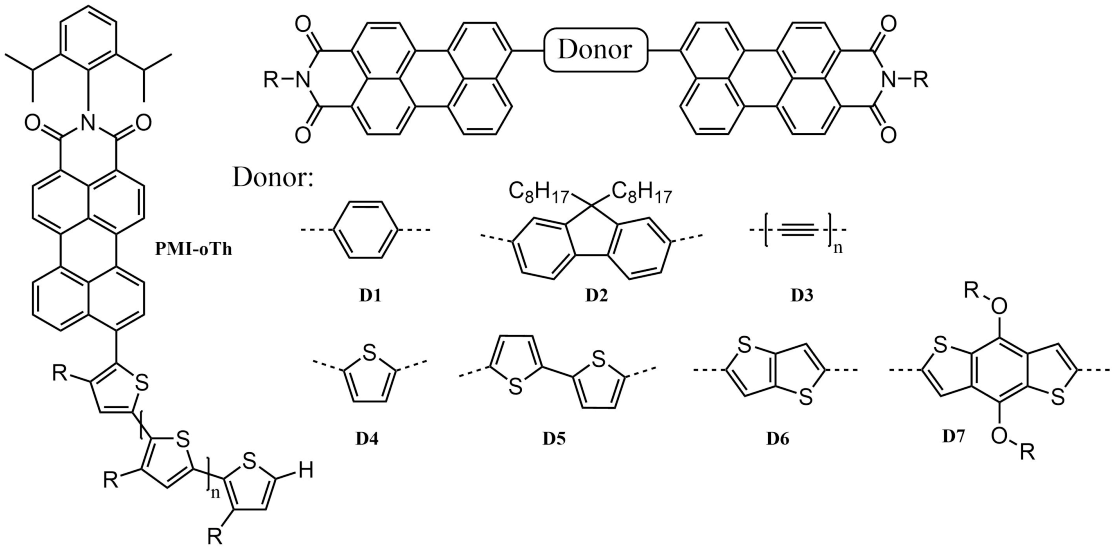

Figure 12: Examples acceptor molecules with PMI units.

where ε_r is the relative permittivity, ε_0 the permittivity of vacuum, N the number density of atoms/molecules, N_A the Avogadro constant, ρ the mass density, M the molar mass and α is the polarizability of the respective compound (defined by $\alpha = p/E$, where E is the applied electric field and p the induced electric dipole moment).[62]

In 2006, Breselge *et al.* first introduced oligo(ethylene glycole) (OEG) side chains to a donor polymer, poly(*p*-phenylene vinylene) (PPV). This yielded an increase of ε_r to a maximum of 5.5 for diPEO(PPV) (**P1**, Fig.13), compared to 3.3 for the starting material OC_1C_{10}-PPV. Furthermore, the conductivity σ increased ($\sim 10^{-4}$ S/m) while the electron mobility μ remained unchanged (range $10^{-4}\,\mathrm{cm}^2/\mathrm{Vs}$). However, the OEG-PPV polymer showed strong phase separation in the used blend with PCBM as acceptor, leading to lower PCE and J_{sc} . They underlined the importance of matching the polarities of donor and acceptor.[63] Torabi *et al.* explained, that the strong influence of the ethyleneglycole chains is due to their high flexibility. Their rapid rotation lies in the GHz and MHz range, constantly reorienting its dipole moment. This significantly enhances the permittivity in the GHz range, where it is relevant for recombination processes.[64]

The same approach was used by Liu *et al.*, who introduced oligoethylene oxide side chains to the popular acceptor molecule ITIC. This increased ε_r from 4.5 (ITIC) to 7.5 (10^3 Hz) - 9.5 (10^6 Hz) (ITIC-OE, **P2**) with device efficiencies of 8.5 % when used in bulk heterojunction with donor PBDB-T. This was slightly lower than the reference cells with original ITIC

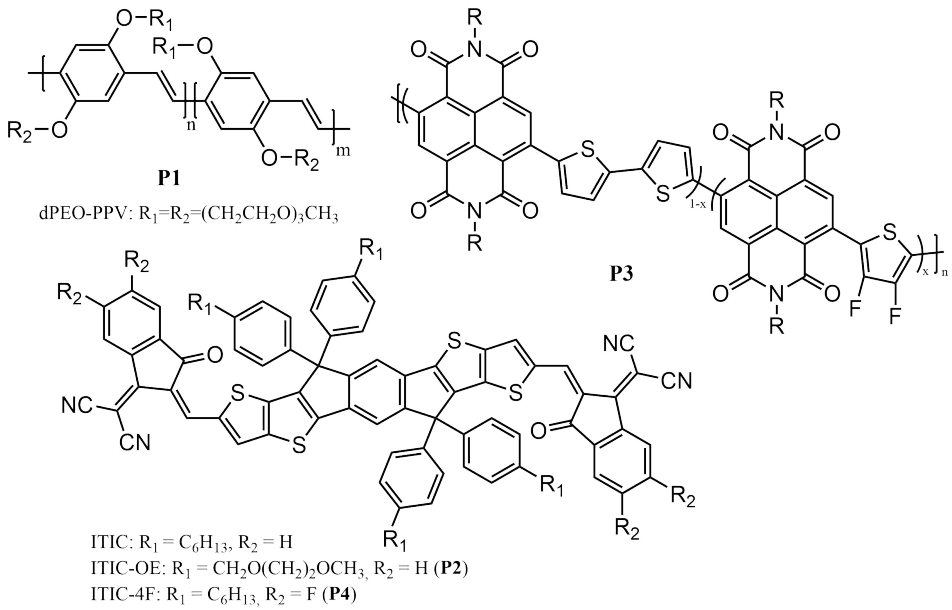

Figure 13: Examples for molecules with increased permittivity.

(10.4 %), resulting from worse crystallinity and too good miscibility with the donor, which hindered the formation of important microphase separation.[65]

In 2019, Zhang *et al.* reported another approach towards increasing the permittivity. They incorporated fluorinated thiophenes onto a naphthalene diimide-bithiophene backbone by co-polymerization (**P3**, Fig.13). When increasing the molar ratio of fluorinated thiophene from 5 to 10 to 15 %, they measured a steady increase of ε_r over the whole frequency interval (10^3-10^5 Hz) from 3.31 to 3.38 to 3.53 of the PBDB-T:acceptor blend, respectively (average over the whole frequency). The best performance was achieved with the 5 % acceptor, achieving a PCE of 8.0 % and a record J_{sc} of 15.08 mA/cm^2, one of the highest values for all-polymer SCs using fluorinated acceptor polymers.[66] The same was done with ITIC by the same group. They showed that a blend of fourfold fluorinated acceptor ITIC-4F (**P4**, Fig.13) with twofold fluorinated donor PBDB-T-2F showed a low recombination coefficient of $2.404 \times 10^{-13}\,\mathrm{cm^{-3}s^{-1}}$ and a small reduction factor of 3.71×10^{-2}. Both values indicate a reduced bimolecular recombination rate and a high charge dissociation rate.[67]

4 Objective

The underlying motivation for this work was the potentially wide-ranging influence of the permittivity ε on many processes within the photovoltaic cell. An increase of ε could, for example, lead to reduction of charge carrier recombinations and increase of mobilities, which would improve both, J_{sc} and achievable V_{oc} of the solar cell, potentially enhancing the PCE.

The objective is the development of synthetic routes for new acceptor-donor-acceptor (A-D-A) compounds for use in OSCs. Perylene-linker-perylene molecules are used as basis scaffold, with fluorene and carbazole as linker and perylene monoimide (PMI) as side groups. Polar side chains should be introduced to the linker molecules. It has already been demonstrated that by doing so, the permittivity of molecules can be improved.[68][65][64] However, to our knowledge, this has never been done to PMI based A-D-A molecules. The polar groups of the side chains should be introduced without conjugation/connection to the chromophoric system to allow improving the electric properties without changing its optical properties. Similar PMI-linker-PMI molecules with alkyl side chains have already been investigated within the working group. This allows for a direct comparison of the new acceptors with already present ones in terms of properties and solar cells performance.

From this, following goals were identified: **i)** establishing synthetic procedures for new linker molecules with polar side chains, **ii)** preparation of A-D-A (A=PMI, D=linker) compounds, **iii)** optical, computational and thermal characterization, **iv)** DFT analysis of geometric and optical properties, **v)** testing the new compounds in bulk heterojunction solar cells.

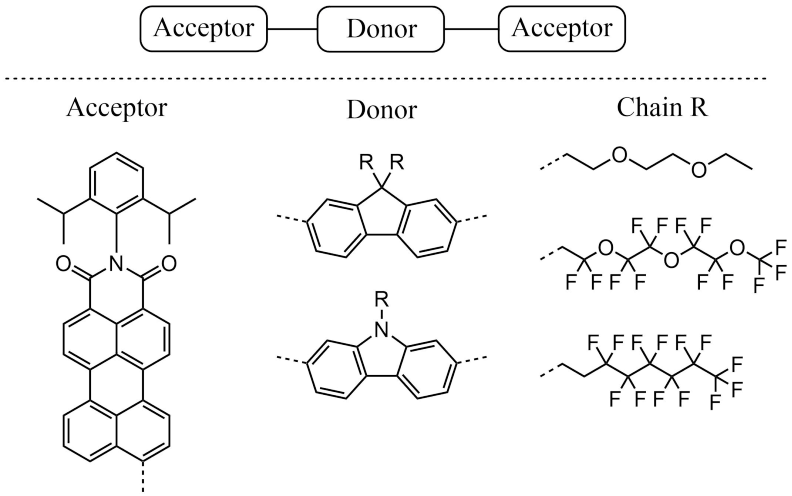

Figure 14: General scheme of target molecules.

5 Results and Discussion

5.1 Synthesis

5.1.1 Approach

All products were prepared by the same procedure. First step was the activation of the wanted side chain by improving its leaving group for later reaction. This was followed by alkylation of the linker molecules, 2,7-dibromofluorene and 2,7-dibromocarbazole, respectively. Finally, the linker molecule was applied in a Suzuki-coupling reaction with PMI. For this, the perylene molecule was equipped with a boronic ester group, which was done by bromination at the aromatic system and a subsequent Pd-catalyzed metal-halogen exchange with a boronic pinacol ester unit.

5.1.2 Side Chains

4 different chains were examined: 2-(2-(ethoxy)ethoxy)ethan-1-ol (**DEG-OH**), 2,2-difluoro-2-(1,1,2,2-tetrafluoro-2-(1,1,2,2-tetrafluoro-2-(trifluoromethoxy)ethoxy)ethoxy)ethan-1-ol (**TEG_F-OH**), 1,1,1,2,2,3,3,4,4,5,5,6,6-tridecafluoro-8-iodooctane (**Oct_F(4H)-I**) and 2,2,3,3,4,4,5,5,6,6,7,7,8,8,8-pentadecafluorooctan-1-ol (**Oct_F(2H)-OH**). On all chains except from Oct_F(4H)-I, the hydroxyl group was converted into a better leaving group. Used leaving groups were bromide Br^-, methanesulfonate OMs^- and trifluoromethanesulfonate OTf^-. Reaction schemes are shown in Fig.15, 16 and 17.

Bromination was tried with 2 approaches. First approach was the Appel reaction with CBr4 and PPh3 as reagents. However, purification turned out to be complicated, since traces of phenyl species, probably oxidized Ph3PO, remained in the organic phase after workup. Therefore, PPh3 and CBr4 were replaced with PBr3 as reagent. This simplified the purification since the only by-products were phosphorous acid H3PO3 and HBr from contact with water (vapour formation)[69, p.151], which were easily removed during aqueous workup. Also, HBr formation could be mostly supressed by working in dry conditions in nitrogen atmosphere. Bromination worked nicely for DEG-OH. After simple purification (aqueous

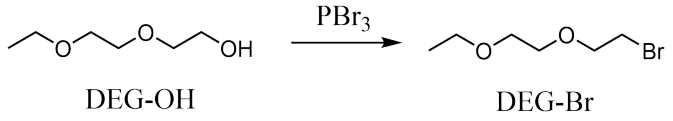

Figure 15: Synthesis scheme DEG-Br: PBr3, CH_2Cl_2, 0 °C, RT, 24 h (80 %).

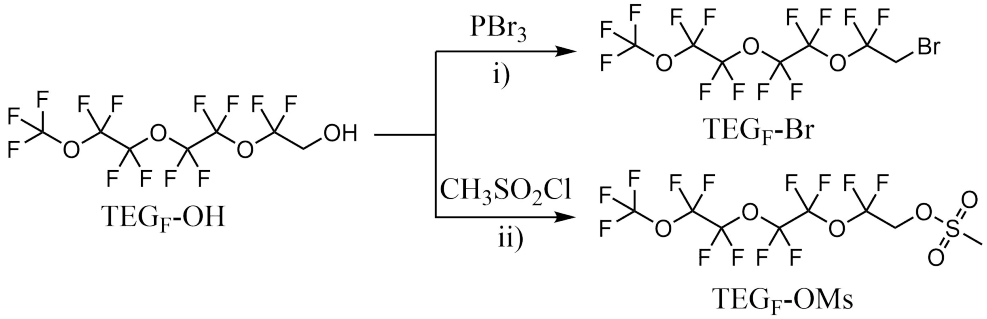

Figure 16: Synthesis scheme end group exchange TEG_F chain: i) PBr3, CH_2Cl_2, 0 °C, RT, 24 h (0 %); ii) CH_3SO_2Cl, Et3N, THF anh., 0 °C, RT, over night (75 %).

workup and distillation at atmospheric pressure), the product was obtained in 80 % yield as colorless liquid.

When the same reaction conditions were applied to TEG_F-OH, only low yields of expected product were achieved despite full conversion of the starting material. Instead, multiple by-products were formed, which made purification difficult. Thus, conversion of the alcohol to a mesylate was tried as activation instead.

Mesylation was done in dry, inert conditions with methanesulfonyl chloride MsCl and a non-nucleophilic base (Et3N) at 0 °C. This gave the mesylated product TEG_F-OMs in good yield (80 %) after aqueous workup. No further purification was necessary.

Triflation was done with triflic anhydride and pyridine as mild base. This lead to quantitative conversion of $Oct_F(2H)$-OH to Oct-(2H)-OTf. No further purification was necessary after

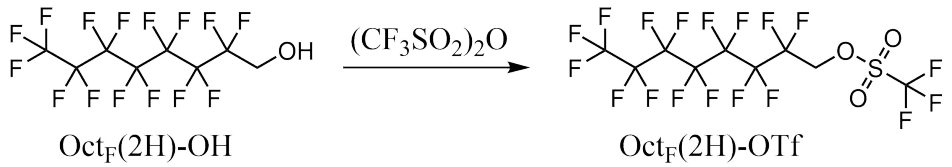

Figure 17: Synthesis scheme $Oct_F(2H)$-OTf: $(CF_3SO_2)_2O$, pyridine, CH_2Cl_2 anh., 0 °C, RT, over night (75 %).

aqueous workup. Particular care had to be taken with the choice of the solvent. Dry solvents and conditions were necessary so not to produce triflic acid. However, slight hydrolysis could not be prevented, most likely due to residual water in the dry solvents. This, in case of dry THF as solvent, lead to initiation of cationic ring-opening polymerization of the solvent to poly-tetrahydrofuran, which is catalyzed by strong acids.[70] Best solvent suitable for the triflation was dry CH_2Cl_2.

5.1.3 Linkers

Investigated linker molecules were 2,7-dibromofluorene and 2,7-dibromocarbazole. All reactions are depicted in Fig.18, 19 and 21. The following section is grouped by the different side chains, because it best reflects the chronologic evolution and reasoning during the laboratory period.

DEG-chain Synthesis of the linkers with DEG chains was straightforward and done according to literature.[71][72] Alkylation of the fluorene was done in a bi-phase system of toluene and aqueous sodium hydroxide (50 % w:w) with a phase transfer catalyst (tetrabutyl ammonium bromide, TBAB). This should prevent the hydroxide from acting as nucleophile. The reaction gave a yield of 63 %. The alkylation of carbazole was done with crushed KOH in DMSO, which also lead to the desired product in satisfying yields (70 %). Purification was easily done by flash chromatography because of the much lower R_f values of the products in CH_2Cl_2.

Oct_F(4H)-chain Alkylation with the Oct_F(4H) side chain was first attempted with the same method as for the DEG-chains, but without success. In the first attempts of alkylating **fluorene**, mainly a side-product formed. Its by flash chromatography yielded a solid with intense yellow color. Literature research revealed, that position 9 (the alkylation site) of fluorene can be readily oxidized by molecular oxygen due to its benzylic position and expansion of aromatic system in case of oxidation (shown for example in [73]). NMR analysis confirmed it to be the oxidized 2,7-dibromofluoren-9-one (NMR spectrum compared to[74]). The reaction was then conducted in nitrogen atmosphere, but still mainly the ketone formed. Literature research revealed that liquid fluorocarbons have exceptionally high gas-dissolving

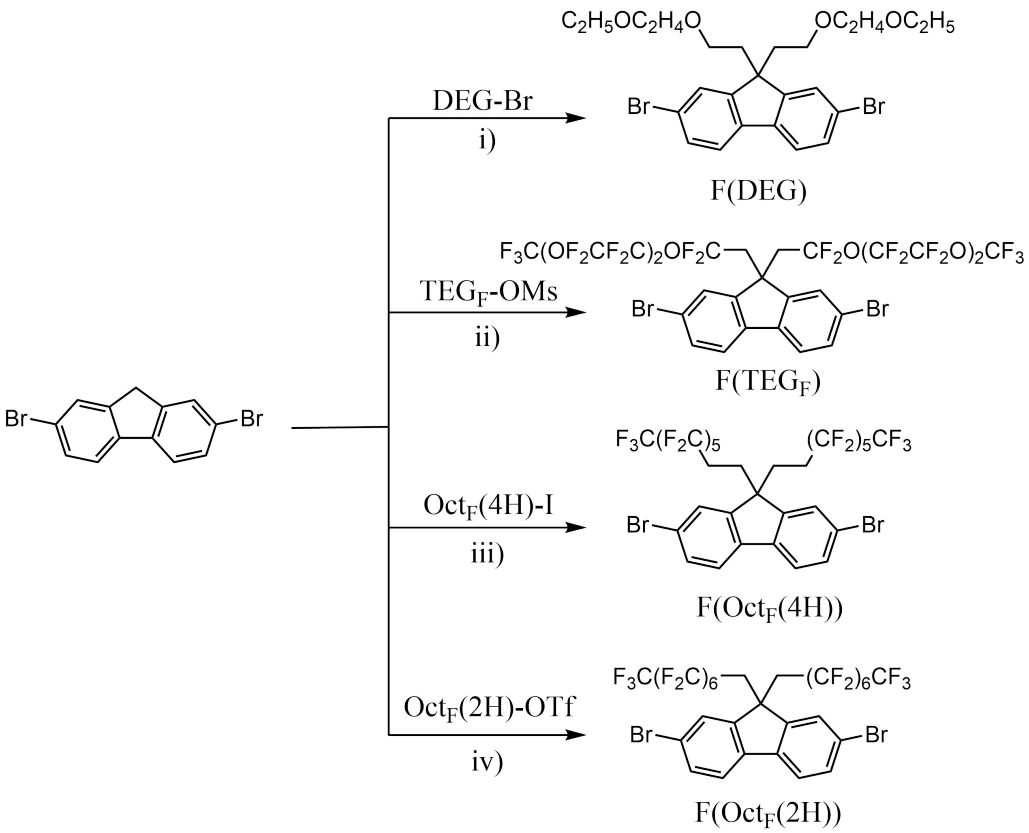

Figure 18: Synthesis scheme alkylation fluorene with various side chains: i) DEG-Br, NaOH aq. (50 % w:w), TBAB cat., toluene, 80 °C, 23 h (63 %); ii) like i) with TEG_F-OMs (0 %) or TEG_F-OMs, KO^tBu, DMF anh., RT, 80 °C, over night (0 %); iii) Et3N, toluene, reflux (0 %) or NaH (2×0.5 eq.), Oct_F(4H)-I (2×0.5 eq.), DMF anh., 0 °C, RT (0 %); iv) like i), Oct_F(2H)-OTf (0 %).

capacities.[75] So, the fluorene was thought to be oxidized by molecular oxygen dissolved in the fluorinated side chain Oct_F(4H)-I. As consequence, all liquid fluorinated chains (TEG_F-OH, Oct_F(4H)-I and Oct_F(2H)-OTf) were degassed with the freeze-pump-thaw method (4-6 cycles, respectively) and stored in Schlenk flasks over 4 Å molsieves in nitrogen atmosphere. After this measure, no more (or only a small fraction of) ketone formed.

Despite inert conditions and degassed reagent, no desired product formed. By using the same conditions as for the DEG chain alkylation (biphase system, toluene, aq. NaOH, TBAB), many by-products formed. Lee *et al.* already reported the same problem when trying to alkylate 2,7-dibromofluorene with a perfluoroalkyl chain with ethylene spacer. They reported a preferred elimination (dehydrohalogenation) of the alkyl iodide to the corresponding vinyl compound, leading to a dark residue.[76] The reported observations match with those made in this work. Other reaction conditions were tried, e.g. using KO^tBu as base in anhydrous

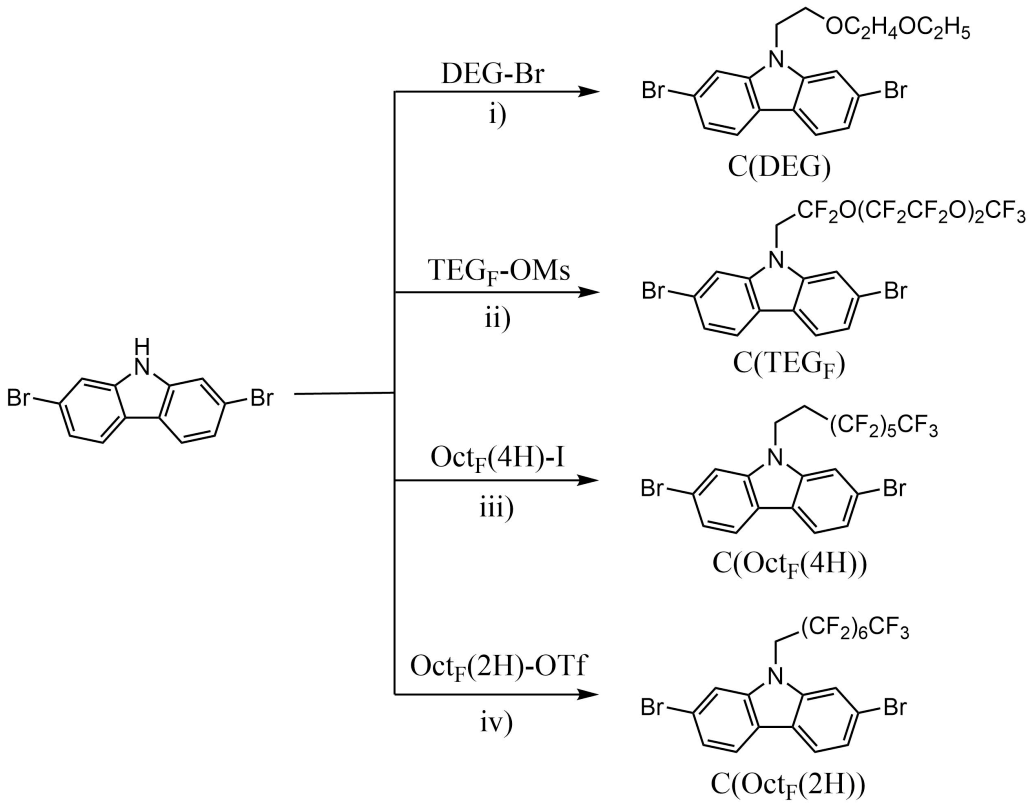

Figure 19: Synthesis scheme alkylation carbazole with various side chains: i) DEG-Br, KOH crushed, DMSO, RT, 19 h (68 %); ii) like i) with TEG_F-OMs (0 %) or TEG_F-OMs, KO^{t}Bu, DMF anh., RT, over night (0 %); iii) Oct_F(4H)-I, Et_3N or ^{i}PrEt$_2$N, toluene, 110 °C or RT, 16 h (both 0 %) or Oct_F(4H)-I, NaH, THF anh., 0 °C, RT, 18 h (0 %); iv) Oct_F(2H)-OTf, NaH or KO^{t}Bu, DMF anh., 0 °C, RT, 60 − 110 °C, 50 h (4 %) or Oct_F(2H)-OTf, KOH, DMSO, RT, 15 h (0 %).

dioxane or sequential alkylation with NaH as base, but without change of the outcome.

Attempts with **carbazole** led to similar results. Reaction control with TLC usually revealed complete consumption of the chain, despite being used in excess (2-6 eq). Simultaneously, the linker was not consumed. It was again believed that elimination of the chain is preferred over substitution. 2 approaches were tried. First was the use of a mild, non-nucleophilic base (Et_3N, Et^{i}Pr$_2$N, K_2CO_3) or medium strong base (KOH, DBU) and simultaneous reaction. Second approach was a beforehand deprotonation of carbazole with a strong base (NaH, KO^{t}Bu) in dry conditions and subsequent reaction with the chain. However, in both approaches it is believed that either the present base or the deprotonated carbazole itself facilidated dehydrohalogenation of the chain, since all conditions lead to the same outcome.

For time reasons, after various attempts the Oct_F(4H)-I chain was not further investigated.

Based on the suspicion that elimination is the dominant pathway when using a chain with ethylene spacer, a new chain with a shorter methylene spacer (Oct_F(2H)-OH) was investigated.

Oct_F(2H)-chain Attempts of alkylating the linkers with the Oct_F(2H) chain started with the same reaction conditions as for the DEG chain. As preparation, the alcoholic chain was mesylated beforehand. However, no reaction occured. Menczinger *et al.* reported that decreasing the spacer in a fluorinated alkyl chain from ethylene to methylene drastically decreases its reactivity in substitution reactions. To compensate, they changed the leaving group from 4-methylbenzenesulfonate (tosylate) to trifluoromethanesulfonate (triflate).[77] Therefore, the chain was triflated using triflic anhydride and a mild base (pyridine).

After changing the leaving group, alkylation of 2,7-dibromocarbazole was successful. The reaction was done using NaH or KO^tBu in dry DMF and subsequent slow addition of the chain. However, only a very small amount of the desired N-alkylated product formed (yield $4-5$ %). Reaction control by TLC indicated the formation of many by-products. Since all by-products were visible upon UV-illumination on the TLC plate it was assumed that many carbazole derivatives formed. Another indicator for side-reactions was the dark brown color of the reaction mixture since the wanted product is colorless. It was observed, when conducting the alkylation at different temperatures, that the brown color appeared instantly at elevated temperatures (above 80 °C).

Two possible side-reactions were assumed. One was that electrophilic aromatic substitution occured. This would be favoured by the activating effect of the carbazole's nitrogen (even stronger when deprotonated) with *ortho* and *para* directing behavior. The bromine would be slightly deactivating for S_EAr reactions and also *ortho* and *para* directing. The combined influence would favour substitution on positions 1, 3, 6 and 8 (depiction see Fig.20). Also, alkylation of the aromatic system further increases reactivity for further alkylation, which would be a reasonable explanation for the many by-products/TLC spots.

Another hypothesis is that in the desired product, the hydrogen of the methylene spacer in the chain is abstracted by either leftover base or deprotonated carbazole. The negative charge after deprotonation would be stabilized by the negative inductive effect of geminal fluorines and the connected nitrogen. Furthermore, the created double bond would be conjugated

to the aromatic system, further favouring elimination (reaction scheme see Fig.20). This reaction mechanism was already reported by Chen *et al.*, who conducted dehydrofluorination of 2,2,3,3-tetrafluoropyrrolidine derivatives to the corresponding pyrrole in the presence of a strong base at 80 °C in DMSO.[78]

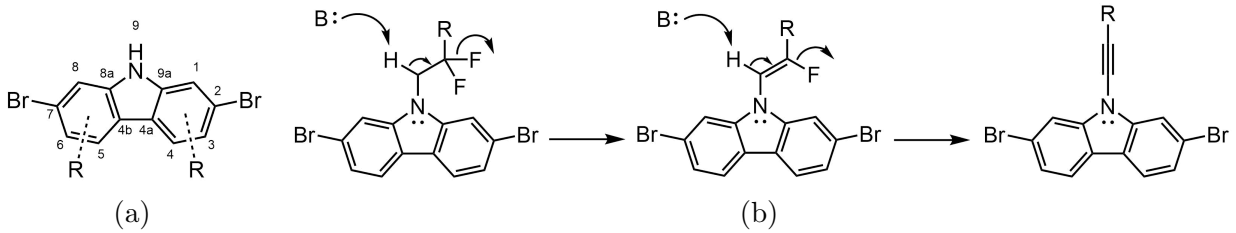

Figure 20: Possible side reactions during alkylation of 2,7-dibromocarbazole and carbazole with triflated side chain; (a) Electrophilic aromatic substitution, favoured on position 1, 3, 6 and 8, (b) base-catalyzed elimination which expands the conjugated system.

Because of generally low yields and time reasons, the by-products were not isolated. Since the assumed side-reactions are both believed to be favoured at higher temperatures (usually high activation energy $\Delta G_R^{\ddagger}$ for S_EAr, entropy gain $-T\Delta S$ for eliminations), a different synthetic pathway was tried to allow low temperatures. Therefore, n-BuLi was tried as strong base. To enable its use, 2,7-dibromocarbazole was replaced with unhalogenated carbazole as substrate. This should prevent metal-halogen exchange reactions, which dominate when using organolithium reagents on aryl halides.[79] Deprotonation was done at −78 °C and addition of the side chain was done at −30 to −20 °C (reaction mixture froze at lower temperatures) in dry THF. The mixture was then allowed to warm to RT (reaction scheme see Fig.21). TLC control indicated the formation of only one product, also at much higher yields as before. This confirmed that side-reactions are favoured at elevated temperatures. Isolation of the compound gave colorless crystals in 10 % yield. ^{1}H NMR analysis confirmed the successful

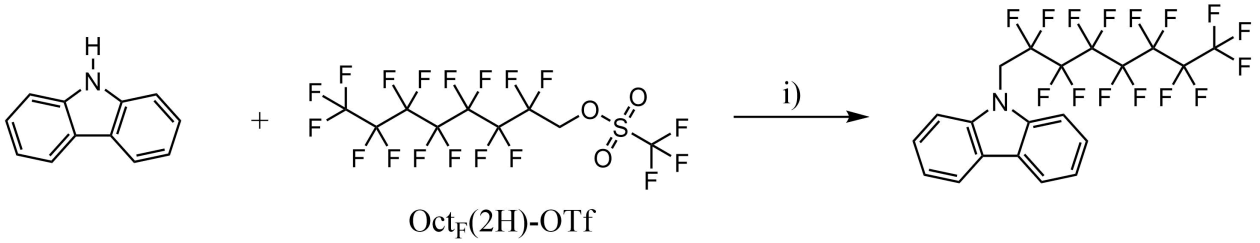

Figure 21: Synthesis scheme alkylation carbazole with n-BuLi: i) Oct$_F$(2H))-OTf, n-BuLi, −78 °C, RT, 30 h (0 %).

N-alkylation and furthermore absence of alkylation on the aromatic system. However, the nitrogen did not seem to be alkylated with the desired chain $Oct_F(2H)$. Main indicator was absence of the expected proton signal with HF coupling of the side chain methylene group in the ^{1}H NMR spectrum. The absence of a methylene signal could be explained by a double elimination promoted by excess of n-BuLi, leading to a triple bond connected to the nitrogen (see Fig.20b). ^{13}C NMR spectroscopy showed multiple potential signals in the region from $100 - 150$ ppm. They indicated the presence of the $Oct_F(2H)$ chain, but confirmation of a triple bond was not definite. Additionally, an APCI-mass spectrum was recorded. There, both signals of the actual desired product ($[M - H]^+ : 548.2$) and the doubly eliminated compound with triple bond ($[M + H]^+ : 510.1$) were found (mass spectrum see Fig.57 in Appendix).

TEG_F-chain Alkylation with the TEG_F chain was first tried with the same conditions as for the DEG chain, using the mesylated TEG_F-OMs. Reaction control by TLC revealed no reaction at RT. Heating above 100 °C led to new spots on the TLC and change of color. ^{1}H NMR analysis, however, usually showed many aromatic as well as aliphatic signals without indication of the desired product. Zeng *et al.* have reported a high tendency of fluorinated triethylene glycoles towards being attacked by nucleophiles such as amides and hydroxides at higher temperatures (110 °C).[80] This could mean that the TEG_F chain is not stable in basic conditions, which would be a plausible explanation for the various TLC spots of the reaction mixture and the many impurities observed in the NMR spectra. Furthermore, Menczinger *et al.* have reported about the drastically decreased reactivity of fluorinated chains with a short methylene spacer (same discussion as for $Oct_F(2H)$ chain).[77] The combination of both findings would suggest a higher success rate when changing the leaving group to the more reactive triflate, and working with a deficit of base at low temperatures. But since it is believed, that the fluorinated ether chains would generally bring problems regarding stability and decomposition, it was not further investigated.

5.1.4 PMI precursor

The PMI molecule was prepared in 3 steps from the starting molecule perylene-3, 4, 9, 10-tetracarboxylic dianhydride (see Fig.22). The first step was a simultaneous decarboxylation and conversion of an anhydride group to an 2, 6-diisopropylphenyl imide to give PMI-H (done by Matiss Reinfelds). The second step was the bromination of the PMI-H to PMI-Br. Using concentrated acetic acid as solvent, high excess of bromine and iodine as catalyst led to high conversion (yield 94 %). This conversion turned out to be straightforward, bearing no synthetic difficulties.

Last step was the exchange of the bromine with a boronic ester group to get PMI-Bpin. This was done in a Miyaura borylation, a Pd catalyzed metal-halogen exchange reaction between bromine and boron. In the beginning, small batches of this step were done, once in inert and once in ambient conditions. Workup of both attempts revealed a high sensitivity of the used catalyst, [1,1´-bis(diphenylphosphino)ferrocene]dichloropalladium(II) [Pd(dppf)Cl_2], to oxygen and/or water. Also, use of not dry KOAc or PMI-Br led to low yields or no reaction at all, confirming the sensitivity to water. When drying all reagents and conducting the reaction in a nitrogen atmosphere, the desired product was obtained exclusively. Purification by flash column chromatography gave PMI-Bpin with 60 % yield.

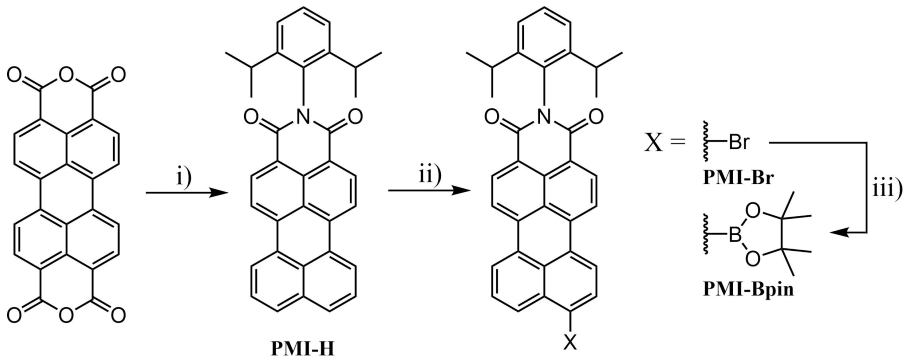

Figure 22: Synthetis scheme of PMI-Bpin: i) *N*-(2,6-diisopropylphenyl)amine, $Zn(OAc)_2$, imidazole, H_2O, 190 °C, RT (done by Matiss Reinfelds); ii) Br_2, I_2 cat., AcOH conc., RT, 24 h (94 %); iii) bis-(pinacolato)diboron, KOAc anh., [Pd(dppf)Cl_2] cat., dioxane anh., N_2, 80 °C, 24 h (60 %).

5.1.5 A-D-A molecules

For connecting the linkers to the PMI units, the classic Suzuki coupling method was used (scheme see Fig.23). Its advantages are high applicability for aryl-aryl bond formation and a high tolerance for functional groups. Also, boronic acids and esters have a high stability against water and oxygen.[81, p.1085-1087][82, p.603] Simultaneously, the used boronates are much less poisonous than e.g. organostannanes, which are used in the related Stille coupling.[83] Used catalyst was the classic $[Pd(PPh_3)_4]$ complex. Changes of the aromatic regions in ^1H NMR spectra are shown in Fig.24, where all PMI species are compared. Full NMR spectra of all products (A-D-A compounds) are attached in the Appendix.

Due to the higher intertness of the boronic ester, the presence of an inorganic base is necessary to accelerate the transmetallation step by forming a boronate anion.[81, p.1085-1087][82, p.603] Two different bases were used for the reactions: aqueous K_2CO_3 with Aliquat 336 as phase transfer catalyst, or aqueous KF with 10 vol% EtOH (respective to the KF volume).

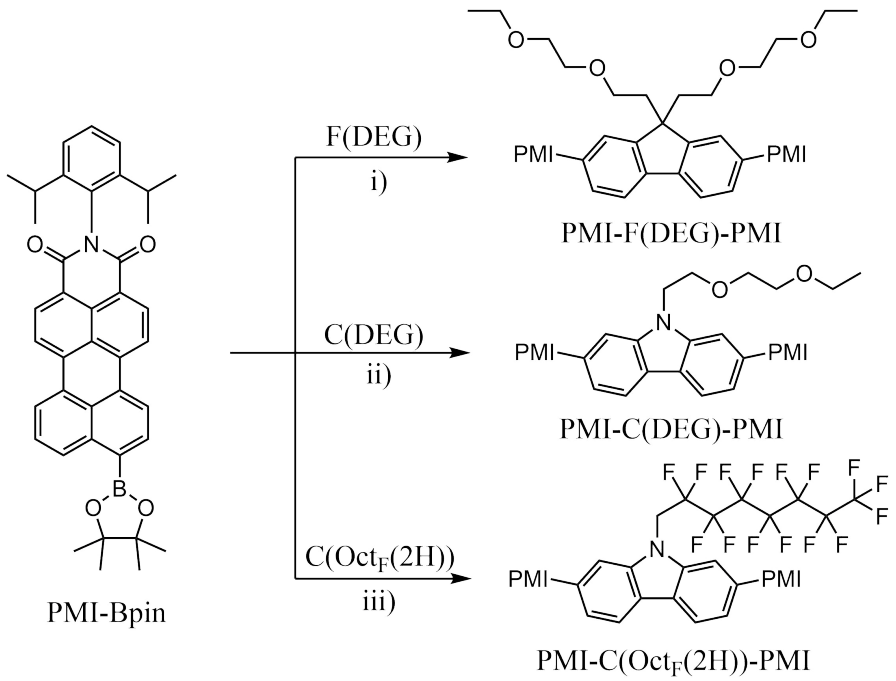

Figure 23: Synthesis schemes of A-D-A compounds: i) F(DEG), 1 M K_2CO_3, Aliquat 336, $[Pd(PPh_3)_4]$ cat., toluene, 110 °C, 5 h (51 %); ii) C(DEG), 1 M K_2CO_3, Aliquat 336, $[Pd(PPh_3)_4]$ cat., toluene, 110 °C, 17 h (12 %); iii) C(Oct$_F$(2H)), 1 M KF, EtOH, $[Pd(PPh_3)_4]$ cat., 110 °C, 17 h (4 %).

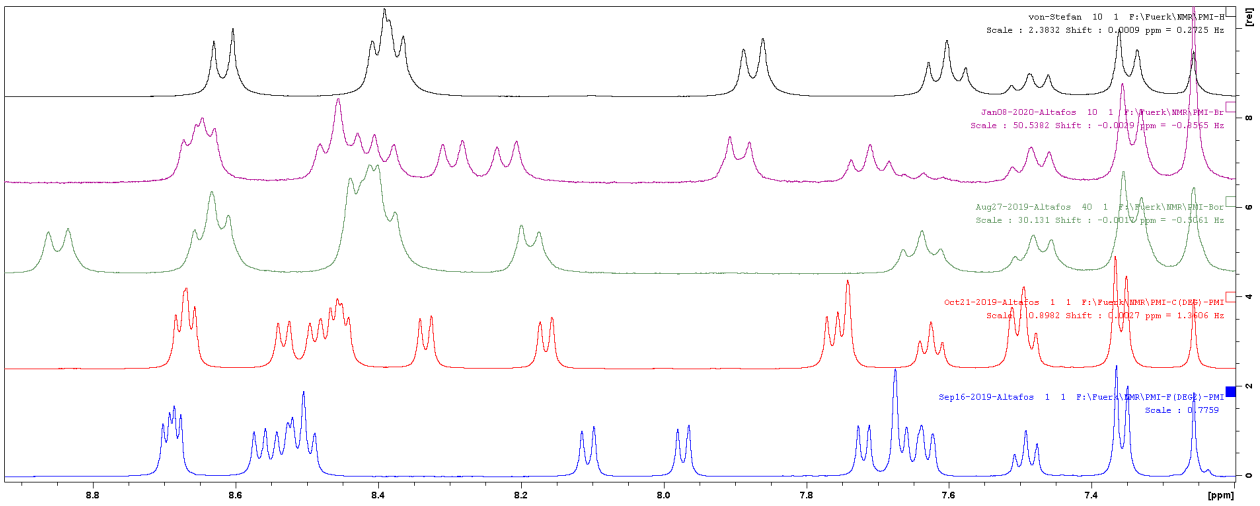

Figure 24: ^{1}H NMR comparison of all PMI compounds, aromatic region of PMI-F(DEG)-PMI (blue), PMI-C(DEG)-PMI (red). PMI-Bpin (green), PMI-Br (violet) and PMI-H (black, measured by Stefan Weber).

For the products with diethyleneglycole chains, PMI-F(DEG)-PMI and PMI-C(DEG)-PMI, it was found that K_2CO_3 with Aliquat 336 achieved higher conversion and less formation of by-products. Both reactions achieved yields of 51 % and 12 %, respectively (in case of PMI-F(DEG)-PMI, the use of KF and EtOH achieved 7 % yield). Flash column chromatography was conducted as first purification step, but did not lead to sufficiently pure products. The final measure was recrystallization, usually multiple times. In case of PMI-F(DEG)-PMI, the pure product was achieved by 2 flash columns with polar and non-polar eluent, to remove higher R_f and lower R_f impurities, respectively. The final step was recrystallization from CH_2Cl_2 and overlaying with twice the volume of methanol as antisolvent. In case of PMI-C(DEG)-PMI, also 2 flash columns were applied, which led to the wanted product and one impurity with almost identical R_f value. The pure product was obtained by three times recrystallization from hot toluene (the use of CH_2Cl_2 and methanol did not lead to separation). When recrystallizing from toluene, NMR analysis indicated the inclusion of 0.8 equivalent toluene into the crystal structure. This is also seen in the TGA analysis, where 2.5 % of weight loss was recorded at 110 °C (see Fig.28b).

For the product with fluorinated side chain PMI-C(Oct_F(2H))-PMI, use of KF with EtOH achieved slightly better results than K_2CO_3. One theory is that the lower basicity of KF compared to K_2CO_3 causes less side-reactions, since it is believed that the methylene hydrogen

of the perfluoroalkyl chain on the carbazole linker is highly CH acidic (electron withdrawing effects of both, the connected nitrogen and CF_2 group). Although slightly better in terms of conversion, the overall yield was still very low with only 4 %. When using K_2CO_3 as base, the PMI-Bpin was fully consumed, even though used in excess. Comparison on TLC indicated that most of the perylene was back-converted to PMI-H by so-called protodeboronation, which was later confirmed by isolation and NMR analysis. Simultaneously, almost little to no product formed. It is assumed, that hardly any cross-coupling occurred, allowing the protodeboronation to take place almost exclusively. Using KF also led to formation of PMI-H, but at a lower rate. The crude product was purified by flash column chromatography and subsequent recrystallization from CH_2Cl_2 and methanol with cooling. The ^{1}H NMR spectrum confirmed the isolation of the desired product, however the aromatic region still showed impurities. TLC showed another spot with an almost identical R_f value (just below the product spot). Its NMR spectrum suggests it to be the homocoupled PMI-PMI due to the absence of carbazole and pinacol signals yet presence of perylene peaks. Also, comparison of the spectrum showed high accordance with that of PMI-H.

Common observations during all coupling attempts were the formation of multiple by-products and low yields. Some isolated and characterized (^{1}H NMR spectroscopy) by-products were the hydrogenated PMI-H and homocoupled PMI-PMI. A reason for the low yields could be the use of partially oxidized, thus inactive, catalyst. The used $[Pd(PPh_3)_4]$ had a brown color, which is a sign for oxidation of the usually yellow compound [84, p.122] into an inactive species, e.g. $[Pt^{II}(O_2)(PPh_3)_2]$.[85, p.1736] The low turnover frequency would then leave time for common side reactions to happen, such as protodeboronation, homocoupling and oxidation (depicted in Fig.25).[86] The pinacol boronic ester group is on one hand much less prone to undergo these side reactions[87], however also hydrolysis of the ester to the boronic acid group possible in the presence of water.[88] An obvious improvement step would be the use of pure, non-oxidized $[Pd(PPh_3)_4]$. One step further would be the general improvement of the catalyst. For example, Buchwald *et al.* have developed reactive Pd complexes with bulky phosphine ligands (so-called Buchwald ligands), which show improved properties in cross coupling reactions, even enabling the use of aryl chlorides.[89] In these ligands, bulky alkyl substituents on the phosphor promote the oxidative addition step with their inductive

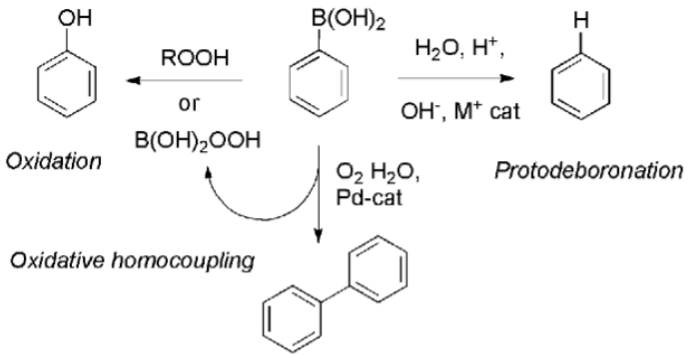

Figure 25: Common side reactions occurring during Suzuki coupling (reproduced from Lennox, A.J. *et al. Israel Journal of Chemistry* **2010**, 50, 664–674, with permission from WILEY-VCH Verlag GmbH & Co. KGaA, Weinheim, 2010[86]).

electron pushing behaviour. Secondly, their bulkiness promotes the reductive elimination step.[82, p.606]

5.2 Compound Characterization

5.2.1 General

All characterization methods were conducted with the glycol products PMI-F(DEG)-PMI and PMI-C(DEG)-PMI. Unfortunately, the fluorinated product PMI-C($\mathrm{Oct_F}$(2H))-PMI was not available in sufficient purity and amount in time to conduct any measurements.

5.2.2 Optical Properties

Absorption as well as emission properties were recorded (in CHCl3). Absorption spectra are shown in Fig.26a, fluorescence spectra in Fig.27. Furthermore, the molar absorption coefficients were determined from multiple measurements at different concentrations (summary see Tab.1). Additionally, optical properties were calculated by DFT computation (see chapter

Table 1: Optical data of the product compounds in CHCl3 wavelength of maximum absorption $\lambda_{max}^{opt.}$ and the corresponding molar absorption coefficient α, optical absorption onset $\lambda_{G}^{opt.}$, stokes shift and quantum yield Φ.

Compound	$\lambda_{max}^{opt.}$ [nm]	$\alpha(\lambda_{max}^{opt.})$ [lmol^{-1}cm^{-1}]	$\lambda_{G}^{opt.}$ [nm] ([eV])	Stokes Shift [µm^{-1}] ([nm])	Φ [%]
PMI-F(DEG)-PMI	530	92.0×10^3	572 (2.17)	0.177 (55)	72 ± 5
PMI-C(DEG)-PMI	532	92.2×10^3	576 (2.15)	0.193 (61)	64 ± 2

5.3.3). PMI-F(DEG)-PMI and PMI-C(DEG)-PMI show an absorption onset $\lambda_G^{opt.}$ at 572 nm (2.17 eV) and 576 nm (2.15 eV) and a maximum absorption $\lambda_{max}^{opt.}$ at 530 nm and 532 nm, respectively. The molar absorption coefficients α at $\lambda_{max}^{opt.}$ are, respectively, around $92.0 \times 10^3\,\mathrm{lmol^{-1}cm^{-1}}$ and $92.2 \times 10^3\,\mathrm{lmol^{-1}cm^{-1}}$, which are typical values for perylene dyes (α of perylene monoimides and diimides usually range in the order of $10^4 - 10^5$ [90][91][92]). Both compounds exhibit a second, smaller maximum at 507 nm ($83.0 \times 10^3\,\mathrm{lmol^{-1}cm^{-1}}$) and 507 nm ($81.5 \times 10^3\,\mathrm{lmol^{-1}cm^{-1}}$), respectively. DFT suggests both peaks corresponding to the HOMO $\rightarrow$ LUMO and HOMO-1 $\rightarrow$ LUMO+1 transitions, respectively. When compared to the smaller PMI-H (Fig.26b), absorption onset as well as maximum absorption are red-shifted as expected. Furthermore, α increased strongly from around $36.0 \times 10^3\,\mathrm{lmol^{-1}cm^{-1}}$ for the PMI-H (measured by Stefan Weber), which was also expected, already because of the doubling of chromophoric units. More interestingly, the change of the side chain from alkyl to glycol does not influence the optical properties. The same acceptors with alkyl chains (hexyl for fluorene and 1-octylnonyl for carbazole, synthesized and characterized by Stefan Weber) show an absorption onset at 574 nm and 577 nm, respectively, for the fluorene and carbazole linked molecule (Fig.26b). This is almost identical to the new compounds. The same is true for $\lambda_{max}^{opt.}$ (531 nm and 533 nm for the alkylated acceptors). This observation agrees with the

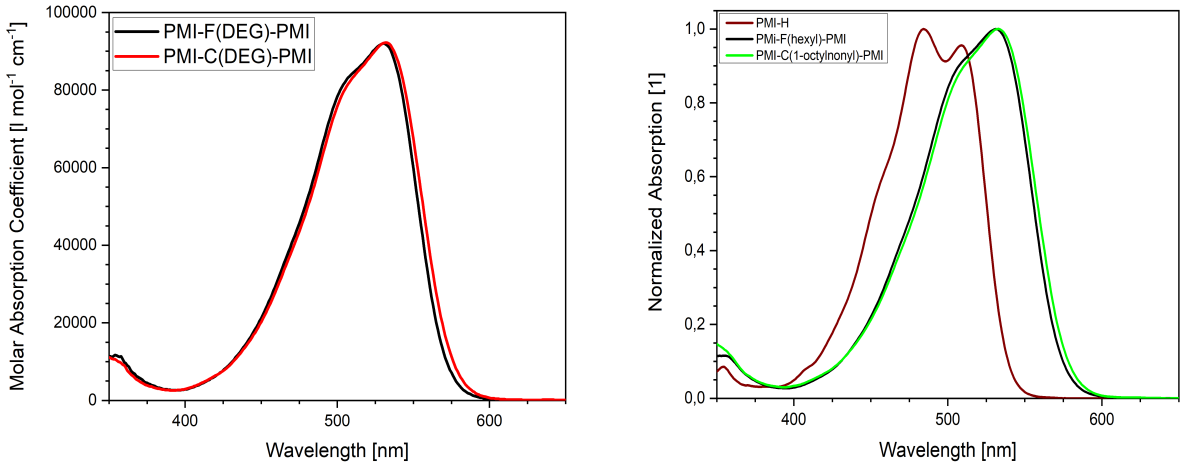

(a) (b)

Figure 26: (a) UV/VIS spectra of PMI-F(DEG)-PMI (black) and PMI-C(DEG)-PMI (red).; (b) UV/VIS spectra of intermediate PMI-H (brown) and related A-D-A compounds with alkyl chains on central atoms, respectively with fluorene PMI-F(hexyl)-PMI (black) and carbazole PMI-FN(1-octylnonyl)-PMI (green) (synthesized and measured by Stefan Weber).

expectation, that side chains which are not directly connected to the chromophoric system will not influence the optical properties of the compound. This offers a convenient pathway to alter the electronic and morphological properties of a given compound without changing its absorption behaviour.

The fluorescence spectra show maximum emissions at 585 nm and 593 nm for PMI-F(DEG)-PMI and PMI-C(DEG)-PMI. Comparing the maximum peaks in the absorption and emission spectra, the Stokes shifts were determined to be $0.177\,\mu m^{-1}$ (55 nm) and $0.193\,\mu m^{-1}$ (61 nm), respectively. Furthermore, the fluorescence quantum yields Φ were calculated with

$$\Phi = \frac{\text{number of photons emitted}}{\text{number of photons absorbed}} = \Phi_{ref} \frac{f_{ref}}{f} \frac{I}{I_{ref}} \frac{n^2}{n_{ref}^2} \tag{5.1}$$

where Φ_{ref} is the known quantum yield of a reference compound (Fluoreszenzorange with a quantum yield of $\Phi_{ref} > 90$ % [93], used 95 %). I is the integrated fluorescence photon flux and n is the refractive index of the solvent. f is the absorption factor at the excitation wavelength, and calculated by $f = 1 - 10^{-A}$ where A is the absorption at the excitation wavelength.[94] PMI-F(DEG)-PMI achieved a yield of 72 ± 5 %, PMI-C(DEG)-PMI of 64 ± 2 %. Having high quantum yields is desirable for materials in OSCs, because it indicates a small rate of non-radiative recombinations of the electron-hole pairs. Fluorescence results are listed in Tab.1.

Table 2: Optical data of thin films: wavelength of maximum absorption $\lambda_{max}^{opt.}$ with relative intensity I_{rel} and optical absorption onset $\lambda_G^{opt.}$.

Thin film	$\lambda_{max}^{opt.}$ (I_{rel}) [nm] ([1])	$\lambda_G^{opt.}$ [nm] ([eV])
PMI-F(DEG)-PMI	482 (1)	560 (2.21)
PMI-C(DEG)-PMI	487 (1)	578 (2.14)
PBDB-T	576 (1) , 533 (0.91)	632 (1.96)
PBDB-T : PMI-F(DEG)-PMI	490 (1), 576 (0.71)	621 (2.00)
PBDB-T : PMI-C(DEG)-PMI	512 (1), 573 (0.82)	624 (1.99)

Besides in solution, UV/VIS absorptions of thin films were measured. Investigated films were both, pure acceptor layers (PMI-F(DEG)-PMI and PMI-C(DEG)-PMI) as well as donor:acceptor blends identical to those applied in solar cells (donor PBDB-T, ratio D:A 1:1 (w:w)). They are shown in Fig.27, characteristic values are summarized in Tab.2. Compared

with the measurements in chloroform, thin films of the pure acceptors show approximately similar absorption onsets at 560 nm and 578 nm for PMI-F(DEG)-PMI and PMI-C(DEG)-PMI, respectively. The wavelengths of maximum absorption show a hypsochromic shift for both acceptors, now being at 482 nm and 487 nm.

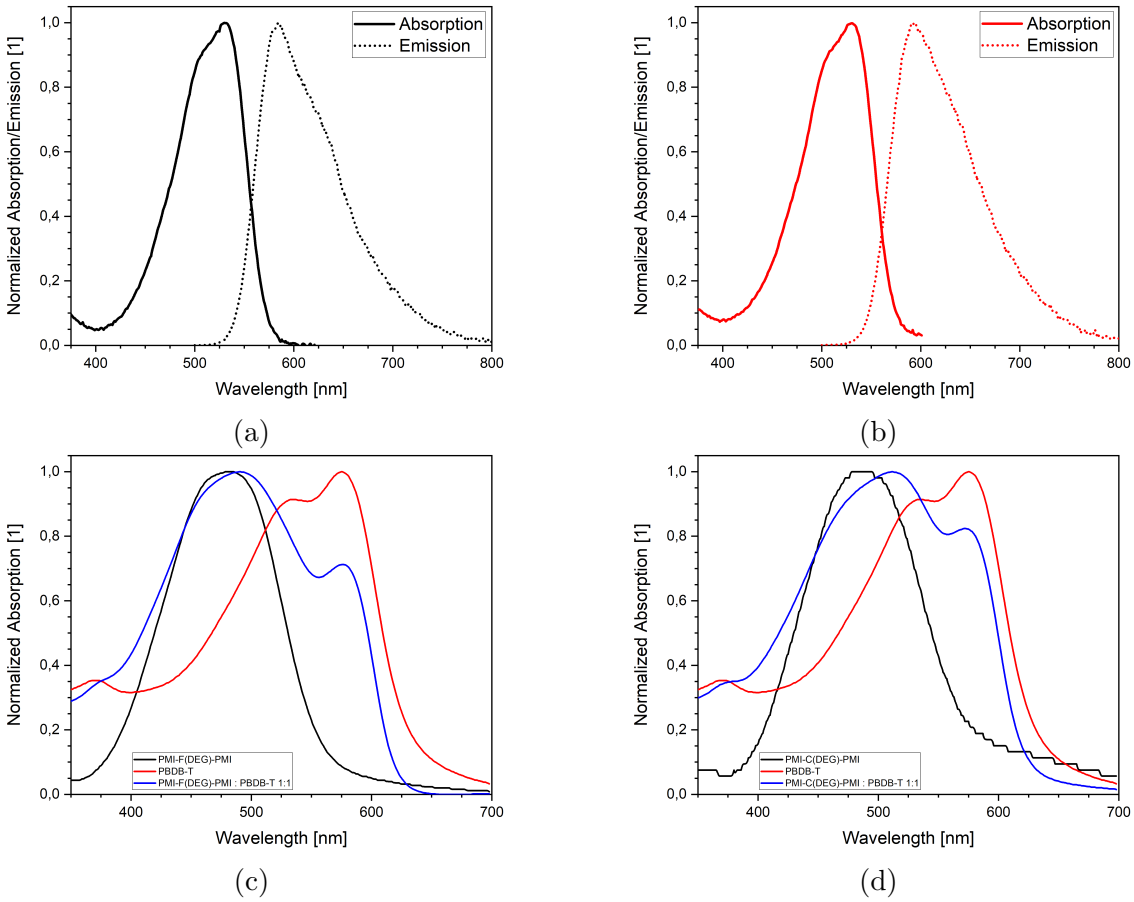

Figure 27: UV/VIS absorption and fluorescence spectra in $CHCl_3$ of PMI-F(DEG)-PMI (a) and PMI-C(DEG)-PMI (b); UV/VIS absorption spectra of thin films of PMI-F(DEG)-PMI, PBDB-T and blend (D:A 1:1) (c) and PMI-C(DEG)-PMI, PBDB-T and blend (D:A 1:1) (d).

This could be explained by a, to a certain degree, H-type aggregation behaviour in solid state compared to solution. As calculated by DFT, the absolute dipole vectors of both products lie in the linker plane, facing towards the DEG chains. Furthermore, the linker has an angle in respect to the PMI plane of $\alpha \sim 55$ ° (more detailed discussion see chapter 5.3.2, p.40). If strong $\pi - \pi$ stacking occurs, the tilted linkers would lead to a mix of in-line and parallel alignment of the electric dipoles. This would be in agreement with the necessary parallel alignment of dipole moments for H-type aggregation.[28] A similar behaviour for

perylene imides has already been reported by Raj *et al.*, who observed strong $\pi - \pi$ stacking of PDI molecules.[95]

The absorption windows of both, donor and acceptor, complement each other with that of the polymer donor PBDB-T, which absorbs already at longer wavelengths (absorption onset at 632 nm). This results in a larger total absorption window of the bulk heterojunction in solar cells, which increases the light harvesting potential of the device.

5.2.3 Thermal Properties

Thermal properties were determined by thermogravimetric analysis (TGA) and differential scanning calorimetry (DSC), conducted by Josefine Hobisch (TU Graz). Also, the glass transition temperatures were determined. The recorded curves are shown in Fig.28.

PMI-F(DEG)-PMI behaves stable at lower temperatures. It has the glass transition T_g at 222 °C. Melting point is at 345 °C, followed by endothermic decomposition, which starts at 400 °C. First slight mass loss slowly starts at approximately $320 - 330$ °C, increasing when nearing the maximum decomposition peak. The total weight loss after reaching the final temperature (550 °C) is 28.66 %. Loss of both DEG chains would correspond to a weight loss of 17.4 %, so further decomposition than just simple side chain dissociation occurs.

PMI-C(DEG)-PMI shows a weight loss of 2.5 % over a temperature range from $100-200$ °C. This is probably evaporating toluene. During the recrystallization of the product from hot toluene it is believed that some amount gets incorporated into the crystal structure. This was also observed in the NMR spectrum. The weight loss of 2.5 % would correspond to an incorporation of approx. 0.33 eq. toluene. Upon further heating, the mass stays constant until decomposition starts at approximately 440 °C. The overall weight loss at 550 °C is 24.28 %. Glass transition occurs at 276 °C, shortly followed by another signal at 285 °C. A third transition is present at 358 °C. One of them could correspond to a melting point. However, the signals are relatively weak, so also different changes could happen, like crystallization or phase-transformation processes.

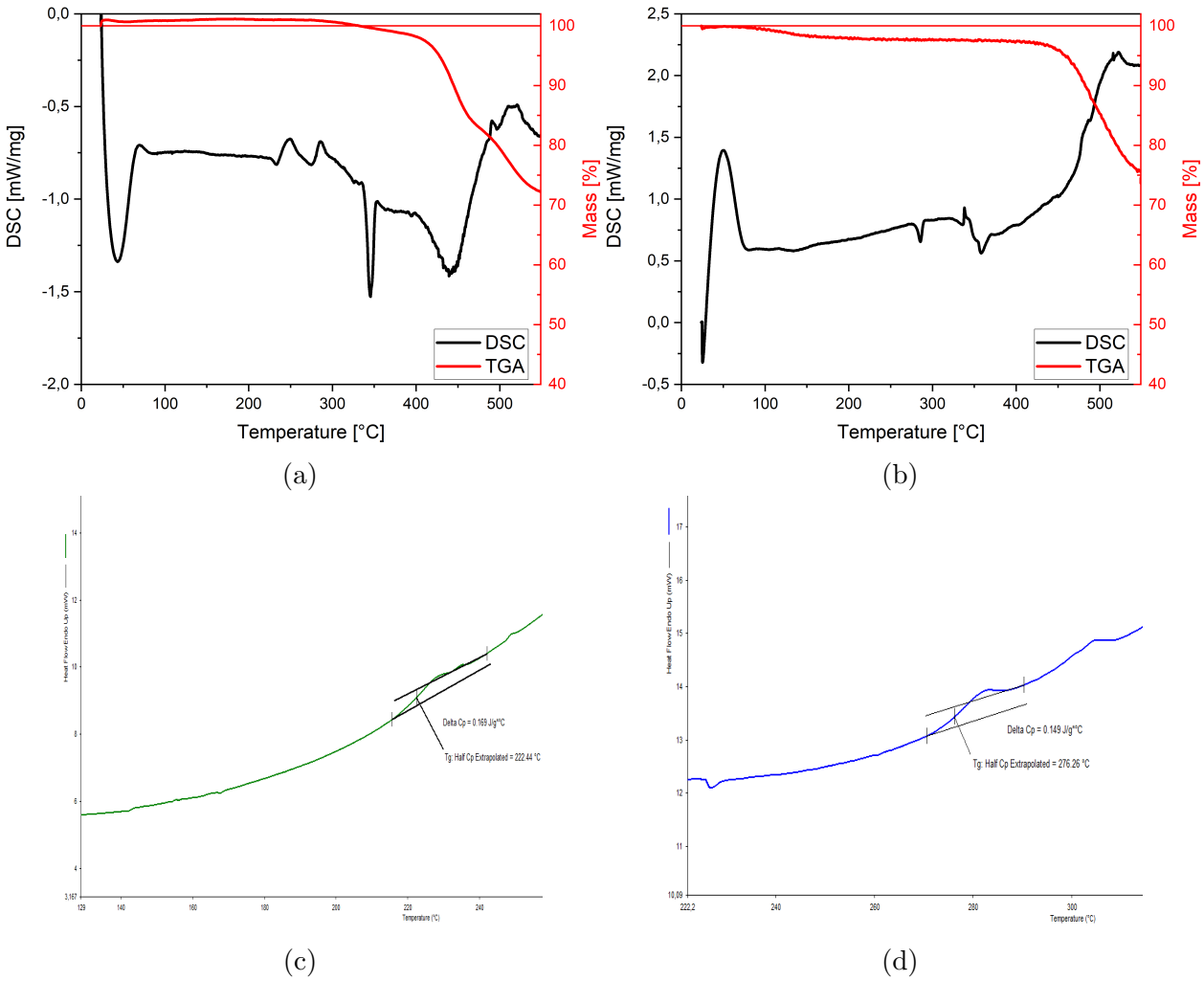

Figure 28: TGA and DSC of PMI-F(DEG)-PMI (a) and PMI-C(DEG)-PMI (b); Close-up on glass transition T_g in second heating gradient of PMI-F(DEG)-PMI (c) and PMI-C(DEG)-PMI (d).

5.3 DFT-Calculation

5.3.1 Approximations

All DFT calculations were conducted with the B3LYP functional together with 2 different basis sets, the smaller 6-31G* set and bigger, diffuse 6-31+G* set. General approach was a first optimization of the geometry. If successful, next step was calculation of the vibrational frequencies as stability test for the geometry. If the obtained frequencies were physically meaningful (not negative), third and last step was the calculation of optical properties together with orbital shapes. The used DFT codes are attached in the Appendix. Attempts to do orbital calculations for the acceptors with full side chain length all failed, because the

iterations did not converge to a solution within the maximum cycles. Therefore, the molecule was divided. First, the linker molecules alone with full chain length were examined to see qualitative changes in energy levels caused by the new side chains. In addition, simplified A-D-A molecules were calculated.

The linker molecules alone were considered without bromine on the aromatic system. All geometry and orbital calculations were successful with the diffuse 6-31+G* basis set in gas phase. Linker molecules with simple octyl chains were also calculated as reference. The results are listed in Tab.4.

For the A-D-A molecules, 2 different conformations were examined for all compounds, one with *syn* alignment of the aromatic PMI units, and another with *skewed* conformation (more detailed discussion see chapter 5.3.2). Calculating the complete A-D-A molecules was attempted several times, but usually failed with the diffuse basis set 6-31+G*. A first simplification was the change of the *N*-stubstituent at the imide from the large 2,6-diisopropylphenyl to a simpler isopropyl group. This led to successful geometry optimization and frequency calculation. The calculation of the optical properties, however, still failed, even after increasing the maximum number of iteration cycles. The next simplification was shortening of the side chains 8 to 4 atoms. 4 was chosen to still include oxygen atoms in the glycole chain plus a methyl endgroup (to avoid a potentially misleading -OH endgroup). That way, orbital calculation was successful for the carbazole products with just one side chain PMI-C(DEG)-PMI and PMI-C($\mathrm{Oct_F}$(2H))-PMI with *syn* conformation. For the fluorene type molecules with twi side chains, PMI-F(DEG)-PMI and PMI-F($\mathrm{Oct_F}$(2H))-PMI, and the *skewed* geometries, only change to the smaller basis set 6-31G* achieved a successful calculation.

5.3.2 Geometric Properties

It was examined that the A-D-A compounds adopted two different geometries during geometric pre-optimization (done in Chem3D and Avogadro). One was a *syn* ($\parallel$) alignment of the PMI units ($\beta \sim 0°$, see Fig.29) with a tilted linker molecule ($\alpha > 0°$). The second showed *skewed* ($\angle$) PMI units ($\beta > 0°$), which was usually observed when two side chains were present (fluorene). Since it was assumed that the exact DFT iterations would easily be "trapped"

within a pre-set local energy minimum, both conformations were examined separately for each A-D-A molecule. The obtained conformation angles and energy values H_F are listed in Tab.3(p.41) and Tab.5 (p.43), respectively. Comparison revealed that for all compounds with fluorene (two side chains) as linker, the *skewed* conformation is favoured, while for carbazole (one side chain), the *syn* conformation is favoured. The same trend was observed in both, gas phase and solvent environment. The calculated energy differences are relatively small compared to RT. So, rotation is unhindered and happens at a high rate (in solution) at room temperature. This fits with the NMR results, where no isomers for any of the 3 synthesized products were observed. The *syn* conformation generally has an angle β around zero between the PMI planes and a tilted linker molecule with an angle $\alpha_1 = \alpha_2$ of $57 - 59°$. The *skewed* conformation showed an angle β of ~ 180 ° between the PMI units, and a similar angle of the linker ($\alpha_1 \sim 58°$) for the fluorene acceptors. Differently, in the carbazole acceptors the PMI units have a higher angle β of $104 - 114°$.

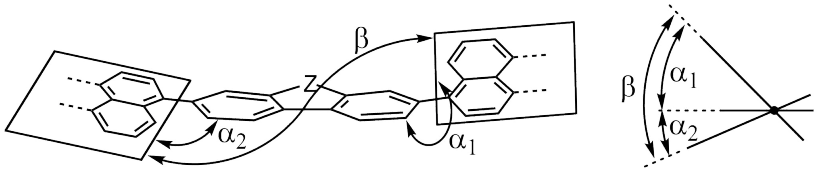

Figure 29: Investigated angles in A-D-A molecules, α_1 and α_2 between aromatic planes of PMI units and linker molecule, respecitvely, β between the PMI units; side view on the right with horizontal linker molecule and *skewed* PMI units.

Table 3: Calculated angles in A-D-A molecules: α_1 and α_2 between aromatic planes of PMI units and linker molecule, respecitvely, β between the PMI units. Favoured conformation with the respective energy difference to the unfavoured, both in gas phase (ΔE_g) and chloroform environment (ΔE_s), calculated by DFT with the 6-31G* basis set.

Molecule	Conf.	α_1 [°]	α_2 [°]	β [°]	Fav. conf.	ΔE_g / ΔE_s [kJ/mol]
PMI-F(DEG)-PMI	∥	57.6	57.9	0.3		
PMI-F(DEG)-PMI	∠	58.5	235.7	177.2	×	4.17 / 5.46
PMI-F(Oct_F(2H))-PMI	∥	59.6	59.7	0.1		
PMI-F(Oct_F(2H))-PMI	∠	58.0	235.3	177.3	×	7.22 / 6.61
PMI-C(DEG)-PMI	∥	58.4	58.4	0.0	×	1.15 / 1.12
PMI-C(DEG)-PMI	∠	236.3	122.8	113.5		
PMI-C(Oct_F(2H))-PMI	∥	57.8	57.8	0.0	×	1.00 / 1.24
PMI-C(Oct_F(2H))-PMI	∠	235.1	130.7	104.4		

5.3.3 Optical Properties

Linkers Geometric as well as optical DFT calculation of the linker molecules was successful with the diffuse basis set 6-31+G* for all molecules. The results, including energy of the HOMO and LUMO level, optical bandgap and wavelength of maximum absorption are summarized on Tab.4. Comparison with the alkyl chains shows a slight lowering of HOMO and LUMO orbitals when changing to the glycol chain and a stronger lowering when introducing the perfluoro alkyl chain. Also, the optical bandgap increases slightly.

Table 4: DFT results of linker molecules: Absolute electric dipolemoment μ_{tot}, energy of HOMO (E_{HOMO}) and LUMO (E_{LUMO}) and optical bandgap $E_G^{opt.}$, Values calculated using the 6-31+G* basis set in gas phase.

Molecule	μ_{tot} [D]	E_{HOMO} [eV]	E_{LUMO} [eV]	$E_G^{opt.}$ [eV]
F(octyl)	0.67	-5.97	-1.07	4.49
F(DEG)	0.37	-6.08	-1.18	4.50
F($\mathrm{Oct_F}$(2H))	2.66	-6.40	-1.48	4.54
C(octyl)	2.16	-5.55	-1.02	4.39
C(DEG)	2.09	-5.65	-1.08	4.41
C($\mathrm{Oct_F}$(2H))	1.65	-5.97	-1.26	4.47

A-D-A molecules Optical properties were calculated successfully for all 4 A-D-A molecules (fluorene and carbazole with DEG and $\mathrm{Oct_F}$(2H) cain, respectively) using the 6-31G* basis set. Each molecule was calculated in gas phase and chloroform environment, as well as in *syn* and *skewed* conformation. All results are shown in Tab.5.

Generally, differences of HOMO and LUMO energies between *syn* and *skewed* conformation are relatively small (< 0.05 eV). Same is true for the maximal absorption wavelength $\lambda_{max}^{opt.}$, which varies only within a few nm. An interesting observation is, that molecules with a lower geometric energy H_F do not necessarily have lower lying HOMO levels. All qualitative trends are similar, in gas phase and chloroform environment. However, the absolute values differ slightly. The absolute dipole moment increases significantly in chloroform and $\lambda_{max}^{opt.}$ is shifted to longer wavelength (~ 20 nm). HOMO and LUMO energies are lower in gas phase, in a range of 0.05 eV.

Comparison of DFT values to the experimentally determined properties (compare Tab.1,

Table 5: DFT results of A-D-A molecules: Molecular energy H_F, absolute electric dipolemoment μ_{tot}, energy of HOMO (E_{HOMO}) and LUMO (E_{LUMO}), optical bandgap $E_G^{opt.}$ and wavelength of maximum absorption $\lambda_{max}^{opt.}$. Values calculated using the 6-31G* basis set in gas phase and $CHCl_3$ environment, calculations done with *syn* ($\parallel$) and *skewed* ($\angle$) conformation of the PMI units.

Linker	Env.	Conf.	H_F [E_h]	μ_{tot} [D]	E_{HOMO} [eV]	E_{LUMO} [eV]	$E_G^{opt.}$ [eV]	$\lambda_{max}^{opt.}$ [nm]
F(DEG)	gas	$\parallel$	-3221.7177513	3.02	-5.36	-2.85	2.31	533
F(DEG)	gas	$\angle$	-3221.7193403	1.75	-5.42	-2.85	2.35	528
F(DEG)	$CHCl_3$	$\parallel$	-3221.7356747	3.97	-5.34	-2.83	2.25	552
F(DEG)	$CHCl_3$	$\angle$	-3221.7377555	2.46	-5.36	-2.83	2.26	548
$F(Oct_F(2H))$	gas	$\parallel$	-4539.2568637	4.46	-5.46	-2.91	2.35	524
$F(Oct_F(2H))$	gas	$\angle$	-4539.2596143	4.05	-5.45	-2.89	2.35	526
$F(Oct_F(2H))$	$CHCl_3$	$\parallel$	-4539.2743711	5.51	-5.38	-2.84	2.28	544
$F(Oct_F(2H))$	$CHCl_3$	$\angle$	-4539.2768873	5.15	-5.37	-2.84	2.27	546
C(DEG)	gas	$\parallel$	-3044.6341198	1.94	-5.39	-2.83	2.34	529
C(DEG)	gas	$\angle$	-3044.6336812	2.04	-5.40	-2.82	2.36	524
C(DEG)	$CHCl_3$	$\parallel$	-3044.6515358	2.59	-5.34	-2.82	2.25	550
C(DEG)	$CHCl_3$	$\angle$	-3044.6511092	2.69	-5.35	-2.81	2.27	545
$C(Oct_F(2H))$	gas	$\parallel$	-3703.3999197	3.93	-5.42	-2.86	2.34	530
$C(Oct_F(2H))$	gas	$\angle$	-3703.3995392	2.65	-5.41	-2.86	2.34	531
$C(Oct_F(2H))$	$CHCl_3$	$\parallel$	-3703.4169527	4.91	-5.36	-2.83	2.26	549
$C(Oct_F(2H))$	$CHCl_3$	$\angle$	-3703.4164806	3.43	-5.35	-2.83	2.25	550

p.34) shows good agreement for $\lambda_{max}^{opt.}$. Experimental values are at ~ 530 nm, whereas DFT values are at $524 - 533$ nm for gas phase and $548 - 552$ nm for solvent environment. The bandgap is slightly larger in all DFT conditions, ranging around $2.25 - 2.36$ eV. Experimental values are 2.17 eV and 2.15 eV for PMI-F(DEG)-PMI and PMI-C(DEG)-PMI, respectively. In agreement with the experimental absorption spectra, the computated spectra also show a second, smaller peak at shorter wavelengths. Both transitions (main and side transition) correspond to HOMO $\rightarrow$ LUMO and HOMO-1 $\rightarrow$ LUMO+1 transition. Examining the orbital shapes, the main transition (HOMO $\rightarrow$ LUMO) corresponds to a charge transfer excitation, since charge shifts from the central linker to outer PMI units (see Fig.30). The second transition (HOMO-1 $\rightarrow$ LUMO+1), on the other hand, corresponds to a localized excitation on the PMI units (for both PMI-F(DEG)-PMI and PMI-C(DEG)-PMI). The two main computated transitions are summarized in Tab.6.

Besides characteristic values, the shapes of the HOMO and LUMO were calculated. They are shown in Fig.30 exemplary for PMI-C(DEG)-PMI, respectively in *syn* and *skewed*

Table 6: Main optical transitions of A-D-A molecules with oscillator strength f, calculated with 6-31G* basis set in gas phase.

Molecule	Transition	ΔE [eV (nm)]	f [1]
PMI-F(DEG)-PMI	HOMO → LUMO	2.34 (530)	1.366
	HOMO-1 → LUMO+1	2.54 (488)	0.566
PMI-C(DEG)-PMI	HOMO → LUMO	2.35 (529)	1.347
	HOMO-1 → LUMO+1	2.54 (488)	0.561

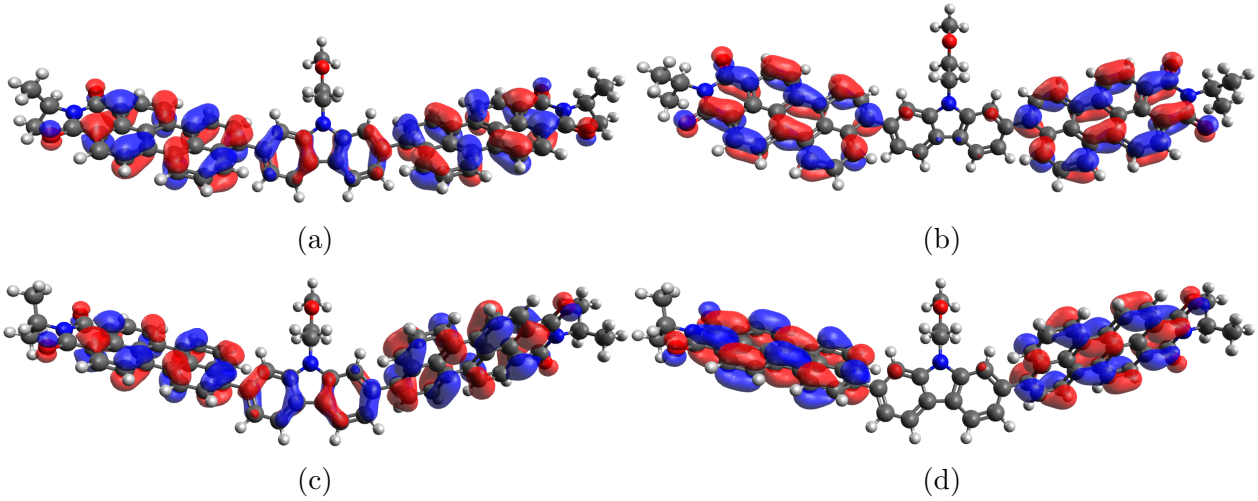

Figure 30: Graphical representation of HOMO and LUMO of the A-D-A molecules (isopropyl as *N*-substituent, side chain shortened to 4 atoms) with *syn* (∥) and *skewed* (∠) conformations, calculated with 6-31G* basis set: PMI-C(DEG)-PMI ∥ HOMO (a) and LUMO (b), PMI-C(DEG)-PMI ∠ HOMO (c) and LUMO (d).

conformation. Similar features for all molecules are fully delocalized HOMOs and separated LUMOs, which exclude the linker molecule. In any case, the change in orbital localization between HOMO and LUMO agrees with the initial idea of making a molecule with electron acceptor-donor-acceptor units. This supports intramolecular charge transfer and can lead to strong and broad absorption in the visible range.[96]

In summary, the DFT calculations led to accurate values for the optical parameters, even despite the simplification of the geometry. The obtained results confirm the expected independence of the optical properties (bandgap, position and magnitude of excitations) from the introduced chains. This makes side chain modification an useful way to selectively tune other properties, such as solubility, crystallization behaviour and permittivity. Their influence on the preferred geometry was also shown. Furthermore, the desired A-D-A behaviour could be confirmed, as seen by the shift of charge between HOMO and LUMO from the linker to the PMI units.

5.4 Solar Cells

5.4.1 Fabrication

Solar cells were made from the two acceptors with glycole chains, PMI-F(DEG)-PMI and PMI-C(DEG)-PMI. All cells were built using an inverted architecture with following layers: substrate/ITO/ZnO/D:A/MoO_x/Ag. Therein, the ITO functions as electron collecting cathode and the silver counter electrode functions as hole collecting anode (see Fig.5a). The active layers were fabricated as bulk heterojunction with PBDB-T as donor. To examine effects of layer thickness on the device performance, layer deposition was usually done with different spin coating speeds. Preparation of the annealing substrates was then done with the same spin coating parameters as for most efficient solar cells (3000 min^{-1} for both acceptors). A beneficial feature of both acceptors is their high solubility (especially of the fluorene-type acceptor) in many solvents, including chloroform and chlorobenzene, which was used for spin coating. So, active layer deposition generally achieved homogeneous layers (visual impression) with sufficient thicknesses. The PMI-C(DEG)-PMI showed slightly worse solubility in CB. The active layers also showed dark dots, which were small crystals of undissolved acceptor material. It is assumed, that PMI-C(DEG)-PMI has a higher degree of crystallinity and worse solvation behaviour since it has one side chain less (smaller entropy gain upon solvation, also better crystallization behaviour). Microscope pictures of the active layers are shown in Fig.31, where undissolved crystallites can be seen.

Since in bulk heterojunctions, both donor and acceptors are connected to either electrode, charge carrier recombination can be a problem. To avoid that, buffer layers were put between the active layer and electrodes. ZnO was used as electron transport layer (ETL) and MoO_x as hole transport layer (HTL). Their conduction and valence bands have suitable energies which only favour the transport of electrons or holes, respectively, while blocking the other. This significantly reduces the recombination rate of free charge carriers, leading to a higher fill factor.[97]

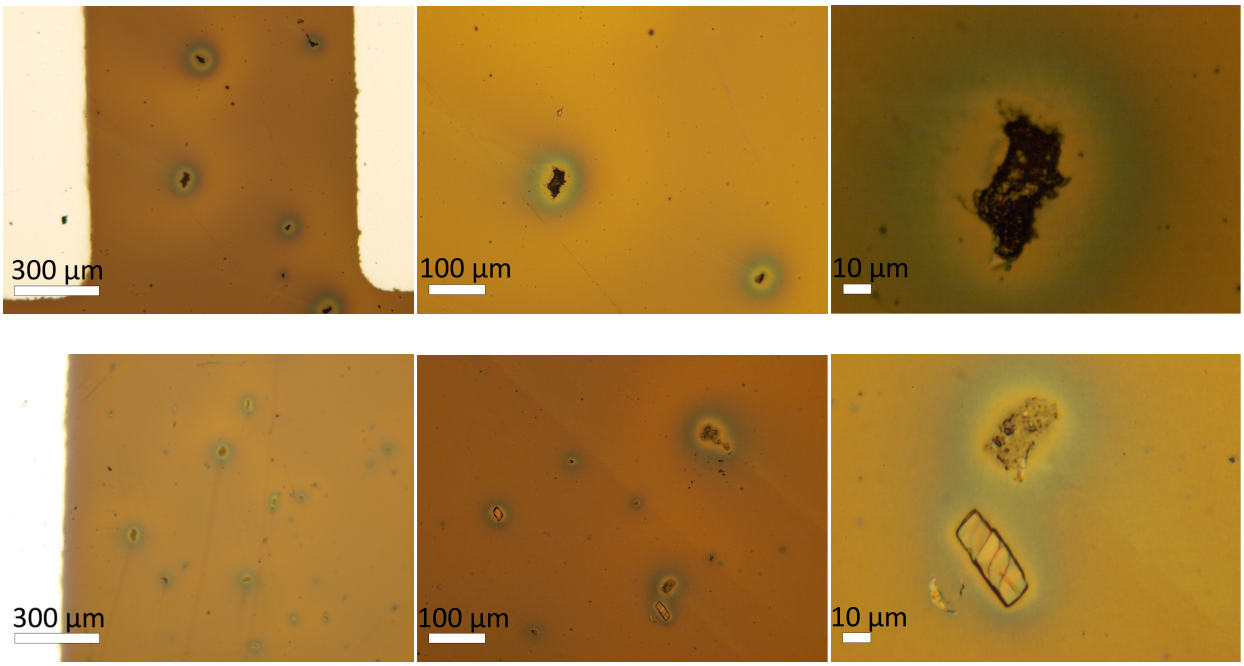

Figure 31: Optical microscope pictures of active layers of PMI-F(DEG)-PMI (above) and PMI-C(DEG)-PMI (below), recorded in reflection mode with 100-fold (left), 200-fold (middle) and 1000-fold (right) magnification.

5.4.2 J-V Curves

JV curves were recorded for each SC type under dark, illuminated, light soaked and annealed conditions. Curves of the cell with best performance are depicted in Fig.32, respectively for the PMI-F(DEG)-PMI type and PMI-C(DEG)-PMI type SC. The exact values for each produced film thickness of the active layer are listed in Tab.7, 8 and 9 for the fluorene type SCs and Tab.10, 11 and 12 for the carbazole type SCs.

The **fluorene** type SCs showed a typical PCE of $0.9-1.2$ % with the best cell at 1.32 %. FF ranged at $37-42$ %, V_{oc} at $0.87-0.92$ V and J_{sc} at $1.9-3.8$ mA/cm^2. Devices with thinner active layers ($\sim 80-90$ nm) generally showed higher performances. Tab.7 shows higher PCE at thicker and thinner layers with a minimum in between, caused by lower J_{sc} and FF values. Light soaking the substrates for 4 minutes slightly, but not significantly increased the PCE. This was due to slight increase of J_{sc} while FF and V_{oc} stayed constant. Light soaking effects can be caused by the ZnO layer. Jiang *et al.* have reported that upon illumination the usually low charge carrier density in the ZnO layer increases. This reduces the width of the depletion region which then allows more charge carriers to tunnel through the active

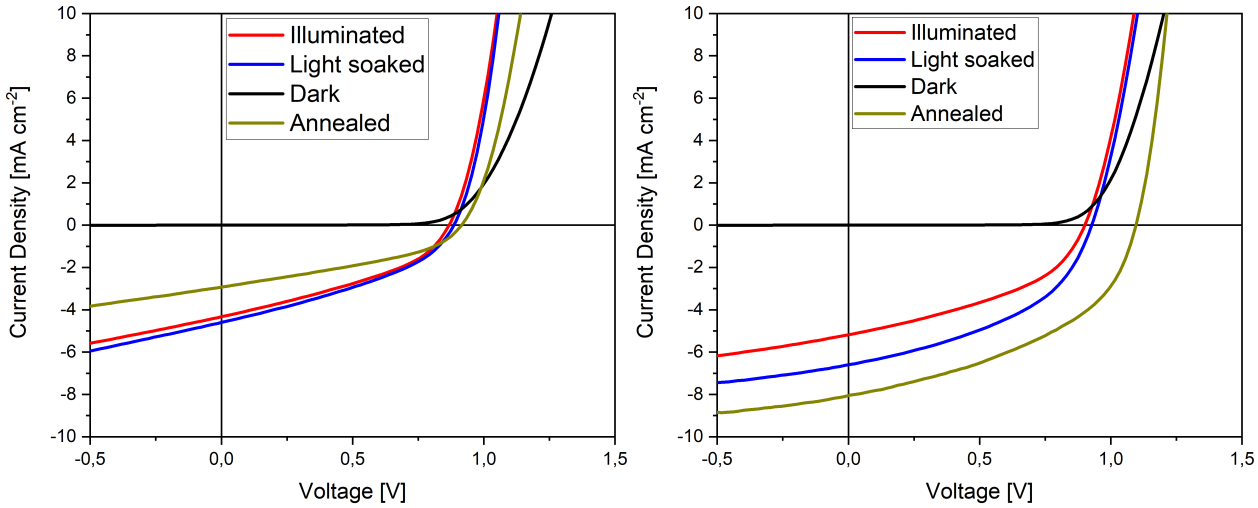

Figure 32: J-V curves of SC series with PMI-F(DEG)-PMI (left) and PMI-C(DEG)-PMI (right) as acceptor material, respectively, and PBDB-T as donor (ratio 1:1); 4 curves recorded under dark (black) and illuminated (red) conditions, after 4 minutes light soaking (blue) and 5 min annealing (green, depicted for 190 °C for PMI-F(DEG)-PMI and 170 °C for PMI-F(DEG)-PMI).

layer/ETL and ETL/cathode interfaces, increasing the device's current density.[98] Annealing within the chosen temperature range ($170 - 250$ °C) did not lead to significant changes. A trend of the characeristic solar cell parameters as function of annealing temperature is shown in Fig.33a, the corresponding values are listed in Tab.9. All trendlines show a relatively constant behaviour across the temperature range, which means all changes happen before 170 °C. Since TGA/DSC analysis showed no transitions for the PMI-F(DEG)-PMI before its glass transition at 222 °C, the changes could be predominantly caused by the donor polymer PBDB-T, which has a wide glass transition region at $105 - 210$ °C.[99]

The **carbazole** type SCs reached higher efficiencies, mostly due to a higher J_{sc} . FF and V_{oc} were almost identical to the fluorene type. The J_{sc} values are ranging at $3.6 - 4.8$ mA/cm^2, leading to PCE values of $1.4 - 2.0$ % with a maximum of 2.03 %. Trends of PCE vs. layer thickness show the best performance at medium thicknesses ($\sim 90 - 130$ nm), which decreases for thinner and thicker layers. Light soaking again led to a slight increase of J_{sc} ($4.0 - 6.4$ mA/cm^2), raising the PCE to $1.8 - 2.5$ %. Annealing achieved a significantly improved PCE of $3.3 - 3.7$ %, caused by an increase of both, V_{oc} and J_{sc} ($1.0 - 1.1$ V and $7.0 - 7.8$ mA/cm^2). The annealing trends can be seen in Fig.33b, the values in Tab.12. Since the glass transition of PMI-C(DEG)-PMI is even higher (276 °C) and the parameters also show relatively constant behaviour within the temperature range, the same assumption can

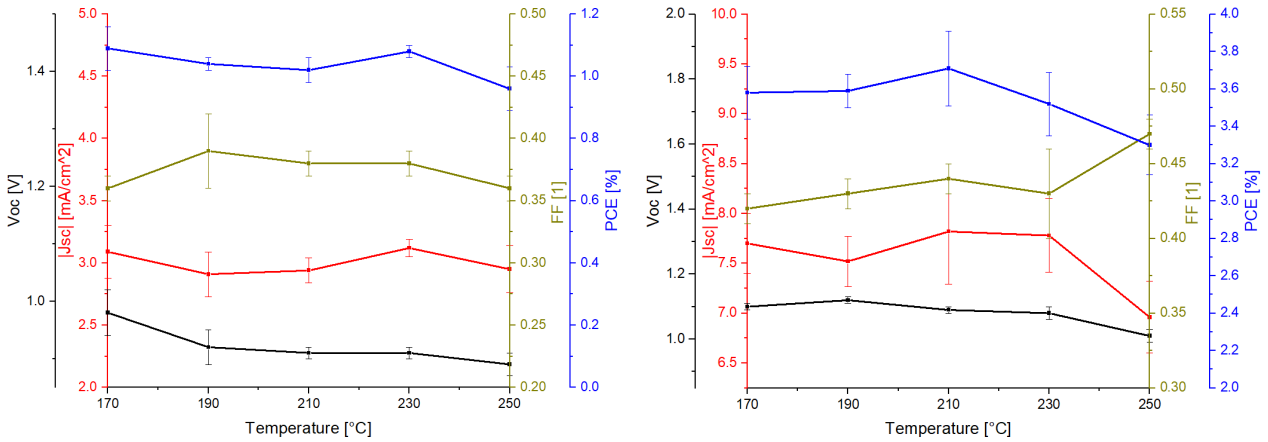

Figure 33: Trend of characteristic parameters V_{oc} (black), J_{sc} (red), FF (green) and PCE (blue) as function of the annealing temperature: (a) PBDB-T : PMI-F(DEG)-PMI (1:1 w:w); (b) PBDB-T : PMI-C(DEG)-PMI (1:1 w:w). Mean values calcd. from 5 best cells, respectively.

be made as for the fluorene type SCs, meaning a main influence of the donor on the annealing behaviour. However, in this case changes within the SC seem to greatly improve charge carrier transport. Also, the increased V_{oc} indicates a reduction of the collective series resistance R_s. This can also be seen from the steeper slope of the annealed JV curve at the linear region $V > V_{oc}$. As explained in chapter 2.1.2 (p.6), R_s is inversely proportional to the slope in this region, so a steeper JV curve indicates a smaller R_s. The shunt resistance R_{sh}, on the other hand, does not seem to be influenced by annealing (estimated by the inverse slope at $V \sim V_{oc}$).[29] The highest performance is achieved at 210 °C. At higher temperatures, both V_{oc} and J_{sc} decrease, leasing to smaller PCE values.

Table 7: J-V data for PMI-F(DEG)-PMI series (donor: PBDB-T, D:A 1:1, 10 mg/ml, no annealing, no light soaking): Average values calc. from 5 best cells, respectively; shown for each spin coating speed v with average film thickness t (averaged from 3 measurements), maximum values in brackets.

v [min^{-1}]	t [nm]	V_{oc} [V]	J_{sc} [mA/cm^2]	FF [1]	PCE [%]
500	375 ± 53	0.92 ± 0.02 (0.95)	-2.58 ± 0.24 (-2.95)	0.41 ± 0.01 (0.42)	0.96 ± 0.11 (1.14)
1000	150 ± 12	0.92 ± 0.01 (0.93)	-2.92 ± 0.24 (-3.22)	0.42 ± 0.01 (0.44)	1.13 ± 0.06 (1.2)
1500	118 ± 6	0.89 ± 0.03 (0.91)	-1.93 ± 0.15 (-2.13)	0.39 ± 0.02 (0.41)	0.67 ± 0.04 (0.73)
2000	98 ± 6	0.91 ± 0.01 (0.91)	-2.35 ± 0.08 (-2.43)	0.36 ± 0.01 (0.37)	0.76 ± 0.01 (0.78)
2500	90 ± 2	0.89 ± 0.01 (0.89)	-2.81 ± 0.06 (-2.9)	0.37 ± 0 (0.37)	0.92 ± 0.03 (0.97)
3000	87 ± 3	0.88 ± 0.02 (0.89)	-3.23 ± 0.06 (-3.31)	0.37 ± 0.01 (0.38)	1.05 ± 0.02 (1.07)
3500	78 ± 1	0.88 ± 0.02 (0.91)	-3.56 ± 0.17 (-3.7)	0.37 ± 0 (0.38)	1.17 ± 0.06 (1.24)
4000	80 ± 12	0.87 ± 0.02 (0.89)	-3.76 ± 0.22 (-4.15)	0.37 ± 0 (0.38)	1.21 ± 0.06 (1.32)

Table 8: J-V data for PMI-F(DEG)-PMI series after light soaking (donor: PBDB-T, D:A 1:1, 10 mg/ml, no annealing, 4 minutes light soaking): Average values calc. from 5 best cells, respectively; shown for each spin coating speed v with average film thickness t (averaged from 3 measurements), maximum values in brackets.

v [min^{-1}]	t [nm]	V_{oc} [V]	J_{sc} [mA/cm^2]	FF [1]	PCE [%]
500	375 ± 53	0.95 ± 0.02 (0.97)	-2.57 ± 0.21 (-2.9)	0.41 ± 0 (0.41)	1.05 ± 0.1 (1.21)
1000	150 ± 12	0.93 ± 0.02 (0.95)	-3.04 ± 0.31 (-3.45)	0.44 ± 0.01 (0.45)	1.2 ± 0.11 (1.32)
1500	118 ± 6	0.73 ± 0.36 (0.89)	-2.07 ± 0.18 (-2.32)	0.35 ± 0.05 (0.4)	0.58 ± 0.3 (0.77)
2000	98 ± 6	0.91 ± 0.01 (0.91)	-2.88 ± 0.01 (-2.89)	0.37 ± 0 (0.37)	0.95 ± 0.01 (0.96)
2500	90 ± 2	0.88 ± 0.01 (0.89)	-3.3 ± 0.06 (-3.41)	0.36 ± 0.01 (0.37)	1.04 ± 0.04 (1.11)
3000	87 ± 3	0.89 ± 0.02 (0.91)	-3.48 ± 0.1 (-3.57)	0.37 ± 0 (0.37)	1.14 ± 0.05 (1.19)
3500	78 ± 1	0.71 ± 0.4 (0.91)	-2.41 ± 3.54 (-4.19)	0.5 ± 0.28 (1)	1.06 ± 0.58 (1.39)
4000	80 ± 12	0.95 ± 0.02 (0.91)	-2.57 ± 0.21 (-4.58)	0.41 ± 0 (0.38)	1.05 ± 0.1 (1.51)

Table 9: J-V data for PMI-F(DEG)-PMI series after annealing (donor: PBDB-T, D:A 1:1, 10 mg/ml, active layer spin coating with 3000 min^{-1}, annealing for 5 minutes at temperature T): Average values calc. from 5 best cells, respectively; maximum values in brackets.

T [°C]	V_{oc} [V]	J_{sc} [mA/cm^2]	FF [1]	PCE [%]
170	0.98 ± 0.04 (1.04)	-3.09 ± 0.21 (-3.43)	0.36 ± 0.01 (0.37)	1.09 ± 0.07 (1.21)
190	0.92 ± 0.03 (0.95)	-2.91 ± 0.18 (-3.1)	0.39 ± 0.03 (0.44)	1.04 ± 0.02 (1.06)
210	0.91 ± 0.01 (0.91)	-2.94 ± 0.1 (-3.07)	0.38 ± 0 (0.39)	1.02 ± 0.04 (1.07)
230	0.91 ± 0 (0.91)	-3.12 ± 0.07 (-3.19)	0.38 ± 0.01 (0.39)	1.08 ± 0.02 (1.11)
250	0.89 ± 0.02 (0.91)	-2.95 ± 0.19 (-3.27)	0.36 ± 0 (0.37)	0.96 ± 0.07 (1.07)

Table 10: J-V data for PMI-C(DEG)-PMI series (donor: PBDB-T, D:A 1:1, 10 mg/ml, no annealing, no light soaking): Average values calc. from 5 best cells, respectively; shown for each spin coating speed v with average film thickness t (averaged from 3 measurements), maximum values in brackets.

v [min^{-1}]	t [nm]	V_{oc} [V]	J_{sc} [mA/cm^2]	FF [1]	PCE [%]
500	242 ± 15	0.93 ± 0.01 (0.93)	-3.84 ± 0.19 (-4.09)	0.4 ± 0.01 (0.41)	1.43 ± 0.1 (1.54)
1000	134 ± 16	0.92 ± 0.02 (0.93)	-4.77 ± 0.22 (-5.01)	0.45 ± 0.01 (0.47)	1.95 ± 0.06 (2.03)
1500	119 ± 14	0.74 ± 0.4 (0.91)	-3.67 ± 0.78 (-4.1)	0.39 ± 0.1 (0.44)	1.27 ± 0.7 (1.62)
2000	88 ± 1	0.91 ± 0 (0.91)	-4.6 ± 0.15 (-4.79)	0.43 ± 0.01 (0.44)	1.78 ± 0.07 (1.88)
2500	89 ± 6	0.89 ± 0.01 (0.89)	-4.83 ± 0.33 (-5.2)	0.42 ± 0.01 (0.43)	1.8 ± 0.12 (1.96)
3000	109 ± 4	0.99 ± 0.01 (0.99)	-4.01 ± 0.13 (-4.22)	0.42 ± 0.01 (0.43)	1.66 ± 0.05 (1.71)
3500	87 ± 1	0.93 ± 0.02 (0.95)	-3.76 ± 0.3 (-4.05)	0.42 ± 0.01 (0.44)	1.46 ± 0.08 (1.58)
4000	95 ± 7	0.92 ± 0.01 (0.93)	-4.42 ± 0.23 (-4.65)	0.4 ± 0.01 (0.41)	1.64 ± 0.1 (1.74)

Table 11: J-V data for PMI-C(DEG)-PMI series (donor: PBDB-T, D:A 1:1, 10 mg/ml, no annealing, 4 minutes light soaking): Average values calc. from 5 best cells, respectively; shown for each spin coating speed v with average film thickness t (averaged from 3 measurements), maximum values in brackets.

v [min^{-1}]	t [nm]	V_{oc} [V]	J_{sc} [mA/cm^2]	FF [1]	PCE [%]
500	242 ± 15	0.94 ± 0.02 (0.95)	-3.95 ± 0.19 (-4.15)	0.42 ± 0.01 (0.42)	1.55 ± 0.12 (1.63)
1000	134 ± 16	0.93 ± 0.02 (0.95)	-5.17 ± 0.28 (-5.43)	0.45 ± 0.01 (0.46)	2.14 ± 0.11 (2.31)
1500	119 ± 14	0.91 ± 0.03 (0.93)	-4.91 ± 0.55 (-5.4)	0.42 ± 0.01 (0.44)	1.87 ± 0.19 (2.01)
2000	88 ± 1	0.94 ± 0.01 (0.95)	-5.85 ± 0.22 (-6.07)	0.41 ± 0.01 (0.43)	2.27 ± 0.09 (2.4)
2500	89 ± 6	0.92 ± 0.01 (0.93)	-6.37 ± 0.34 (-6.78)	0.43 ± 0.01 (0.44)	2.53 ± 0.15 (2.68)
3000	109 ± 4	0.97 ± 0.04 (1.02)	-5.32 ± 0.24 (-5.64)	0.42 ± 0 (0.43)	2.14 ± 0.03 (2.18)
3500	87 ± 1	0.94 ± 0.01 (0.95)	-5.15 ± 0.2 (-5.33)	0.42 ± 0.01 (0.43)	2.01 ± 0.07 (2.07)
4000	95 ± 7	0.95 ± 0.01 (0.95)	-5.85 ± 0.39 (-6.39)	0.42 ± 0.01 (0.43)	2.3 ± 0.14 (2.47)

Table 12: J-V data for PMI-C(DEG)-PMI series after annealing (donor: PBDB-T, D:A 1:1, 10 mg/ml, active layer spin coating with 3000 min^{-1}, annealing time 5 minutes at temperature T): Average values calc. from 5 best cells, respectively; maximum values in brackets.

T [°C]	V_{oc} [V]	J_{sc} [mA/cm^2]	FF [1]	PCE [%]
170	1.1 ± 0.01 (1.12)	-7.7 ± 0.3 (-8.2)	0.42 ± 0.01 (0.43)	3.58 ± 0.14 (3.81)
190	1.12 ± 0.01 (1.14)	-7.52 ± 0.23 (-7.79)	0.43 ± 0.01 (0.44)	3.59 ± 0.09 (3.69)
210	1.09 ± 0.01 (1.1)	-7.82 ± 0.53 (-8.65)	0.44 ± 0.01 (0.45)	3.71 ± 0.2 (3.92)
230	1.08 ± 0.02 (1.1)	-7.78 ± 0.37 (-8.3)	0.43 ± 0.03 (0.45)	3.52 ± 0.17 (3.75)
250	1.01 ± 0.02 (1.04)	-6.96 ± 0.36 (-7.41)	0.47 ± 0.01 (0.48)	3.3 ± 0.16 (3.5)

5.4.3 External Quantum Efficiency

The EQEs were determined for the best SCs (without annealing). The curves are shown in Fig.34 for solar cells with both donor:acceptor blends. The onsets are identical to those extracted from the UV/VIS spectra, respectively. Both curves show a first shoulder at $625 - 625$ nm. Comparing to the thin film UV/VIS absorption spectra of donor and acceptors (Fig.27c and 27d), this shoulder most likely origins from the donor polymer, PBDB-T. The global maximum at $500 - 520$ nm origins from the respective acceptor material. The carbazole acceptor, PMI-C(DEG)-PMI, shows higher values for EQE ($25 - 32$ % from $460 - 550$ nm) than the fluorene acceptor ($20 - 24$ % from $460 - 550$ nm).

To cross-check the accuracy of both EQE and JV measurements, J_{sc} was calculated with eq.2.5 from the recorded EQE spectra. This yields calculated J_{sc} of $3.34\,\mathrm{mA/cm^2}$ and $3.88\,\mathrm{mA/cm^2}$ for the fluorene-type and carbazole-type SC, respectively. Both values lie in the range of measured current densities ($1.9 - 3.8$ mA/cm^2 for the fluorene-type SCs, $3.6 - 4.8$ mA/cm^2 for the carbazole-type SCs), verifying the obtained experimental data. One error factor while EQE measurement is the slow degradation of the SC upon air exposure during measurement, since the encapsulation of the substrates is not completely airtight.

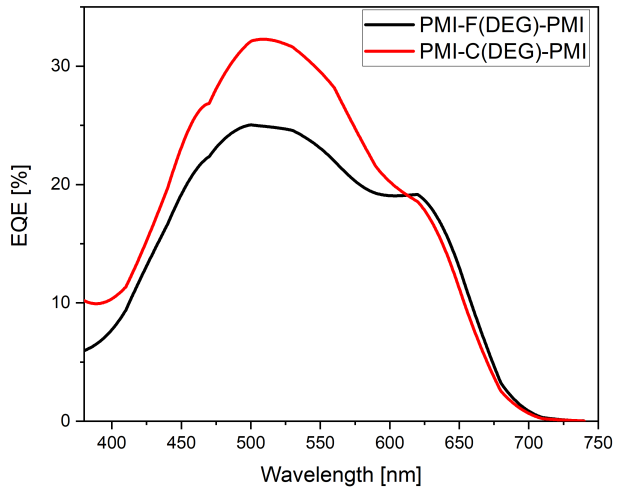

Figure 34: EQE spectra of series 1 (black) and 2 (red).

5.4.4 Thin Film Crystallinity

Crystallinity and phase mixing of donor and acceptor in the bulk heterojunction have turned out to be crucial factors determining performance and charge extraction efficiency of an OSC. A close intermixing of donor and acceptor with small microcristalline areas turned out to be ideal.[65][63] For this reason, GIWAXS measurements were conducted for the used donor:acceptor blends at RT and after annealing at 160 °C. The results are shown in Fig.35. The donor polymer PBDB-T alone (Fig.35a showed some crystalline behaviour, mainly perpendicular to the substrate. Upon annealing, crystallinity strongly increased, both parallelly and perpendicularly oriented. The acceptor PMI-F(DEG)-PMI (Fig.35d), on the other hand, did not show any crystallinity. The blends with both acceptors show the same behaviour. Only polymer signals seem to be present, both before and after annealing. All results suggest that both acceptors, PMI-F(DEG)-PMI and PMI-C(DEG)-PMI, show no crystallization in 1:1 blends. This is unfavourable for OSCs, for before mentioned reasons.

However, the produced thin films of the pure materials could have been insufficiently thick for seeing proper GIWAXS patterns. In case of PMI-C(DEG)-PMI, the measurement failed at all. So to conclude, GIWAXS measurement with ideal thin films, combined with a more thorough/detailed interpretation of the results could bring more accurate and deeper knowledge about the behaviour of the materials in blends and pure films.

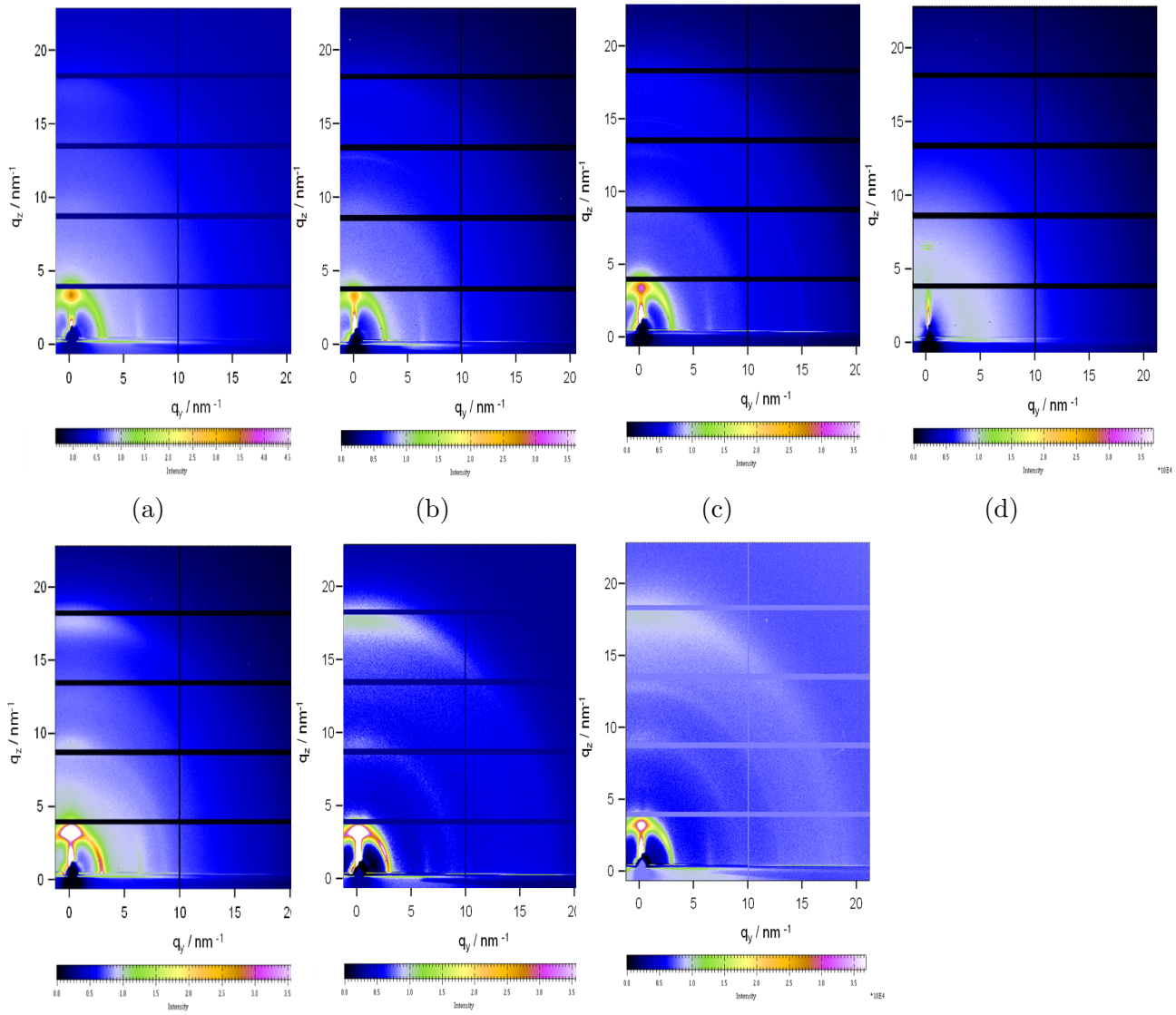

Figure 35: GIWAXS results of thin films, respectively untreated (above) and annealed at 160 °C (below) of PBDB-T (a)(e), blend PBDB-T:PMI-F(DEG)-PMI 1:1 (w:w) (b)(f), blend PBDB-T:PMI-C(DEG)-PMI 1:1 (w:w) (c)(g) and pure PMI-F(DEG)-PMI (d).

6 Summary & Outlook

The aim of this work was the introduction of polar side chains to A-D-A molecules (A = PMI, D = fluorene, carbazole). Attachment at the linker molecule should allow independent improvement of the permittivity of the compound, without changing its optical properties significantly. Objectives were, consequently, **i)** establishing synthetic procedures for new linker molecules with polar side chains, **ii)** preparation of A-D-A (A=PMI) compounds with linkers, **iii)** optical, computational and thermal characterization, **iv)** DFT analysis of geometric and optical properties, **v)** testing the new compounds in bulk heterojunction solar cells.

The side chain precursors were commercially available as primary alcohols. Therefore, the -OH groups had to be activated by installing a better leaving group. To that end, mesylation and triflation was done for the fluorinated side chains TEG_F and $Oct_F(2H)$, while DEG was converted to the corresponding bromide.

The main synthetic challenge turned out to be the alkylation of the two linker molecules, 2,7-dibromofluorene and 2,7-dibromocarbazole. Preparation of the glycolated linkers F(DEG) and C(DEG) did not pose difficulties and was achieved in good yields by following literature procedures. The fluorinated side chains, however, generally favoured side reactions. In case of both, $Oct_F(2H)$ and $Oct_F(4H)$, dehydrohalogenation was the major side reaction in any attempted reaction. This is believed to be due to a combined effect of sterically hindered, yet strongly basic nucleophiles (fluorene- and carbazole- anion) and high CH-acidity at the reaction center of the side chain. In case of carbazole, this could be proofed by isolation of the doubly eliminated $C(Oct_F(2H))$ with a C-C triple bond adjacent to the nitrogen. Still, preparation of $C(Oct_F(2H))$ could be achieved by stepwise deprotonation with NaH/KO^{t}Bu, however in low yields (4 %). Even though a product could be obtained with $Oct_F(2H)$, alkylation with TEG_F proved to be too challenging. Comparison with present literature suggested that mesylates are too weak leaving groups for fluorinated alkyl chains with only a methylene spacer. Furthermore, it is suspected, that fluorinated glycoles have a high tendency for breakdown in presence of nucleophiles.

Preparation of the acceptor unit, PMI-Bpin, proved straightforward and was done in three steps. The first intermediate, PMI-H, was obtained from perylene-3, 4, 9, 10-tetracarboxylic

dianhydride in a simultaneous decarboxylation and imide formation. PMI-H could then be brominated regiospecifically to PMI-Br with near quantitative yield, followed by Miyaura borylation reaction to give perylene monoimide pinacol boronate PMI-Bpin. The bromination was simple and required no chromatigraphic purification.

Linking to the final A-D-A compound could be successfully done via Suzuki coupling. However, many by-products and average to low yields were observed for all products. On improvement step could be the change from the classic catalyst [Pd(PPh3)4] to a more performant one, e.g. with Buchwald ligands. In summary, three acceptor molecules with A-D-A (A=PMI) structure could be prepared, PMI-F(DEG)-PMI, PMI-C(DEG)-PMI and PMI-C($\mathrm{Oct_F}$(2H))-PMI.

Both glycolated compounds, PMI-F(DEG)-PMI and PMI-C(DEG)-PMI, show strong absorption in the visible range, starting at 572 and 576 nm, respectively. Maximum absorptions are at 530 and 532 nm, respectively. The corresponding molar absorption coefficients of 92.0×10^3 and 92.2×10^3 $\mathrm{lmol^{-1}cm^{-1}}$ lie in the expected range for perylene dyes (compared with literature [90][91][92]). Furthermore, Stokes shifts of 55 and 61 nm and fluorescence quantum yields of 72 ± 5 and 64 ± 2 % could be determined, respectively for the fluorene type and carbyzole type compounds.

When building OSCs, both, PMI-F(DEG)-PMI and PMI-C(DEG)-PMI, turned out suitable for use in OSCs. Inverted architecture cells with a PBDB-T:acceptor bulk heterojunction (1:1 w:w) achieved PCEs of $0.9 - 1.2$ % and $1.4 - 2.0$ %, respectively, and moderate fill factors around $40 - 43$ %. Upon light soaking and annealing, values of the fluorene acceptor cells showed little to no change, however the carbzole acceptor cells significantly increased in performance, reaching up to 3.7 % PCE. Light soaking effects are likely to some degree caused by the zinc oxide layer (ETL), which is known to improve its conductivity upon illumination.[98]

The promising performance of DEG in solar cells would motivate their further investigation. Optimizing the SCs, e.g. by varying donor materials, D:A ratios, optimizing annealing processes etc., could potentially improve the already achieved efficiencies even further. Since many literature results emphasize the tremendous importance of an ideal donor-acceptor interplay, a closer investigation of the prepared compounds in blends, e.g. with AFM, could

bring important findings. The fluorocarbon-chain containing PMI-C(Oct_F(2H))-PMI showed promising physical properties, such as high solubility and stability. Therefore, testing their potential in solar cells and determination of their influence on the permittivity would be compelling.

To conclude, perylene based A-D-A type molecules were found to be highly tuneable and easily applicable in OSCs. If efficient synthetic pathways can be found, these materials show great promise for use in organic electronics.

7 Experimental

7.1 Instrumentation and Methods

7.1.1 Synthesis & Compound Characterization

TLC was done with silica gel 60 on aluminum sheets from Merck. Signals were detected visually under an UV lamp at 254 nm wavelength or with a stain agent. The stain agent was a $KMnO_4$ solution with 3 g $KMnO_4$, 20 g K_2CO_3, 5 ml of 5 % NaOH in 300 ml water.[100] Flash chromatography was done with silica gel 60 irregular from Fluka™.

NMR spectra were recorded on a Bruker Avance 300 MHz and a Varian Inova 500 MHz. Deuterated solvents, such as $CDCl_3$, CD_3OD and $(CD_3)_2SO$ were pruchased from Euriso-Top GmbH. All 500 MHz spectra were recorded by Dr. Petra Kaschnitz. The spectra were referenced against the TMS peak of the deuterated solvent if not otherwise stated.

Mass spectrometry HR-MS was done with the MALDI-TOF method on a Micromass MALDI micro MX from Waters. The samples were usually prepared in 4 different matrices, dithranol, dithranol-Na, *trans*-2-[3-(4-tert-butylphenyl)-2-methyl-2-propenylidene]malononitrile (DCTB) and alpha-cyano-4-hydroxycinnamic acid (alpha). The sample solutions (1 mg/ml in $CHCl_3$) were mixed with the respective matrix solution (10 mg/ml in THF) in a volumetric ratio of 2 : 7 and the solvents were let evaporate. In case of dithranol-Na, two parts of sodium trifluoroacetate were added to the solution. Sample preparations and measurements were done by Ing. Karin Bartl.

Conventional MS for lighter compounds was done with the atmospheric pressure chemical ionization (APCI) method on an Advion Expression^L CMS with nitrogen as carrier gas and the included software Advion Mass Express. The samples were applied in solution (CH_2Cl_2) onto a glass carrier and then directly inserted into the ionization chamber.

Thermoanalyis was done by thermogravimetry (TGA) and differential scanning calorimetry (DSC). TGA/DSC was done on a STA Jupiter 449C from Netzsch. The measurement was conducted in helium atmosphere with a temperature interval of $20 - 550$ °C and a scan rate of $10\,°C\,min^{-1}$. DSC was measured on a DSC 8500 from Perkin Elmer in nitrogen atmosphere with a temperature range of $30 - 380$ °C and a scan rate of $20\,°C\,min^{-1}$. The temperature run

was done twice, and the last was used for interpretation. All TGA and DSC measurements were done by Josefine Hobisch.

UV/VIS spectra were recorded on a Shimadzu UV-1800 spectrometer with 1 cm optical glass cuvettes from Hellma and $CHCl_3$ as solvent. Scanning was done from 300 to 800 nm with medium scanning speed (350 nm/min). All samples were measured 3 times with 3 different concentrations, respectively, to determine the molar absorption coefficient. Thin film absorption was measured on the same device. Therefore, 10 mg/ml solutions of the respective compound or blend in chlorobenzene were deposited onto cleaned and plasma etched glass substrates (cleaning process identical to solar cell substrate preparation, see below). Spin coating at 3000 min^{-1} with 5000 min^{-2} for 60 s, then 5000 min^{-1} with 5000 min^{-2} for 5 s.

Fluorescence spectra were measured by recording UV/VIS spectra on a Cary 50 UV-Vis spectrophotometer from Varian with optical glass cuvettes from Hellma Analytics. This was done to match the maximal absorption of the sample and the reference compound to a value of around 0.1. Subsequently, the fluorescence spectra were measured on a FluoroLog 3 spectrofluorometer from Horiba Scientific Jobi Yvon together with a R2658 photomultiplier from Hamamtsu. The spectra were recorded from $500 - 800$ nm with a slit width of 1.0 nm and excitation wavelength of 485 nm. Fluoreszenzorange from Kremer Pigmenete GmbH & Co.KG was used as reference. Mean fluorescence quantum yields were calculated with eq.5.1 (p.36) from three individual measurements.

FT-IR spectra were recorded on a Bruker ALPHA-p FT-IR spectrometer with the software OPUS 7.5.

7.1.2 Solar Cell Fabrication & Characterization

Cell fabrication was done with an ultrasonic cleaning bath from VWR and a Femto oxygen plasma etcher from diener electronics were used. Etching was done with 9.95 W and 3 min etching time. Spin coating was done on a WS-650MZ-23NPPB from Laurell Technologies Corporation inside a nitrogen glove box. Evaporation deposition was done at high vacuum ($< 10^{-5}$ mbar) with a thermal heating element to evaporate the desired substance. The heating current was adjusted manually to get a desired deposition rate. The substrates were covered with a shadow mask of 6 times 3×3 mm^2. During deposition, film thickness was

measured with an Inficon SQM-160 rate/thickness monitor.

J-V-curves were recorded inside the glove box with a Keithley 2400 source meter connected to a LabView-based software. The substrates were covered with a shadow mask with a defined illumination area of 0.070225 cm^2 per electrode. A Dedolight lDLH400 lamp with a similar emission spectrum to AM1.5G was used as light source. The distance was generally adjusted to have a light intensity of 100 mW/cm^2. Curves were recorded both under dark and illuminated conditions. The illuminated measurements were done three times with a delay of 2 minutes each, to examine light soaking effects. Scans were done from −500 to 1500 mV with 100 mA compliance, 100 measurement points, 500 mA overwrite max compliance, 100 ms delay and -0.02 V step width.

EQE measurements were done by encapsulating the solar cell in an airtight measurement box which was connected to a Stanford Research Systems SR 830 DPS lock-in amplifier and a Keithley 2400 source meter. Light source was a 75 W Xenon lamp connected to a Multimode 4-AT monochromator from Amko with 2 gratings, one for lower and one for higher wavelengths. The light was chopped at a frequency of 30 Hz. The setup was connected to a LabView-based software. The curves were generally recorded from 380 to 900 nm.

Film thicknesses were measured on a DaktakXT from Bruker, by taking mean value of $3-4$ measurements.

Optical microscopy was done on an Olympus BX60 in transmission and reflection mode. Pictures were taken with a connected camera.

GIWAXS measurements were done at the GISAXS/GIWAXS beamline at Elettra Synchrotron in Triest, Italy. As substrates, Si wafers (grade: prime, thickness: $625 \pm 20\,\mu m$) from Siegert Wafer were used to have a flat surface and less interference during the measurement. The same cleaning procedure was followed as for the solar cells (see chapter 7.4.2). Precursor solutions were prepared analogous to the ones for the solar cells (see above). The layers were produced by spin coating 20 µl of the precursor solution on to the substrate inside the nitrogen glove box. Coating parameters were 2000 min^{-1} and 500 min^{-2} for 60 s, followed by 5000 min^{-1} and 5000 min^{-2} for 5 s for drying. The final samples were then sealed in plastic bags with nitrogen before transport to the measurement facility. There, the samples were mesured in amibent atmosphere. Temperature runs were done in nitrogen atmosphere.

7.1.3 DFT Calculation

DFT calculations were done similarly for every compound. Following software was used, in the respective order:

- Chemdraw version 18.0: Drawing molecule and generating 3D structure
- Chem3D version 18.0: Generating .sdf files
- Avogadro version 1.2.0: Pre-optimizing structure, generating com-file for DFT calculation and visualization of calculation results
- FileZilla version 3.45.1: File transfer between local computer and TU DFT account
- Putty SSH client: Command console to submit calculations to Gaussian 09
- Gaussian 09, Revision D.01, Frisch M. J. *et al.*[101]: Conducting all DFT calculations
- molden 5.7: Visualization UV-VIS spectrum.

All DFT calculations were done using the B3LYP functional. 2 basis sets were used, the smaller 6-31G* set and the larger, diffused 6-31+G* set, both in gas phase and in solvent phase (chloroform). The calculation followed the general procedure:

1. Optimize geometric structure
2. Calculate vibrational frequencies as stability test for the optimized structure
3. Calculate UV/VIS absorptions, including HOMO & LUMO levels
4. Visualize the calculated orbitals

The used codes are attached in the appendix.

7.2 Chemicals

All chemicals were used as purchased unless stated otherwise. Used compounds for synthesis of the wanted products are listed in Tab.13. Dry CH_2Cl_2 was prepared by distillation over P_4O_{10}. Dry THF was prepared by running the solvent through an aluminium oxide column. The PBr3 was distilled under nitrogen atmosphere to give a colorless liquid, which was stored in the fridge (4 °C). The Oct_F(4H)-I and TEG_F-OH were dried by freeze-pump-thaw drying. They were subsequently stored over 4 Å molsieves in inert atmosphere. Fluorene, carbazole and Oct_F(2H)-OH were dried under full vacuum over $CaCl_2$ for $2-3$ days. The precursor PMI-H was prepared by Matiss Reinfelds in a 2-step reaction from perylene-3, 4, 9, 10-tetracarboxylic dianhydride, which was purchased commercially.

Table 13: Used chemicals and suppliers.

Name	Abbr.	CAS	Supplier
2-(2-Ethoxyethoxy)ethan-1-ol	DEG-OH	111-90-0	Merck
2,2-Difluoro-2-(1,1,2,2-tetrafluoro-2-(1,1,2,2-tetrafluoro-2-(trifluoromethoxy)ethoxy)ethoxy)ethan-1-ol	TEG_F-OH	147492-57-7	Fluorochem
1,1,1,2,2,3,3,4,4,5,5,6,6-Tridecafluoro-8-iodooctane	Oct_F(4H)-I	2043-57-4	Fluorochem
2,2,3,3,4,4,5,5,6,6,7,7,8,8,8-pentadecafluorooctan-1-ol	Oct_F(2H)-OH	307-30-2	abcr
2,7-Dibromofluorene	-	16433-88-8	Merck
2,7-Dibromo-9H-carbazole	-	136630-39-2	Merck
Carbazole	-	86-74-8	Alfa Aeser
Perylene-3,4,9,10-tetracarboxylic dianhydride	-	128-69-8	TCI

7.3 Synthesis

7.3.1 Side Chains

DEG-Br Bromination of the commercially available DEG-OH was done with PBr3 according to literature.[102] DEG-OH (9.65 g, 71.9 mmol) was dissolved in 40 ml CH_2Cl_2 in a round bottom flask equipped with a stir bar and septum. Then, freshly distilled PBr3 (2.70 ml, 28.7 mmol) was added dropwise over 1 hour at 0 °C. The mixture was then stirred at RT for 26 hours. Workup was done by diluting the reaction mixture with 40 ml CH_2Cl_2 and washing it

with 3 × 20 ml water. The CH_2Cl_2 was evaporated and the crude product, an opaque brown liquid, was purified by distillation with a Vigreux column and nitrogen stream at atmospheric pressure (product fraction at 140-170 °C).

Yield 6.94 g (69 %), light brown liquid, R_f 0.84 (CH:acetone 1:1), b.p. 170 °C. - ^{1}H NMR (300 MHz, $CDCl_3$, TMS) δ (ppm): 3.81 (t, $^3J_{HH}$ = 6.5 Hz, 2H), 3.72 - 3.53 (m, 2H), 3.63 - 3.42 (m, 6H), 1.22 (t, $^3J_{HH}$ = 7.0 Hz, 3H). - ^{13}C NMR (75 MHz, $CDCl_3$, TMS) δ (ppm): 71.90, 70.3, 69.6, 66.4, 30.1, 14.9. ^{1}H and ^{13}C NMR spectra compared to [102].

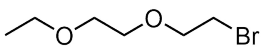

Oct_F(2H)-OTf The preparation was done in nitrogen atmosphere according to literature.[103] A Schlenk flask equipped with a stir bar was dried with a heat gun and 3 heating/vacuum cycles, then loaded with 10 ml dry CH_2Cl_2, Oct_F(2H)-OH (1.50 g, 3.74 mmol) and pyridine (0.36 ml, 4.46 mmol). Triflic anhydride was added dropwise over 40 min at 0 °C. During addition, white precipitate formed. The mixture was then stirred at RT over night. After reaction, the CH_2Cl_2 was removed under reduced pressure and the white residue was partitioned with diethyl ether (70 ml) and water (50 ml). The white precipitate dissolved in the aqueous phase. The aqueous phase was again extracted with 50 ml diethyl ether. The combined organic phased were washed with 20 ml brine, dried with Na_2SO_4 and filtered. Solvents were removed under reduced pressure.

Yield 1.50 g (75 %), colorless liquid, R_f 0.79 (CH:EA 5:1). - ^{1}H NMR (300 MHz, $CDCl_3$, TMS) δ (ppm): 4.82 (t, $^3J_{HF}$ = 12.2 Hz, 2H). - ^{13}C NMR (75 MHz, $CDCl_3$, TMS) δ (ppm): 68.1 (t, $^2J_{CF}$ = 28 Hz).

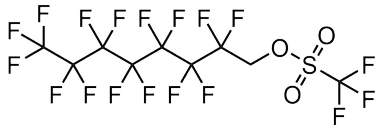

TEG_F-OMs The synthesis was done in nitrogen atmosphere according to literature.[104] A Schlenk flask equipped with a stir bar was dried with a heat gun and 3 heating/vacuum cycles. Then TEG_F-OH (3.40 g, 8.54 mmol) and THF anh. (10 ml) were added, followed by Et_3N (1.28 ml, 9.38 mmol). The methanesulfonyl chloride (0.70 ml, 9.04 mmol) was added

dropwise over 15 min at 0 °C. The mixture was stirred at 0 °C for 1 h, then over night at RT. White precipitate formed. After reaction, the mixture was diluted with 30 ml diethyl ether and washed with 2 × 10 ml water and 10 ml brine, followed by drying with Na_2SO_4, filtration and evaporation of the solvent (300 mbar, 50 °C).

Yield 3.20 g (80 %); light brown liquid, R_f 0.76 (CH:CH_2Cl_2 1:3). ^{1}H NMR (300 MHz, $CDCl_3$, TMS) δ (ppm): 4.54 (t, $^3J_{HF}$ = 8.8 Hz, 2H), 2.98 (s, 3H). - ^{13}C NMR (75 MHz, $CDCl_3$, TMS) δ (ppm): 124.4, 124.1, 120.8, 120.4, 117.3, 116.7, 65.1 (t, $^2J_{CF}$ = 35 Hz), 38.0.

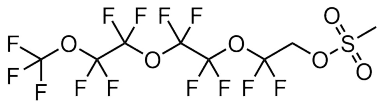

7.3.2 Linkers

F(DEG) The synthesis was done in a biphase system according to literature.[71] 2,7-dibromofluorene (1.41 g, 4.33 mmol), tetrabutyl ammoniumbromide (TBAB, 69.0 mg, 0.21 mmol) and NaOH (15.0 g, 375 mmol) were weighed in a 3-neck round bottom flask with a stir bar, reflux condenser and nitrogen inlet. 50 ml toluene and 25 ml water were added and the flask was flushed for 5 minutes with nitrogen to remove oxygen. Then the mixture was stirred at 80° under nitrogen atmosphere for 23 hours. The organic phase turned dark red. After reaction, the mixture was diluted with 150 ml CH_2Cl_2, washed with 2 × 100 ml water and 50 ml brine. During workup, the color of the organic phase changed from dark violet to red-green. Drying over Na_2SO_4 turned the solution green. Filtration and removal of the solvent under reduced pressure gave both green and colorless crystals. The crude product was purified by flash chromatography (gradient PE:EA 8:1 - 1:1).

Yield 1.50 mg (63 %), colorless solid, R_f 0.35 (PE:EA 5:1). ^{1}H NMR (300 MHz, $CDCl_3$, TMS) δ (ppm): 7.60-7.40 (m, 6H), 3.42 (q, $^3J_{HH}$ = 6.8 Hz, 4H), 3.34 (t, $^3J_{HH}$ = 4.3 Hz, 4H), 3.20 (t, $^3J_{HH}$ = 4.3 Hz, 4H), 2.97 (t, $^3J_{HH}$ = 7.2 Hz, 4H), 2.35 (t, $^3J_{HH}$ = 7.2 Hz, 4H), 1.15 (t, $^3J_{HH}$ = 6.9 Hz, 6H). - ^{13}C NMR (75 MHz, $CDCl_3$, TMS) δ (ppm): 151.0, 138.5, 130.8, 126.8, 121.8, 121.3, 70.2, 69.8, 66.9, 66.7, 52.0, 39.6, 15.2. ^{1}H NMR spectrum compared to [71].

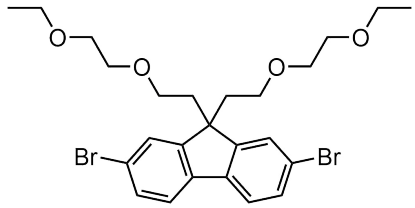

C(DEG) Synthesis was done according to literature.[72] 2,7-dibromocarbazole (1.17 g, 3.60 mmol) and crushed KOH (1.02 g, 18.1 mmol) were dissolved in 15 ml DMSO. Then the flask was flushed with nitrogen for 5 minutes and DEG-Br (1.08 g, 5.24 mmol) was added dropwise. The mixture was stirred at RT for 19 hours in nitrogen atmosphere. The mixture was extracted in 50 ml EA, washed with 2 × 25 ml water, 25 ml brine and dried over Na_2SO_4. The solution was filtered which left a white suspension in the filter paper. This was rinsed with dry THF. Evaporation of the solvent under reduced pressure yielded colorless-yellow crystals. Purification was done by flash chromatography (toluene:acetone 99:1).

Yield 1.09 mg (68 %), colorless solid, R_f = 0.20 (toluene:acetone 99:1). ^{1}H NMR (300 MHz, $(CD_3)_2SO$, TMS) δ (ppm): 8.09 (d, $^3J_{HH}$ = 8.3 Hz, 2H), 7.91 (s, 2H), 7.35 (dd, $^3J_{HH}$ = 8.2 Hz, $^4J_{HH}$ = 1.3 Hz, 2H), 4.56 (t, $^3J_{HH}$ = 4.2 Hz, 2H), 3.76 (t, $^3J_{HH}$ = 4.2 Hz, 2H), 3.41 (t, $^3J_{HH}$ = 4.0 Hz, 2H), 3.30 (t, $^3J_{HH}$ = 4.0 Hz, 2H), 3.24 (q, $^3J_{HH}$ = 7.0 Hz, 2H), 0.96 (t, $^3J_{HH}$ = 6.9 Hz, 3H). - ^{13}C NMR (75 MHz, $(CD_3)_2SO$, TMS) δ (ppm): 141.5, 122.1, 121.9, 120.7, 119.0, 113.0, 70.2, 69.2, 69.1, 65.6, 43.0, 15.0.

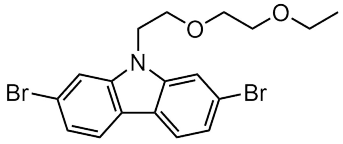

C($\mathbf{Oct_F}$(2H)) Synthesis was done in nitrogen atmosphere similar to literature.[105] A 20 ml Schlenk flask with stir bar was dried with a heat gun and 3 heating/vacuum cycles. It was then charged with 2,7-dibromocarbazole (480 mg, 1.42 mmol) and sodium *tert*-butoxide (145 mg, 1.29 mmol). The flask was subjected to 3 vacuum cycles to remove residual water. 5 ml THF anh. were added and the solution was stirred at RT over night. The solution turned dark red. Subsequently, the THF was removed under reduced pressure and 10 ml DMF anh. were added. The TEG_F-OTf (2.20 g, 4.14 mmol) was added dropwise over 1 hour at 0 °C.

The solution was then stirred for 1 hour at 0 °C and for 4 hours at RT. Due to unfinished reaction (TLC control), the mixture was heated to 60 °C for 48 hours and subsequently 110 °C for 2 hours. Workup by diluting with 40 ml EA, washing with 3×20 ml water, then 20 ml brine, drying over Na_2SO_4, filtration and evaporation of the solvents under reduced pressure. This gives a red solid. The residue was extracted with 10 ml CH. The extract was purified by flash chromatography (2x) (gradient CH:EA 98:2 - 90:10), but without full separation. Recrystallization of the cleanest fraction from hot CH yielded colorless needle-shaped crystals as pure product.

Yield 44.0 mg (4.4 %), colorless needle-shaped solid, $R_f = 0.75$ (CH:EA 10:1). ^{1}H NMR (300 MHz, $CDCl_3$, TMS) δ (ppm): 7.89 (d, $^3J_{HH} = 8.3$ Hz, 2H), 7.52 (s, 2H), 7.43 (dd, $^3J_{HH} = 8.4$ Hz, $^4J_{HH} = 1.2$ Hz, 2H), 4.80 (t, $^3J_{HF} = 15.8$ Hz, 2H).

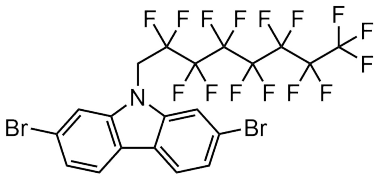

7.3.3 PMI Precursors

PMI-Br Synthesis was done according to literature.[106] PMI (6.00 g, 12.5 mmol) was suspended in 255 ml glacial acetic acid (99.8 %) in a 500 ml round bottom flask and a heavy stir bar. After 30 minutes stirring, I_2 (125 mg, 0.50 mmol) was added. Then, Br_2 was added over 15 minutes (2×1 ml & 1×0.5 ml, 50.0 mmol) with a graduated pipette. Stirring at RT for 24 hours. When TLC indicated reaction completion, the excess Br_2 was removed by blowing air through the solution for 1 hour. 150 ml MeOH was added and after 30 minutes the mixture was poured on 1 l water. The product was isolated by filtration and washing the residue with water until the filtrate had a pH value of ~ 6 (controlled with indicator paper). The residue was dried over KOH pellets and $CaCl_2$.

Yield 6.61 g (94 %), dark red solid, $R_f = 0.60$ (toluene:acetone 99:1, eluated 5x). - ^{1}H NMR (300 MHz, $CDCl_3$, TMS) δ (ppm): 8.71 - 8.59 (m, 2H), 8.51 - 8.42 (m, 2H), 8.40 (d, $^3J_{HH} = 8.1$ Hz, 1H), 8.30 (d, $^3J_{HH} = 8.2$ Hz, 1H), 8.22 (d, $^3J_{HH} = 8.2$ Hz, 1H), 7.90 (d, $^3J_{HH} = 8.2$ Hz, 1H), 7.71 (t, $^3J_{HH} = 8.1$ Hz, 1H), 7.49 (t, $^3J_{HH} = 7.6$ Hz, 1H), 7.34 (d, $^3J_{HH} = 7.7$

Hz, 2H), 2.77 (sept, $^3J_{HH}$ = 6.7 Hz, 2H), 1.19 (d, $^3J_{HH}$ = 6.8 Hz, 12H). - FT-IR $\tilde{v}$ (cm^{-1}): 1697, 1653 (OCNCO imide). ^{1}H NMR spectrum compared to [107].

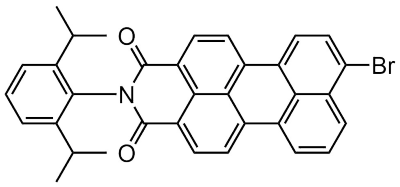

PMI-Bpin Synthesis was done according to literature.[108] The reaction was done under exclusion of air and water in nitrogen atmosphere. All reactants were dried beforehand, since prior attempts revealed a high sensitivity to water. A 3-neck round bottom flask equipped with a reflux condenser and nitrogen inlet was dried by heating it 3 times at full vacuum. Then, PMI-Br (1.21 g, 2.16 mmol), bis(pinacolato)diboron (724 mg, 2.79 mmol), KOAc (850 mg, 7.58 mmol) and the catalyst [1,1´-bis(diphenylphosphino)ferrocene]dichloropalladium(II) [Pd(dppf)Cl_2] (328 mg, 0.45 mmmol) were weighed into the flask inside the nitrogen glovebox. In the fume hood, 50 ml dioxane anh. were added and the mixture was stirred at 80 °C for 24 hours. Reaction progress was monitored by TLC. For workup, the reaction mixture was diluted with 200 ml CH_2Cl_2 and washed with 3 × 50 ml water, brine and dried over Na_2SO_4. Purification was done by flash chromatography (gradient CH_2Cl_2:CH 5:1 - pure CH_2Cl_2).

Yield 800 mg (59 %), red solid, R_f = 0.85 (CH_2Cl_2). - ^{1}H NMR (300 MHz, $CDCl_3$, TMS) δ (ppm): 8.85 (d, $^3J_{HH}$ = 8.4 Hz, 1H), 8.63 (t, $^3J_{HH}$ = 7.0 Hz, 2H), 8.50-8.31 (m, 4H), 8.19 (d, $^3J_{HH}$ = 7.4 Hz, 1H), 7.64 (dd, $^3J_{HH}$ = 7.8 Hz, 1H), 7.48 (dd, $^3J_{HH}$ = 7.6 Hz, 1H), 7.35 (d, $^3J_{HH}$ = 7.6 Hz, 2H), 2.78 (dq, $^3J_{HH}$ = 6.7 Hz, 2H), 1.47 (s, 12H), 1.19 (d, $^3J_{HH}$ = 6.6 Hz, 12H). - ^{13}C NMR (75 MHz, $CDCl_3$, TMS) δ (ppm): 164.2, 164.1, 145.9, 138.2, 138.0, 137.5, 137.4, 136.4, 132.2, 132.0, 131.9, 131.8, 131.2, 130.5, 129.6, 129.1, 127.9, 127.3, 127.0, 125.1, 124.1, 123.8, 122.9, 121.5, 120.9, 120.4, 84.4, 29.3, 25.1, 24.2.- HR-MS (MALDI-TOF) calcd. $C_{40}H_{39}NO_4B^+$ $[MH]^+$: 608.2979; found 608.4222. - FT-IR $\tilde{v}$ (cm^{-1}): 1699, 1661 (OCNCO imide). ^{1}H and ^{13}H NMR spectra compared to [109].

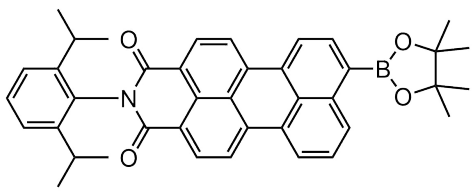

7.3.4 A-D-A Molecules

Suzuki coupling general procedure The general procedure followed literature.[110],[107] PMI-boronic ester (1.2 eq) and the respective linker (1.0 eq) were weighed into a 3-neck round bottom flask equipped with a stir bar, reflux condenser and nitrogen inlet connected to a Schlenk line. Toluene was added and the system was flushed for 5 minutes with nitrogen to remove oxygen. An inorganic base, either 1 M K_2CO_3 or 1 M KF solution (11 eq, respectively), was added. in case of K_2CO_3, a phase transfer catalyst, either Aliquat 336 (1-2 drops) or TBAB (1 spatula tip), was added. In case of KF, EtOH ($0.1V_{KF}$) was added. Then the catalyst [$Pd(PPh_3)_4$] (0.1 eq) was added. The system was again flushed with nitrogen and then refluxed at 110 °C for several hours. When TLC indicated reaction completion, the mix was worked up by diluting with CH_2Cl_2 and washing twice with water, once with brine, drying over Na_2SO_4, filtration and removing the solvents under reduced pressure. Purification was done by flash chromatography and recrystallization.

PMI-F(DEG)-PMI Synthesis was done by following the general Suzuki procedure. Used amounts: PMI-Bpin 340 mg (0.62 mmol), F(DEG) 154 mg (0.250 mmol), 1 M K_2CO_3 2.80 ml (2.80 mmol), TBAB 1 spatula tip, [$Pd(PPh_3)_4$] 40.0 mg (0.0350 mmol), 35 ml toluene. Reflux for 5 hours. Red-black crude product. For purification, dry column vacuum chromatography was run twice to remove high R_f impurities (eluent CH_2Cl_2 until eluent was colorless, then acetone to get product) and low R_f impurities (eluent CH_2Cl_2:acetone 10:1), respectively. The clean fraction was then recrystallized from a minimal volume CH_2Cl_2 which was overlayered with twice the amount methanol (2 days in fridge).

Yield 180 mg (51 %), dark red solid, $R_f = 0.20$ (CH_2Cl_2:acetone 40:1), 0.05 (CH_2Cl_2:acetone 99:1), T_g = 222 °C, m.p. = 345 °C. - ^{1}H NMR (500 MHz, $CDCl_3$, TMS) δ (ppm): 8.70 (d, $^3J_{HH}$ = 4.6 Hz, 2H), 8.68 (d, $^3J_{HH}$ = 4.6 Hz, 2H), 8.60 - 8.46 (m, 8H), 8.11 (d, $^3J_{HH}$ = 8.4 Hz, 2H), 7.97 (d, $^3J_{HH}$ = 7.7 Hz, 2H), 7.72 (d, $^3J_{HH}$ = 7.7 Hz, 2H), 7.69 - 7.58 (m, 6H), 7.49 (t, $^3J_{HH}$ = 7.7 Hz, 2H), 7.36 (d, $^3J_{HH}$ = 7.8 Hz, 4H), 3.45 - 3.38 (m, 8H), 3.38 - 3.32 (m, 4H), 3.11 (t, $^3J_{HH}$ = 7.1 Hz, 4H), 2.80 (sept, $^3J_{HH}$ = 6.8 Hz, 4H), 2.54 (t, $^3J_{HH}$ = 6.9 Hz, 4H), 1.20 (d, $^3J_{HH}$ = 6.7 Hz, 24H), 1.12 (t, $^3J_{HH}$ = 7.0 Hz, 6H). - ^{13}C NMR (125 MHz, $CDCl_3$, TMS) δ (ppm): 164.0, 150.0, 145.8, 143.5, 139.9, 139.3, 137.7, 137.6, 132.8, 132.1, 132.1, 131.1,

130.6, 129.64, 129.53, 129.47, 129.32, 128.66, 128.53, 128.46, 128.24, 127.2, 127.0, 125.0, 124.0, 123.6, 121.04, 120.94, 120.40, 120.24, 120.17, 70.2, 69.8, 67.5, 66.6, 51.8, 39.6, 29.2, 24.1, 15.1. - HR-MS (MALDI-TOF) calcd. $C_{93}H_{84}N_2O_8{}^+$ $[M]^+$ m/z: 1356.6228; found 1356.6490. - UV/VIS ($CHCl_3$) $\lambda_{max}(\alpha)$: 530 nm (91 979 $lmol^{-1}cm^{-1}$), 507 nm (83 175 $lmol^{-1}cm^{-1}$). - Fluorescence ($CHCl_3$, excit. 485 nm) $\lambda_{max}(I_{rel})$: 585 nm (1). - FT-IR $\tilde{v}$ (cm^{-1}): 1701, 1661 (OCNCO imide).

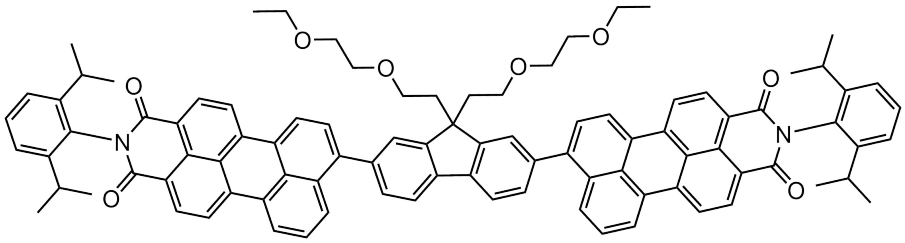

PMI-C(DEG)-PMI Synthesis was done by following the general Suzuki procedure. Used amounts: PMI-Bpin 960 mg (2.18 mmol), C(DEG) 550 mg (0.905 mmol), 1 M K_2CO_3 10.0 ml (10.0 mmol), Aliquat 336 2 drops, $[Pd(PPh_3)_4]$ 100 mg (0.080 mmol), toluene 30 ml. Reflux for 17 hours. Red-black crude product (1.30 g). The crude product was purified by flash chromatography (gradient CH_2Cl_2:acetone 50:1 - 30:1). With the cleanest fractions, a second chromatography was done (gradient CH_2Cl_2:acetone 60:1 - 20:1). 3 fractions (total 524 mg) were collected and further recrystallized separately 2-3 times from hot toluene, respectively. The purest fractions were combined.

Yield 134 mg (12 %), red-violet solid, $R_f = 0.48$ (CH_2Cl_2:acetone 60:1), $T_g = 276\,°C$, m.p. = 285 °C. - ^1H NMR (500 MHz, $CDCl_3$, TMS) δ (ppm): 8.72 - 8.62 (m, 4H), 8.53 (d, $^3J_{HH}$ = 7.8 Hz, 2H), 8.51 - 8.40 (m, 6H), 8.33 (d, $^3J_{HH}$ = 7.8 Hz, 2H), 8.16 (d, $^3J_{HH}$ = 8.4 Hz, 2H), 7.80 - 7.70 (m, 4H), 7.62 (t, $^3J_{HH}$ = 7.8 Hz, 2H), 7.55 - 7.45 (m, 4H), 7.36 (d, $^3J_{HH}$ = 7.8 Hz, 4H), 4.65 (t, $^3J_{HH}$ = 5.1 Hz, 2H), 3.96 (t, $^3J_{HH}$ = 5.6 Hz, 2H), 3.55 (t, $^3J_{HH}$ = 4.5 Hz, 2H), 3.43 (t, $^3J_{HH}$ = 4.5 Hz, 2H), 3.28 (q, $^3J_{HH}$ = 7.0 Hz, 2H), 2.81 (sept, $^3J_{HH}$ = 6.8 Hz, 4H), 1.21 (d, $^3J_{HH}$ = 6.7 Hz, 24H), 0.97 (t, $^3J_{HH}$ = 7.0 Hz, 3H). - ^{13}C NMR (125 MHz, $CDCl_3$, TMS) δ (ppm): 164.0, 145.8, 144.3, 141.5, 137.9, 137.8, 137.7, 133.0, 132.1, 132.1, 131.1, 130.6, 129.8, 129.5, 129.4, 128.7, 128.5, 128.5, 127.1, 127.0, 124.0, 124.0, 123.5, 122.4, 121.9, 121.0, 120.9, 120.4, 120.3, 120.1, 110.8, 71.1, 69.9, 69.6, 66.7, 43.6, 29.2, 24.1, 15.0. - HR-MS

(MALDI-TOF) calcd. $C_{86}H_{72}N_3O_6^+$ $[MH]^+$ *m/z*: 1242.5421; found 1242.5321. - UV/VIS ($CHCl_3$) $\lambda_{max}(\alpha)$: 532 nm (92 261 $lmol^{-1}cm^{-1}$), 507 nm (81 502 $lmol^{-1}cm^{-1}$). - Fluorescence ($CHCl_3$, excit. 485 nm) $\lambda_{max}(I_{rel})$: 593 (1).

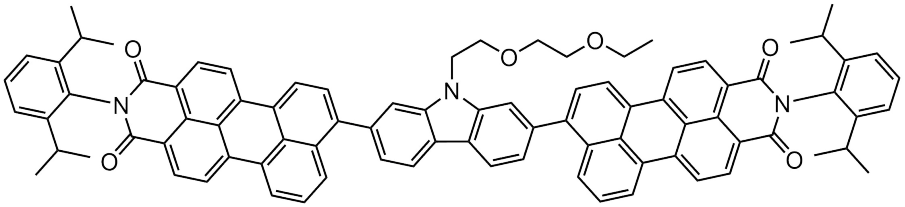

PMI-C(Oct$_F$(2H))-PMI Synthesis was done by following the general Suzuki procedure. Used amounts: PMI-Bpin 220 mg (0.310 mmol), C(Oct$_F$(2H)) 44.0 mg (0.0730 mmol), 1 M KF 0.800 ml (0.800 mmol), EtOH 0.1 ml, $[Pd(PPh_3)_4]$ 15.0 mg (0.0130 mmol), toluene 10 ml. Reflux for 17 hours. Red-black crude product. The crude product was purified by flash chromatography (eluent CH_2Cl_2) and subsequent recrystallization of the purest fraction from CH_2Cl_2 and MeOH as antisolvent (3x volume) and cooling over night. The wanted product formed as violet precipitate. Product still contained impurities, but due to the small amount, no further purification was conducted.

Yield $\sim$ 5 mg (4 %), red-violet solid (contains impurities (NMR)), R_f = 0.55 (CH_2Cl_2, eluated 3x). - ^{1}H NMR (500 MHz, $CDCl_3$, TMS) δ (ppm): 8.74-8.69 (m, 4H), 8.62 (d, $^3J_{HH}$ = 8.0 Hz, 2H), 8.60-8.52 (m, 6H), 8.35 (d, $^3J_{HH}$ = 8.0 Hz, 2H), 8.13 (d, $^3J_{HH}$ = 8.5 Hz, 2H), 7.78 (d, $^3J_{HH}$ = 7.7 Hz, 2H), 7.68-7.62 (m, 4H), 7.59 (d, $^3J_{HH}$ = 7.8 Hz, 2H), 7.49 (t, $^3J_{HH}$ = 7.8 Hz, 2H), 7.36 (d, $^3J_{HH}$ = 7.8 Hz, 4H), 5.04 (t, $^3J_{HF}$ = 15.7 Hz, 2H), 2.79 (sept, $^3J_{HH}$ = 6.8 Hz, 4H), 1.20 (d, $^3J_{HH}$ = 6.8 Hz, 24H) (due to impurities and small sample mass, integral values are not exact (vary $\pm$5 %)). - HR-MS (MALDI-TOF) calcd. $C_{88}H_{60}F_{15}N_3O_4^+$ $[MH]^+$ *m/z*: 1508.4423; found 1508.4519.

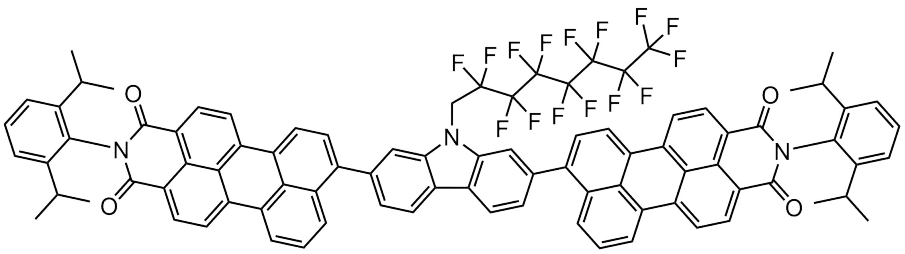

7.4 Solar Cells

7.4.1 Device Architecture

All solar cells were built in an inverted structure with the sequence substrate-cathode-ETL-AL-HTL-cathode. As active layer, bulk heterojunctions of electron donor polymer and electron acceptor dye were prepared. PBDB-T was used as donor polymer and mixed with the respective acceptor. Cathode was the built in ITO film of the substrates. As anode material Ag was used. As ETL, ZnO nanoparticles and as HTL, MoO_3 was used. Following cells were prepared:

- glass / ITO / ZnO / PBDB-T:PMI-F(DEG)-PMI (1:1) / MoO_3 / Ag
- glass / ITO / ZnO / PBDB-T:PMI-C(DEG)-PMI (1:1) / MoO_3 / Ag

7.4.2 Substrate Preparation

For the photovoltaic cells, patterned glass/ITO substrates ($15 \times 15 \times 1.1$ mm, $15\,\Omega sq^{-1}$) from Luminescence Technology Corp were used. The substrates were prepared by cutting the Si wafers in 2.5×2.5 cm^2 squares with a diamond blade. All substrates were first pre-cleaned with acetone and Kimwipes, then put in an isopropanol bath and placed in an utrasonic bath at 40 °C for 40 minutes. After drying the substrates in a nitrogen stream, they were etched with oxygen plasma for 3 minutes just before the first layer deposition. This is done to remove remaining organic contaminations and increase hydrophilicity to improve wetting properties of the surface.

7.4.3 Electron Transport Layer

As electron transport layer, ZnO was applied using a sol-gel procedure identical to literature.[111]. The precursor solution was prepared by mixing 500 mg zinc acetate dihydrate with 150 µl ethanolamine and 5 ml 2-methoxyethanol and stirring it for a day (prepared by Dipl.Ing. Stefan Weber). The solution was then stored inside the glove box under constant stirring. The film was produced by spin-coating 30 ul of the solution onto the plasma-etched substrates with 2000 min^{-1} and 500 min^{-2} for 30 s. Subsequently, the substrates were annealed at 150 °C for 15 min outside the glove box. This should produce ZnO films of $30 - 40$ nm thickness.

7.4.4 Active Layer

For the active layer, the precursor solutions were prepared the day before to achieve full dissolution of the donor polymer and to obtain a homogeneous donor-acceptor blend. Respective amounts of donor and acceptor material were weighed in seperately into small vials. Then both vials were transferred into the glove box. First, solvent was added to the acceptor to obtain a 10 mg/ml solution. After full dissolution, the acceptor solution was transferred into the donor vial. The mixture was then stirred at 40 °C for at least 8 hours, usually over night to obtain a homogeneous solution. During spin coating, the precursor was stored on a heating plate at 60 °C to prevent crystallization of particles.
The spin coating consisted of 2 cycles:

- Cycle 1: x min^{-1} with 500 min^{-2} for 60 s
- Cycle 2: 5000 min^{-1} with 5000 min^{-2} for 5 s, to evaporate remaining solvent

The rotation speed in cycle 1 was varied from 500 to 4000 min^{-1} to investigate the influence of different layer thicknesses on the device performance. For then annealing series, the beforehand determined ideal film thickness was chosen (3000 min^{-1} for both acceptors).

7.4.5 Hole Transport Layer and Electrode

The HTL consisting of MoO3 as well as the anode were deposited by evaporation deposition. Therefore, the substrates were put into shadow masks in a rotating sample holder. The evaporation chamber was evacuated to a pressure of $\sim 10^{-5}$ mbar. The HTL was deposited first, followed by the anode. The thicknesses and deposition rates were, respectively:

- MoO3: thickness 10 nm, 0.1 - 0.5 $\text{Å}\,\text{s}^{-1}$
- Ag: thickness 100 nm, 0.3 - 0.5 $\text{Å}\,\text{s}^{-1}$ for the first 10 nm, then 1.0 - 1.5 $\text{Å}\,\text{s}^{-1}$

References

(1) Williams, R. *The Journal of Chemical Physics* **1960**, *32*, 1505–1514.

(2) Nokia Bell-Labs Timeline. `https://www.bell-labs.com/timeline/#/1950/1/open/` (accessed 12/14/2019).

(3) O'Regan, B.; Grätzel, M. *Nature* **1991**, *353*, 737–740.

(4) *Polymer photovoltaics: a practical approach*; Krebs, F. C., Ed., OCLC: ocn183610455; SPIE Press: Bellingham, Wash, 2008, 315 pp.

(5) Stephen, M.; Genevičius, K.; Juška, G.; Arlauskas, K.; Hiorns, R. C. *Polymer International* **2017**, *66*, 13–25.

(6) Cui, Y.; Yao, H.; Zhang, J.; Zhang, T.; Wang, Y.; Hong, L.; Xian, K.; Xu, B.; Zhang, S.; Peng, J.; Wei, Z.; Gao, F.; Hou, J. *Nat Commun* **2019**, *10*, 2515.

(7) Søndergaard, R.; Hösel, M.; Angmo, D.; Larsen-Olsen, T. T.; Krebs, F. C. *Materials Today* **2012**, *15*, 36–49.

(8) Best Research-Cell Efficiency Chart — Photovoltaic Research — NREL. `https://www.nrel.gov/pv/cell-efficiency.html` (accessed 01/21/2020).

(9) Knupfer, M. *Applied Physics A* **2003**, *77*, 623–626.

(10) Davydov, A., *Theory of Molecular Excitons*; Springer US: 1971.

(11) Brebels, J.; Manca, J. V.; Lutsen, L.; Vanderzande, D.; Maes, W. *J. Mater. Chem. A* **2017**, *5*, 24037–24050.

(12) Hiramoto, M.; Fujiwara, H.; Yokoyama, M. *Applied Physics Letters* **1991**, *58*, 1062–1064.

(13) Koster, L. J. A.; Shaheen, S. E.; Hummelen, J. C. *Advanced Energy Materials* **2012**, *2*, 1246–1253.

(14) Wannier, G. H. *Phys. Rev.* **1937**, *52*, 191–197.

(15) Langevin, P. *Ann. Chim. Phys.* **1903**, *28*, 433.

(16) Kirchartz, T.; Pieters, B. E.; Kirkpatrick, J.; Rau, U.; Nelson, J. *Phys. Rev. B* **2011**, *83*, 115209.

(17) Yu, G.; Gao, J.; Hummelen, J. C.; Wudl, F.; Heeger, A. J. *Science* **1995**, *270*, 1789–1791.

(18) Dang, M. T.; Hirsch, L.; Wantz, G. *Adv. Mater.* **2011**, *23*, 3597–3602.

(19) Chen, W.; Zhang, Q. *Journal of Materials Chemistry C* **2017**, *5*, 1275–1302.

(20) Chang, C.-Y.; Wu, C.-E.; Chen, S.-Y.; Cui, C.; Cheng, Y.-J.; Hsu, C.-S.; Wang, Y.-L.; Li, Y. *Angew. Chem. Int. Ed.* **2011**, *50*, 9386–9390.

(21) Yan, J.; Saunders, B. R. *RSC Adv.* **2014**, *4*, 43286–43314.

(22) Ganesamoorthy, R.; Sathiyan, G.; Sakthivel, P. *Solar Energy Materials and Solar Cells* **2017**, *161*, 102–148.

(23) Patil, Y.; Misra, R. *The Chemical Record* **2018**, *18*, 1350–1364.

(24) Meng, D.; Sun, D.; Zhong, C.; Liu, T.; Fan, B.; Huo, L.; Li, Y.; Jiang, W.; Choi, H.; Kim, T.; Kim, J. Y.; Sun, Y.; Wang, Z.; Heeger, A. J. *Journal of the American Chemical Society* **2016**, *138*, 375–380.

(25) Mayer, A. C.; Scully, S. R.; Hardin, B. E.; Rowell, M. W.; McGehee, M. D. *Materials Today* **2007**, *10*, 28–33.

(26) Choy, W. C. H., *Organic Solar Cells*; Springer: London, 2013.

(27) Benanti, T. L.; Venkataraman, D. *Photosynthesis Research* **2006**, *87*, 73–81.

(28) Hoffmann, O. T.; Zojer, E. Organic Semiconductors (PHT.302UF)., Lecture, Lecture, Graz, University of Technology: Institute of Solid State Physics, 2019.

(29) Petritsch, K. Organic Solar Cell Architectures, PhD Thesis., Ph.D. Thesis, Cambridge and Graz, 2000, 159 pp.

(30) Scharber, M. C.; Mühlbacher, D.; Koppe, M.; Denk, P.; Waldauf, C.; Heeger, A. J.; Brabec, C. J. *Advanced Materials* **2006**, *18*, 789–794.

(31) Tress, W., *Organic Solar Cells*; Springer Series in Materials Science, Vol. 208; Springer International Publishing: Cham, 2014.

(32) Qi, B.; Wang, J. *Phys. Chem. Chem. Phys.* **2013**, *15*, 8972.

(33) Shockley, W.; Queisser, H. J. *J. Appl. Phys.* **1961**, 510–519.

(34) Ameri, T.; Dennler, G.; Lungenschmied, C.; Brabec, C. J. *Energy & Environmental Science* **2009**, *2*, 347.

(35) Qin, R.; Guo, D.; Li, M.; Li, G.; Bo, Z.; Wu, J. *ACS Appl. Energy Mater.* **2019**, *2*, 305–311.

(36) Zhan, C.; Zhang, X.; Yao, J. *RSC Advances* **2015**, *5*, 93002–93026.

(37) Khatri, I.; Bao, J.; Kishi, N.; Soga, T. *ISRN Electronics* **2012**, *2012*, 1–10.

(38) Wang, J.-C.; Weng, W.-T.; Tsai, M.-Y.; Lee, M.-K.; Horng, S.-F.; Perng, T.-P.; Kei, C.-C.; Yu, C.-C.; Meng, H.-F. *J. Mater. Chem.* **2010**, *20*, 862–866.

(39) Liao, K.-S.; Yambem, S. D.; Haldar, A.; Alley, N. J.; Curran, S. A. *Energies* **2010**, *3*, 1212–1250.

(40) Moulé, A. J.; Meerholz, K. *Advanced Functional Materials* **2009**, *19*, 3028–3036.

(41) Wang, H.-J.; Chen, C.-P.; Jeng, R.-J. *Materials* **2014**, *7*, 2411–2439.

(42) Li, G.; Zhu, R.; Yang, Y. *Nature Photon* **2012**, *6*, 153–161.

(43) Bian, L.; Zhu, E.; Tang, J.; Tang, W.; Zhang, F. *Progress in Polymer Science* **2012**, *37*, 1292–1331.

(44) Xu, Y.; Yao, H.; Hou, J. *Chinese Journal of Chemistry* **2019**, *37*, 207–215.

(45) He, Y.; Chen, H.-Y.; Hou, J.; Li, Y. *Journal of the American Chemical Society* **2010**, *132*, 1377–1382.

(46) Anctil, A.; Babbitt, C. W.; Raffaelle, R. P.; Landi, B. J. *Environ. Sci. Technol.* **2011**, *45*, 2353–2359.

(47) Yan, C.; Barlow, S.; Wang, Z.; Yan, H.; Jen, A. K.-Y.; Marder, S. R.; Zhan, X. *Nature Reviews Materials* **2018**, *3*, DOI: 10.1038/natrevmats.2018.3.

(48) Koch, W.; Holthausen, M. C., *A Chemist's Guide to Density Functional Theory*, 1st ed.; Wiley: 2001.

(49) Capelle, K. *Brazilian Journal of Physics* **2006**, *36*, 1318–1343.

(50) Sham, L. J.; Schlüter, M. *Phys. Rev. Lett.* **1983**, *51*, 1888–1891.

(51) Kunz, R. W., *Molecular modelling für Anwender: Anwendung von Kraftfeld- und MO-Methoden in der organischen Chemie*, 2., überarb. u. erw. Aufl; Teubner Studienbücher Chemie, OCLC: 247135819; Teubner: Stuttgart, 1997; 287 pp.

(52) Ditchfield, R.; Hehre, W. J.; Pople, J. A. *The Journal of Chemical Physics* **1971**, *54*, 724–728.

(53) Hu, J.; Liu, X.; Wang, K.; Wu, M.; Huang, H.; Wu, D.; Xia, J. *Journal of Materials Chemistry C* **2020**, DOI: 10.1039/C9TC05713G.

(54) Aivali, S.; Tsimpouki, L.; Anastasopoulos, C.; Kallitsis, J. K. *Molecules* **2019**, *24*, 4406.

(55) Hartnett, P. E.; Timalsina, A.; Matte, H. S. S. R.; Zhou, N.; Guo, X.; Zhao, W.; Facchetti, A.; Chang, R. P. H.; Hersam, M. C.; Wasielewski, M. R.; Marks, T. J. *Journal of the American Chemical Society* **2014**, *136*, 16345–16356.

(56) Zang, Y.; Li, C.-Z.; Chueh, C.-C.; Williams, S. T.; Jiang, W.; Wang, Z.-H.; Yu, J.-S.; Jen, A. K.-Y. *Advanced Materials* **2014**, *26*, 5708–5714.

(57) Liang, N.; Sun, K.; Zheng, Z.; Yao, H.; Gao, G.; Meng, X.; Wang, Z.; Ma, W.; Hou, J. *Advanced Energy Materials* **2016**, *6*, 1600060.

(58) Zhang, Y.; Xiao, Y.; Xie, Y.; Zhu, L.; Shi, D.; Cheng, C. *Organic Electronics* **2015**, *21*, 184–191.

(59) Hu, Y.; Chen, S.; Zhang, L.; Zhang, Y.; Yuan, Z.; Zhao, X.; Chen, Y. *J. Org. Chem.* **2017**, *82*, 5926–5931.

(60) Cremer, J.; Mena-Osteritz, E.; Pschierer, N. G.; Müllen, K.; Bäuerle, P. *Org. Biomol. Chem.* **2005**, *3*, 985–995.

(61) Wen, S.; Wu, Y.; Wang, Y.; Li, Y.; Liu, L.; Jiang, H.; Liu, Z.; Yang, R. *ChemSusChem* **2018**, *11*, 360–366.

(62) Atkins, P. W.; De Paula, J., *Physical chemistry*, OCLC: 441741998; Oxford University Press: Oxford, 2006.

(63) Breselge, M.; Van Severen, I.; Lutsen, L.; Adriaensens, P.; Manca, J.; Vanderzande, D.; Cleij, T. *Thin Solid Films* **2006**, *511-512*, 328–332.

(64) Torabi, S.; Jahani, F.; Severen, I. V.; Kanimozhi, C.; Patil, S.; Havenith, R. W. A.; Chiechi, R. C.; Lutsen, L.; Vanderzande, D. J. M.; Cleij, T. J.; Hummelen, J. C.; Koster, L. J. A. *Advanced Functional Materials* **2015**, *25*, 150–157.

(65) Liu, X.; Xie, B.; Duan, C.; Wang, Z.; Fan, B.; Zhang, K.; Lin, B.; Colberts, F. J. M.; Ma, W.; Janssen, R. A. J.; Huang, F.; Cao, Y. *J. Mater. Chem. A* **2018**, *6*, 395–403.

(66) Zhang, N.; Xu, Y.; Zhou, X.; Zhang, W.; Zhou, K.; Yu, L.; Ma, W.; Xu, X. *Journal of Materials Chemistry C* **2019**, *7*, 14130–14140.

(67) Zhang, X.; Zhang, D.; Zhou, Q.; Wang, R.; Zhou, J.; Wang, J.; Zhou, H.; Zhang, Y. *Nano Energy* **2019**, *56*, 494–501.

(68) Donaghey, J. E.; Armin, A.; Burn, P. L.; Meredith, P. *Chemical Communications* **2015**, *51*, 14115–14118.

(69) Gay, J. F.; Maxson, R. N.; Kleinberg, J.; Haan, R. E. In *Inorganic Syntheses*, Fernelius, W. C., Ed.; John Wiley & Sons, Inc.: Hoboken, NJ, USA, 2007, pp 147–151.

(70) Pruckmayr, G.; Wu, T. K. *Macromolecules* **1978**, *11*, 662–668.

(71) Liu, J.; Jiang, P.; Wang, Y.; Tu, G. *Chinese Chemical Letters* **2019**, DOI: `10.1016/j.cclet.2019.05.023`.

(72) Yu, C.-Y.; Godana, A. S. *European Polymer Journal* **2018**, *99*, 165–171.

(73) Tian, X.; Cheng, X.; Yang, X.; Ren, Y.-L.; Yao, K.; Wang, H.; Wang, J. *Organic Chemistry Frontiers* **2019**, *6*, 952–958.

(74) Kanelidis, I.; Ren, Y.; Lesnyak, V.; Gasse, J.-C.; Frahm, R.; Eychmüller, A.; Holder, E. *Journal of Polymer Science Part A: Polymer Chemistry* **2011**, *49*, 392–402.

(75) Krafft, M. P. *Advanced Drug Delivery Reviews* **2001**, *47*, 209–228.

(76) Lee, J.-K.; Fong, H. H.; Zakhidov, A. A.; McCluskey, G. E.; Taylor, P. G.; Santiago-Berrios, M.; Abruña, H. D.; Holmes, A. B.; Malliaras, G. G.; Ober, C. K. *Macromolecules* **2010**, *43*, 1195–1198.

(77) Menczinger, B.; Nemes, A.; Szíjjártó, C.; Rábai, J. *Journal of Fluorine Chemistry* **2018**, *210*, 70–77.

(78) Chen, H.; Hong, F.; Shao, G.; Hang, D.; Zhao, L.; Zeng, Z. *Chemistry – An Asian Journal* **2014**, *9*, 3418–3430.

(79) Gilman, H.; Langham, W.; Jacoby, A. L. *Journal of the American Chemical Society* **1939**, *61*, 106–109.

(80) Zeng, Z.; Shreeve, J. M. *Journal of Fluorine Chemistry* **2009**, *130*, 727–732.

(81) Clayden, J.; Greeves, N.; Warren, S. G., *Organic chemistry*, 2nd ed; Oxford University Press: Oxford ; New YorK, 2012; 1234 pp.

(82) Elschenbroich, C., *Organometallchemie*, 4., überarb. und erw. Aufl; Teubner-Studienbücher Chemie, OCLC: 249071050; Teubner: Stuttgart, 2003; 756 pp.

(83) Levashov, A. S.; Buryi, D. S.; Goncharova, O. V.; Konshin, V. V.; Dotsenko, V. V.; Andreev, A. A. *New Journal of Chemistry* **2017**, *41*, 2910–2918.

(84) Coulson, D. R.; Satek, L. C.; Grim, S. O. In *Inorganic Syntheses*; John Wiley & Sons, Ltd: 2007, pp 121–124.

(85) Wiberg, E.; Wiberg, N., *Lehrbuch der anorganischen Chemie*, 102., stark umgearbeitete und verbesserte Auflage; Holleman, A. F., Fischer, G., Eds., OCLC: 180963521; Walter de Gruyter: Berlin New York, 2007; 2149 pp.

(86) Lennox, A. J. J.; Lloyd-Jones, G. C. *Israel Journal of Chemistry* **2010**, *50*, 664–674.

(87) Clausen, F.; Kischkewitz, M.; Bergander, K.; Studer, A. *Chemical Science* **2019**, *10*, 6210–6214.

(88) Achilli, C.; Ciana, A.; Fagnoni, M.; Balduini, C.; Minetti, G. *cent.eur.j.chem.* **2013**, *11*, 137–139.

(89) Wolfe, J. P.; Buchwald, S. L. *Angewandte Chemie International Edition* **1999**, *38*, 2413–2416.

(90) Zhang, X.; Jiang, B.; Zhang, X.; Tang, A.; Huang, J.; Zhan, C.; Yao, J. *J. Phys. Chem. C* **2014**, *118*, 24212–24220.

(91) Zhang, X.; Lu, Z.; Ye, L.; Zhan, C.; Hou, J.; Zhang, S.; Jiang, B.; Zhao, Y.; Huang, J.; Zhang, S.; Liu, Y.; Shi, Q.; Liu, Y.; Yao, J. *Advanced Materials* **2013**, *25*, 5791–5797.

(92) Lin, Z.; Li, C.; Meng, D.; Li, Y.; Wang, Z. *Chemistry – An Asian Journal* **2016**, *11*, 2695–2699.

(93) Fluoreszenzorange — Fluoreszenzfarbstoffe — Farbstoffe & Pflanzenfarben — Kremer Pigmente GmbH & Co. KG. `https://www.kremer-pigmente.com/de/fluoreszenzorange-94738.html` (accessed 02/03/2020).

(94) Würth, C.; Grabolle, M.; Pauli, J.; Spieles, M.; Resch-Genger, U. *Nature Protocols* **2013**, *8*, 1535–1550.

(95) Raj, M. R.; Margabandu, R.; Mangalaraja, R. V.; Anandan, S. *Soft Matter* **2017**, *13*, 9179–9191.

(96) Dai, S.; Zhao, F.; Zhang, Q.; Lau, T.-K.; Li, T.; Liu, K.; Ling, Q.; Wang, C.; Lu, X.; You, W.; Zhan, X. *J. Am. Chem. Soc.* **2017**, *139*, 1336–1343.

(97) Jao, M.-H.; Liao, H.-C.; Su, W.-F. *J. Mater. Chem. A* **2016**, *4*, 5784–5801.

(98) Jiang, Z.; Soltanian, S.; Gholamkhass, B.; Aljaafari, A.; Servati, P. *RSC Adv.* **2018**, *8*, 36542–36548.

(99) Brixi, S.; Melville, O. A.; Boileau, N. T.; Lessard, B. H. *J. Mater. Chem. C* **2018**, *6*, 11972–11979.

(100) Magic Formulas: TLC Stains. `http://chem.chem.rochester.edu/~nvd/pages/magic_formulas.php?page=tlc_stains` (accessed 11/13/2019).

(101) Frisch, M.; Trucks, G.; Schlegl, H.; et al. Gaussian 09, Revision D.01., Wallingford CT, 2016.

(102) Zhang, Y.; Chen, B.; Zhang, Y.; Qin, L.; Liu, B.; Ni, B.; Gao, G. *Green Chem.* **2018**, *20*, 1594–1601.

(103) Rábai, J.; Szabó, D.; Borbás, E. K.; Kövesi, I.; Kövesdi, I.; Csámpai, A.; Gömöry, Á.; Pashinnik, V. E.; Shermolovich, Y. G. *Journal of Fluorine Chemistry* **2002**, *114*, 199–207.

(104) O'Driscoll, L. J.; Welsh, D. J.; Bailey, S. W. D.; Visontai, D.; Frampton, H.; Bryce, M. R.; Lambert, C. J. *Chem. Eur. J.* **2015**, *21*, 3891–3894.

(105) Leijtens, T.; Ding, I.-K.; Giovenzana, T.; Bloking, J. T.; McGehee, M. D.; Sellinger, A. *ACS Nano* **2012**, *6*, 1455–1462.

(106) Nolde, F.; Pisula, W.; Müller, S.; Kohl, C.; Müllen, K. *Chem. Mater.* **2006**, *18*, 3715–3725.

(107) Cheriya, R. T.; Joy, J.; Alex, A. P.; Shaji, A.; Hariharan, M. *J. Phys. Chem. C* **2012**, *116*, 12489–12498.

(108) Gong, W.-L.; Xiong, Z.-J.; Xin, B.; Yin, H.; Duan, J.-S.; Yan, J.; Chen, T.; Hua, Q.-X.; Hu, B.; Huang, Z.-L.; Zhu, M.-Q. *J. Mater. Chem. C* **2016**, *4*, 2498–2505.

(109) Weil, T.; Abdalla, M. A.; Jatzke, C.; Hengstler, J.; Müllen, K. *Biomacromolecules* **2005**, *6*, 68–79.

(110) Avlasevich, Y.; Müllen, K. *J. Org. Chem.* **2007**, *72*, 10243–10246.

(111) Hoefler, S. F.; Haberfehlner, G.; Rath, T.; Keilbach, A.; Hobisch, M. A.; Dixon, A.; Pavlica, E.; Bratina, G.; Kothleitner, G.; Hofer, F.; Trimmel, G. *ACS Appl. Energy Mater.* **2019**, *2*, 7535–7545.

Appendix

DFT calculation

Geometric optimization	Vibrational calculation	Optical calculation
%nproc=8 %Chk=filename.chk #p B3LYP/6-31G(d,p) Opt comment 01 atom matrix	%nproc=8 %Chk=filename-geometric-optimization.chk #p B3LYP/6-31G(d,p) Freq geom=checkpoint guess=read comment 01	%nproc=8 %oldchk=filename-vibrational-calculation.chk %chk=filename˙new.chk #P Geom=Checkpoint td=(nstates=10, singlets) b3lyp 6-31G* Pop=Full SCF=(maxcyc=800) comment 01

NMR Spectroscopy

Side Chains

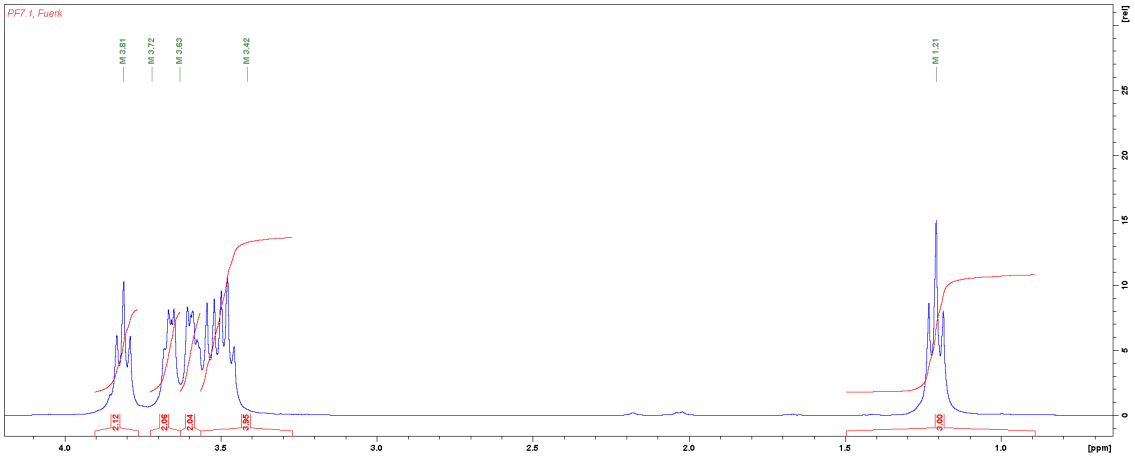

Figure 36: ^{1}H NMR spectrum (300 MHz, $CDCl_3$, TMS) of DEG-Br

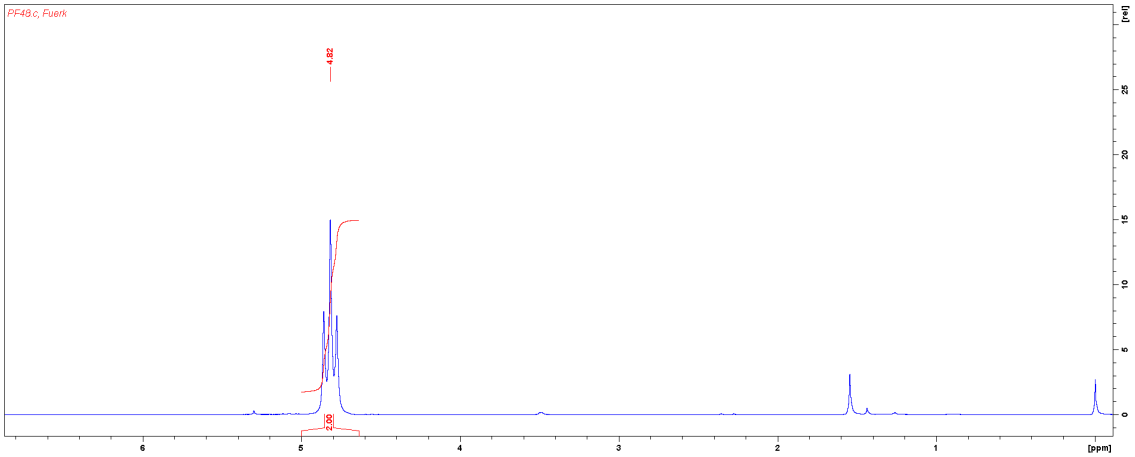

Figure 37: ^{1}H NMR spectrum (300 MHz, $CDCl_3$, TMS) of Oct_F(2H)-OTf

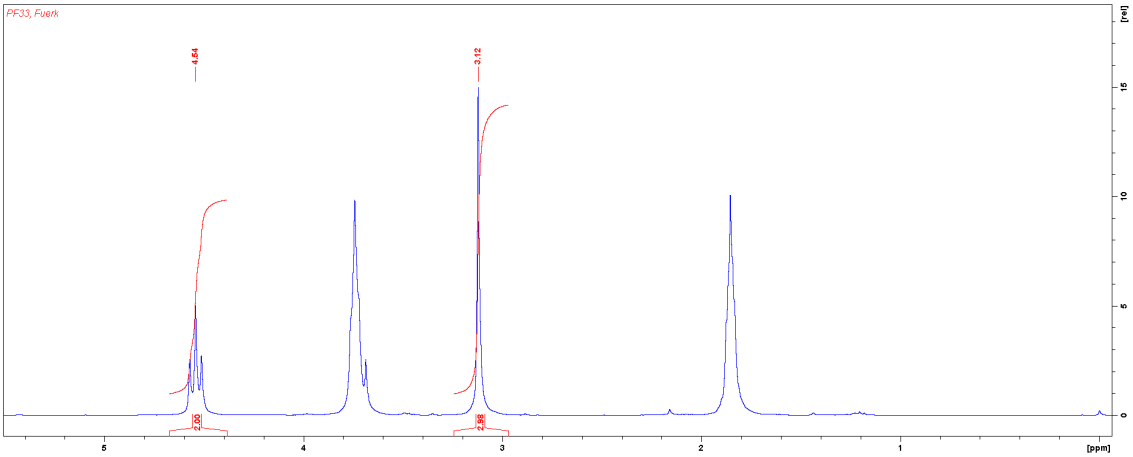

Figure 38: ^{1}H NMR spectrum (300 MHz, $CDCl_3$, TMS) of TEG_F-OMs

Linkers

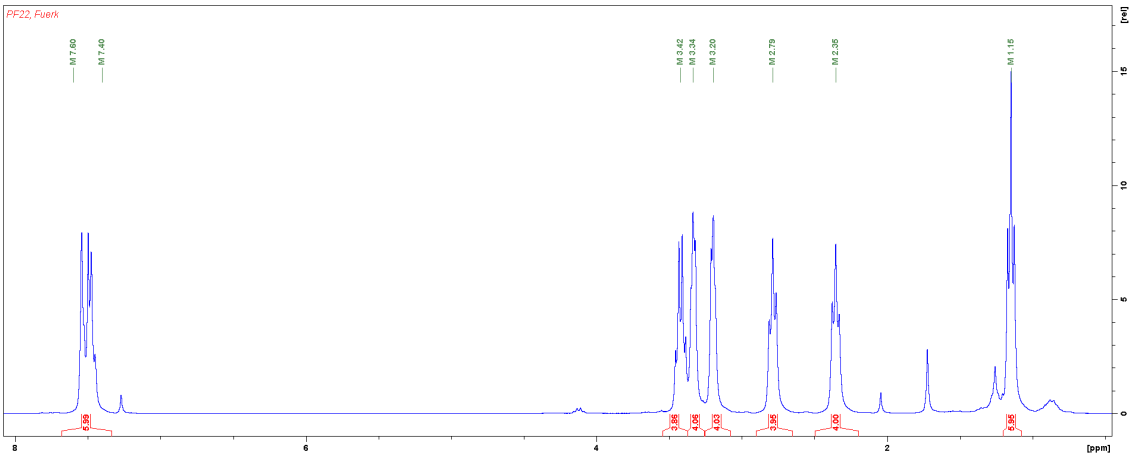

Figure 39: ^{1}H NMR spectrum (300 MHz, $CDCl_3$, TMS) of F(DEG)

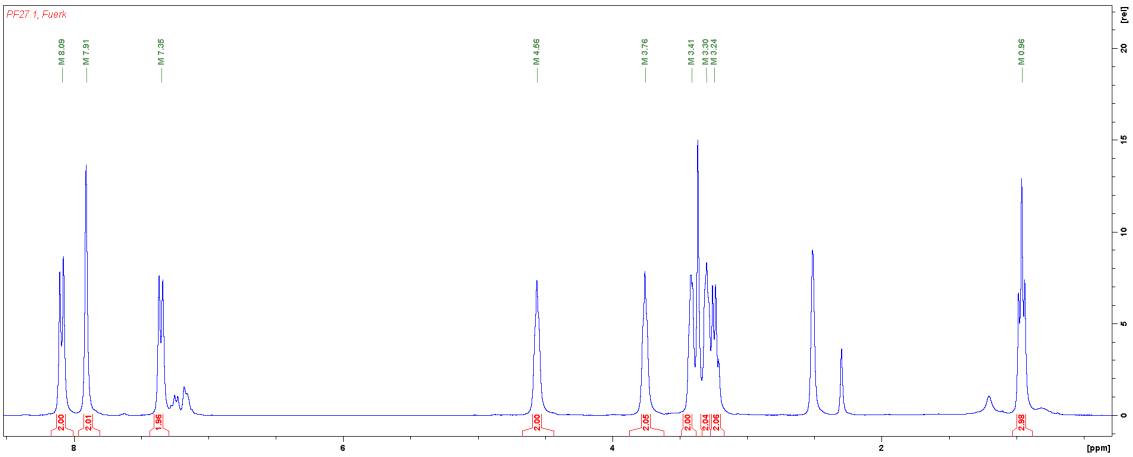

Figure 40: ^{1}H NMR spectrum (300 MHz, $(CD_3)_2SO$, TMS) of C(DEG)

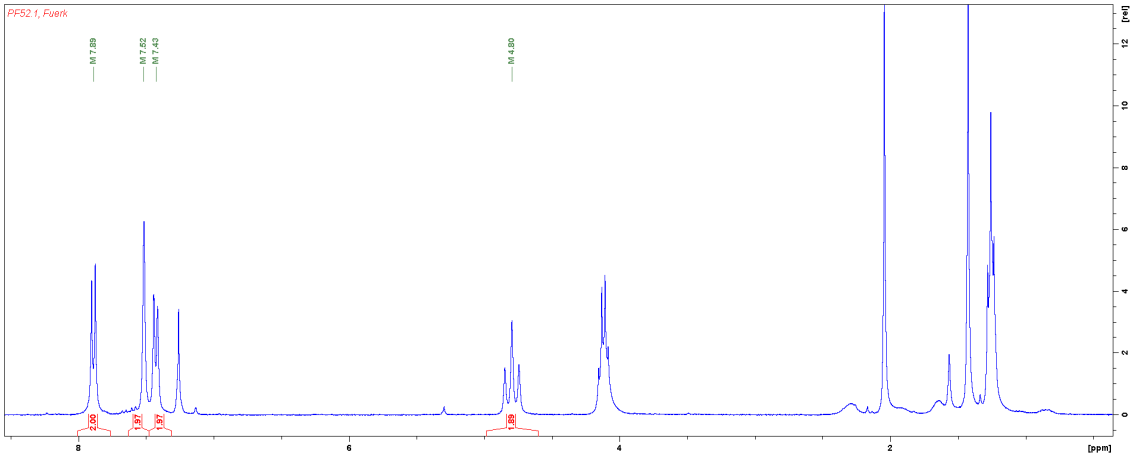

Figure 41: ^{1}H NMR spectrum (300 MHz, $CDCl_3$, TMS) of $C(Oct_F(2H))$

PMI Precursors

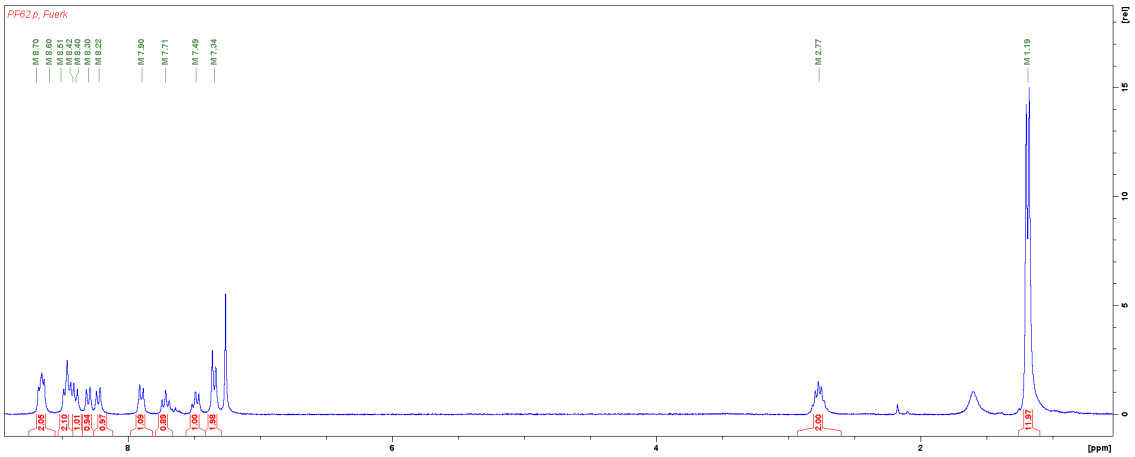

Figure 42: ^{1}H NMR spectrum (300 MHz, $CDCl_3$, TMS) of PMI-Br

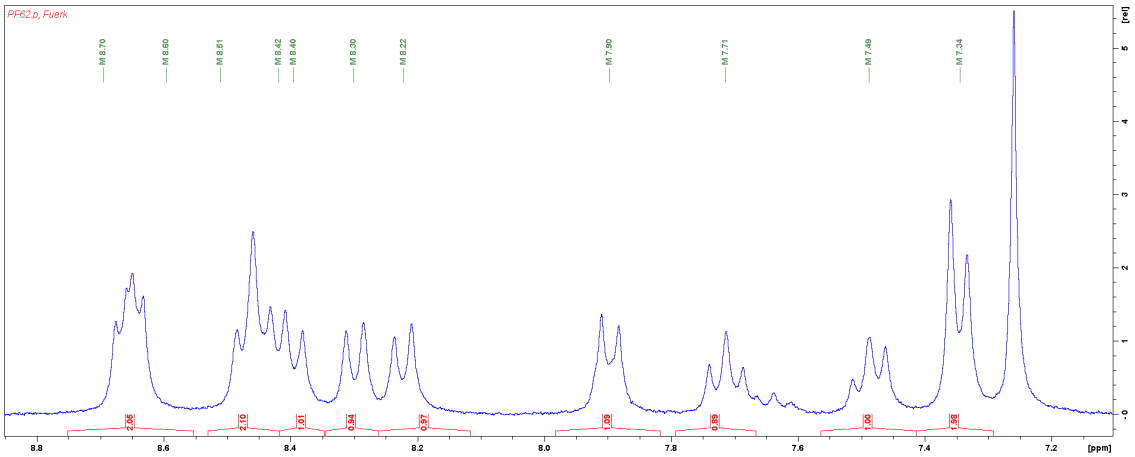

Figure 43: ^{1}H NMR spectrum (300 MHz, $CDCl_3$, TMS) of PMI-Br, aromatic region

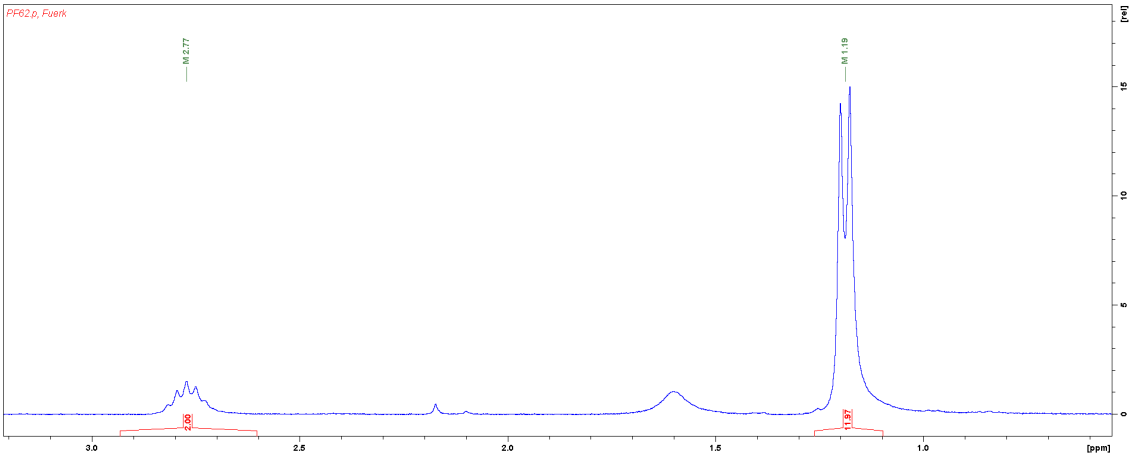

Figure 44: ^{1}H NMR spectrum (300 MHz, CDCl3, TMS) of PMI-Br, aliphatic region

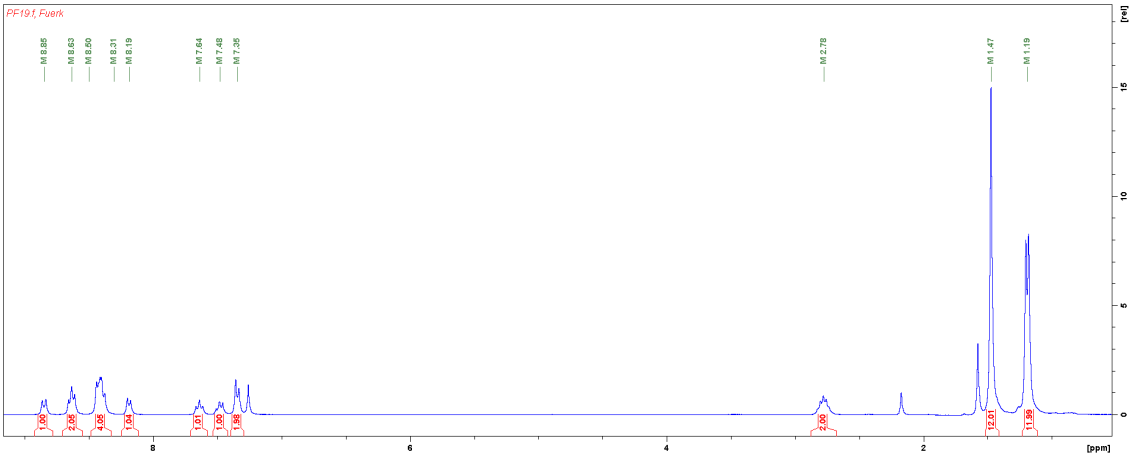

Figure 45: ^{1}H NMR spectrum (300 MHz, CDCl3, TMS) of PMI-Bpin

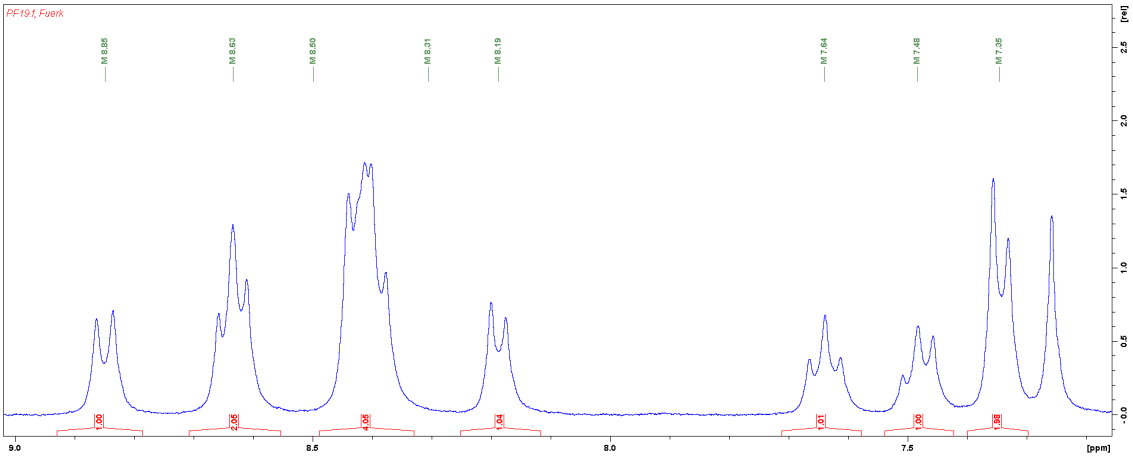

Figure 46: ^{1}H NMR spectrum (300 MHz, CDCl3, TMS) of PMI-Bpin, aromatic region

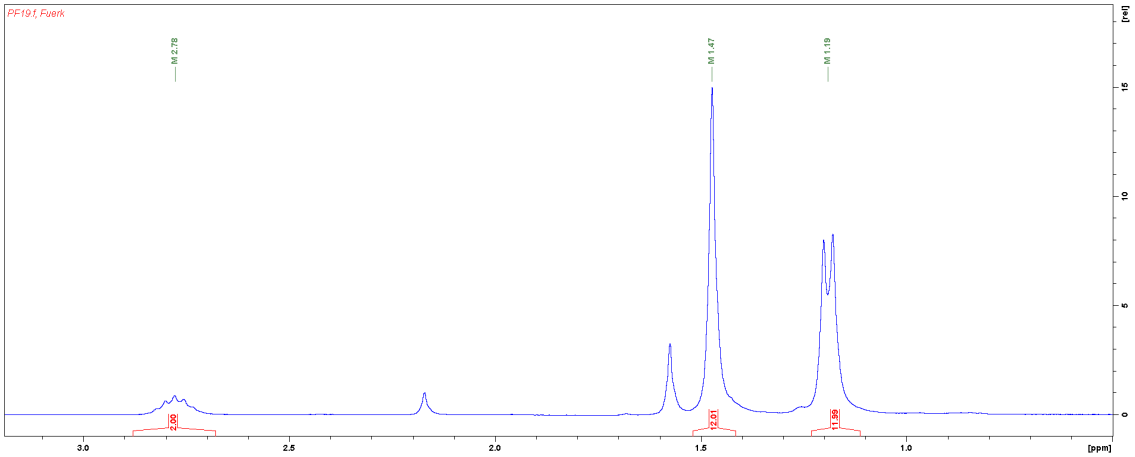

Figure 47: ^{1}H NMR spectrum (300 MHz, $CDCl_3$, TMS) of PMI-Bpin, aliphatic region

A-D-A Compounds

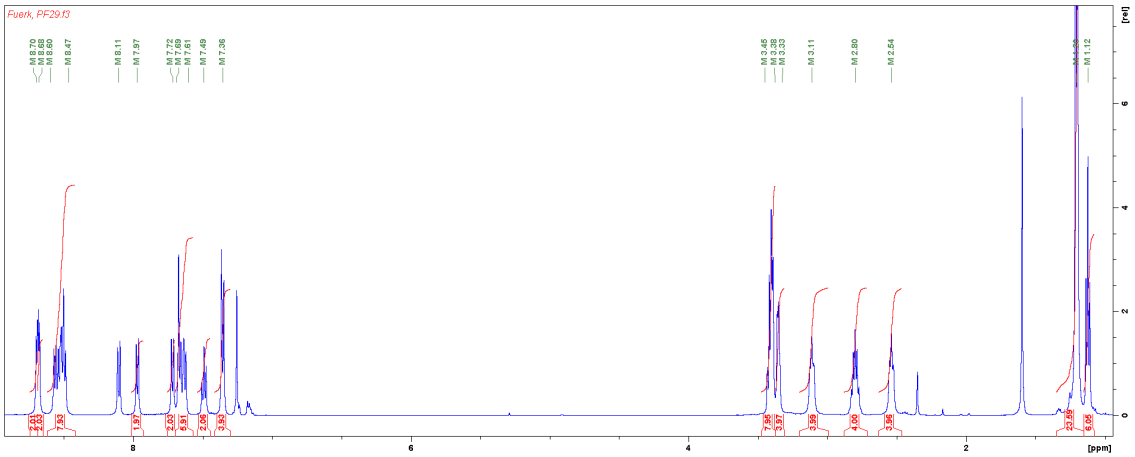

Figure 48: ^{1}H NMR spectrum (500 MHz, $CDCl_3$, TMS) of PMI-F(DEG)-PMI

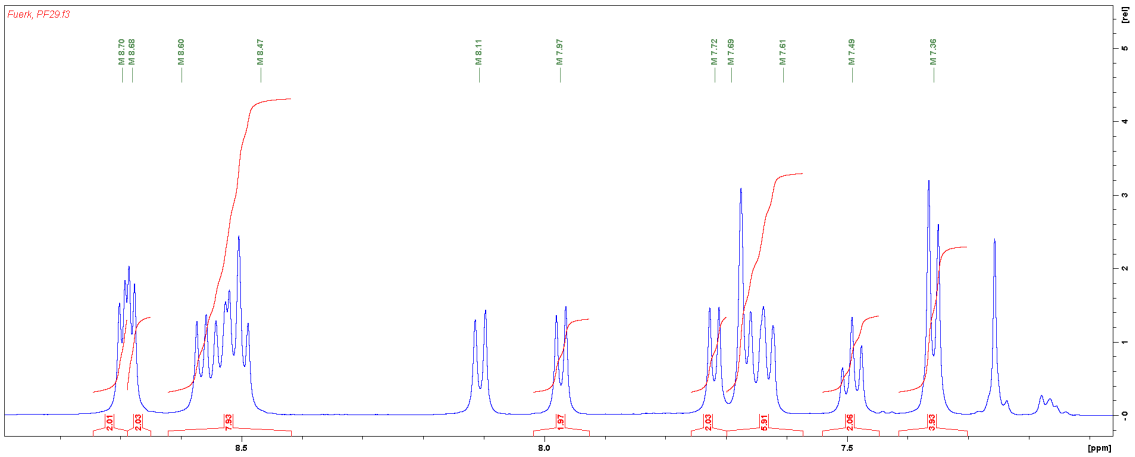

Figure 49: ^{1}H NMR spectrum (500 MHz, $CDCl_3$, TMS) of PMI-F(DEG)-PMI, aromatic region

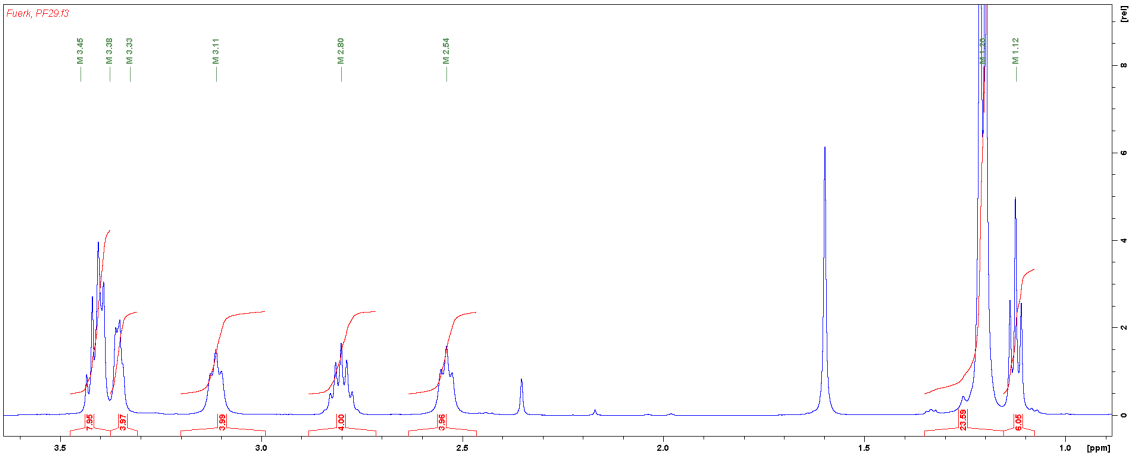

Figure 50: ^{1}H NMR spectrum (500 MHz, $CDCl_3$, TMS) of PMI-F(DEG)-PMI, aliphatic region

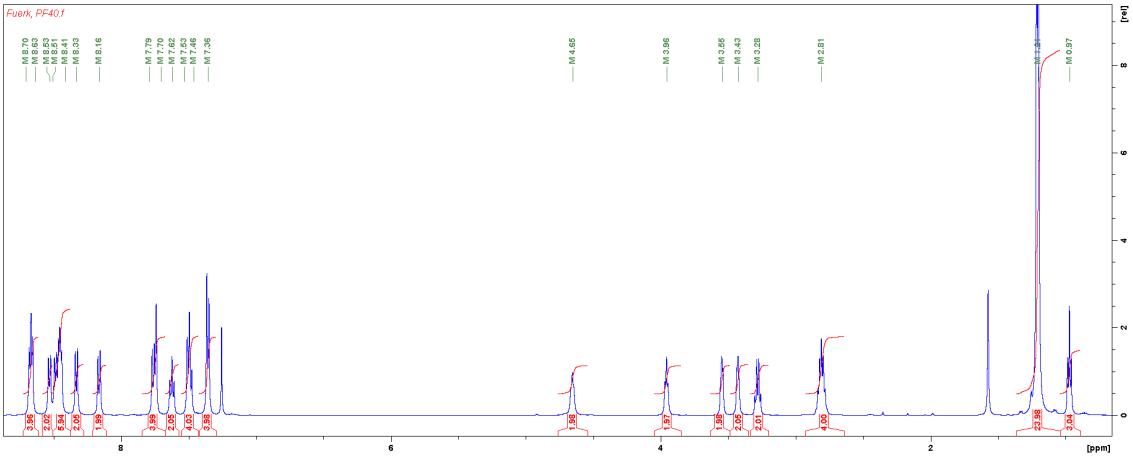

Figure 51: ^{1}H NMR spectrum (500 MHz, $CDCl_3$, TMS) of PMI-C(DEG)-PMI

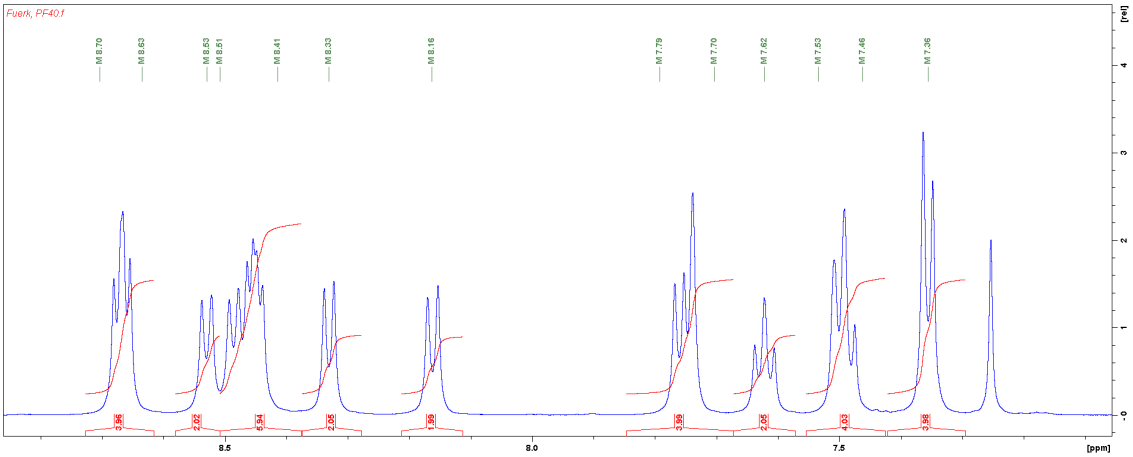

Figure 52: ^{1}H NMR spectrum (500 MHz, $CDCl_3$, TMS) of PMI-C(DEG)-PMI, aromatic region

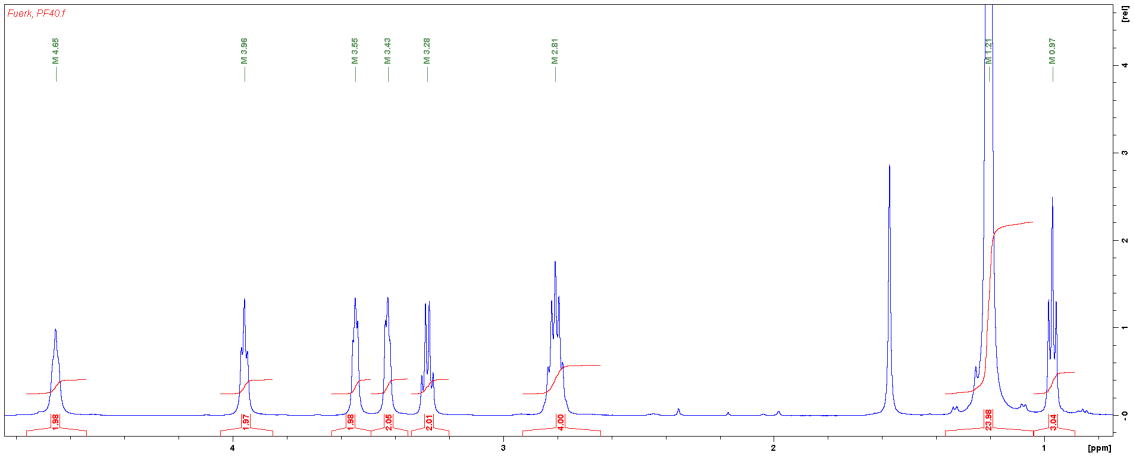

Figure 53: ^{1}H NMR spectrum (500 MHz, $CDCl_3$, TMS) of PMI-C(DEG)-PMI, aliphatic region

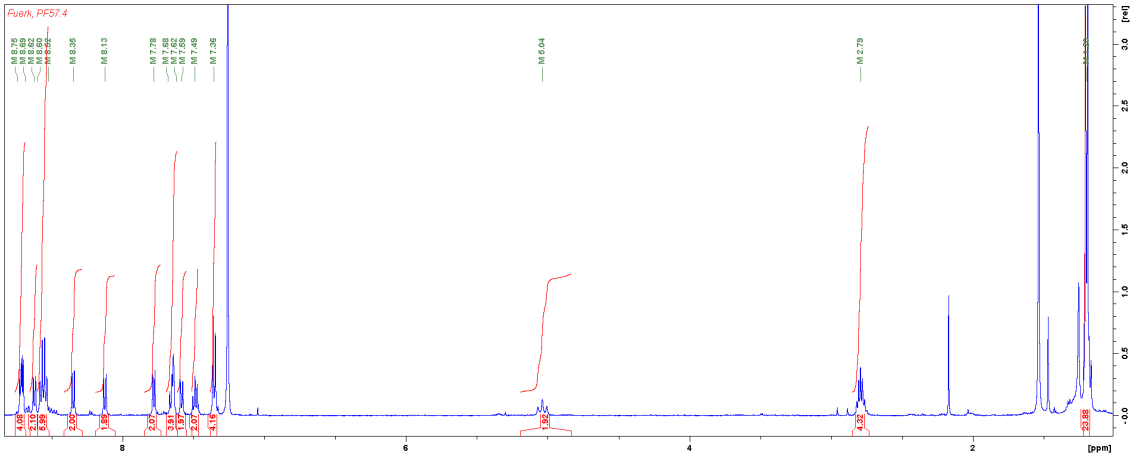

Figure 54: ^{1}H NMR spectrum (500 MHz, $CDCl_3$, TMS) of PMI-C(Oct_F(2H))-PMI

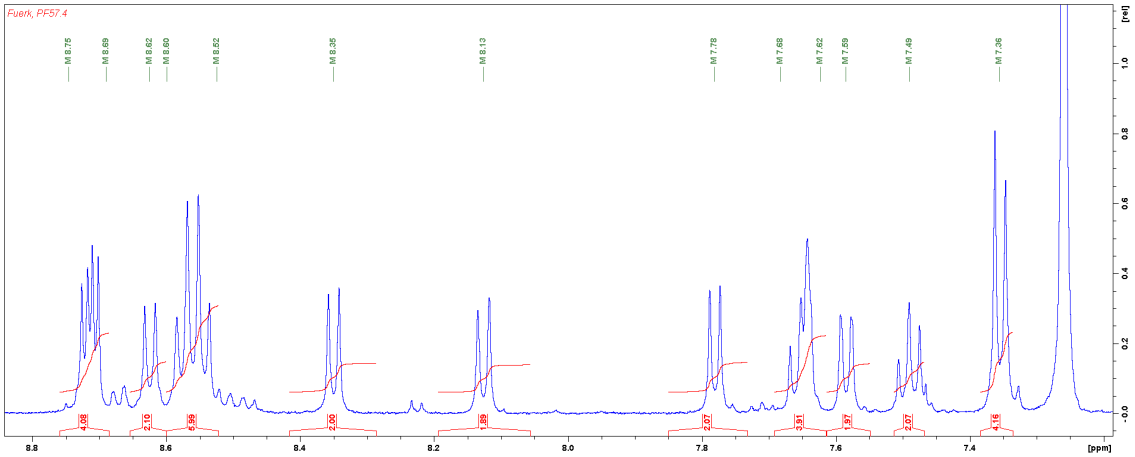

Figure 55: ^{1}H NMR spectrum (500 MHz, $CDCl_3$, TMS) of PMI-C(Oct_F(2H))-PMI, aromatic region

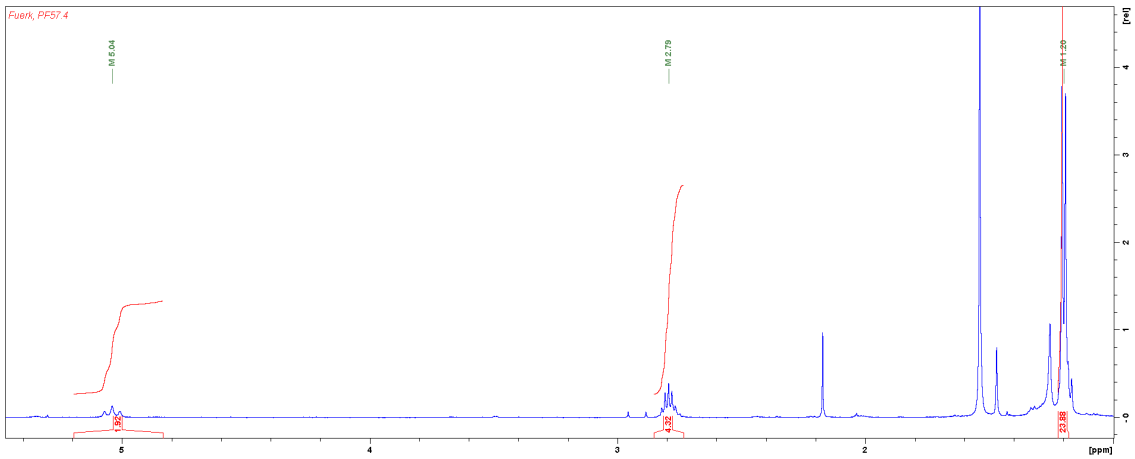

Figure 56: ^{1}H NMR spectrum (500 MHz, $CDCl_3$, TMS) of PMI-C(Oct_F(2H))-PMI, aliphatic region

Mass Spectrometry

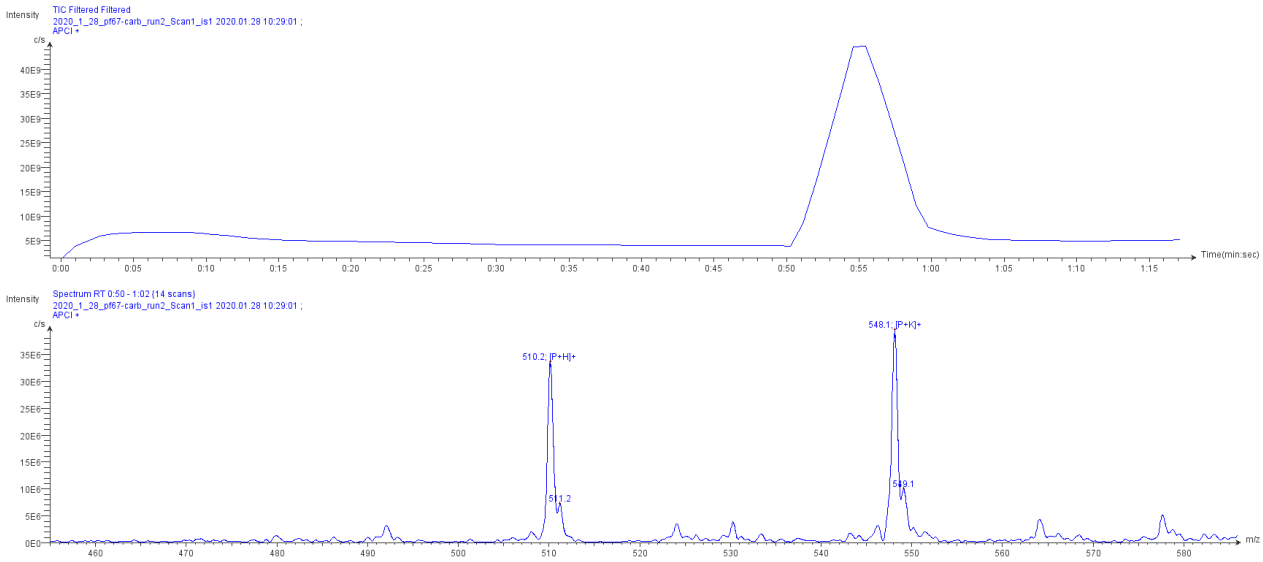

Figure 57: APCI-MS spectrum of carbazole with triple bond.

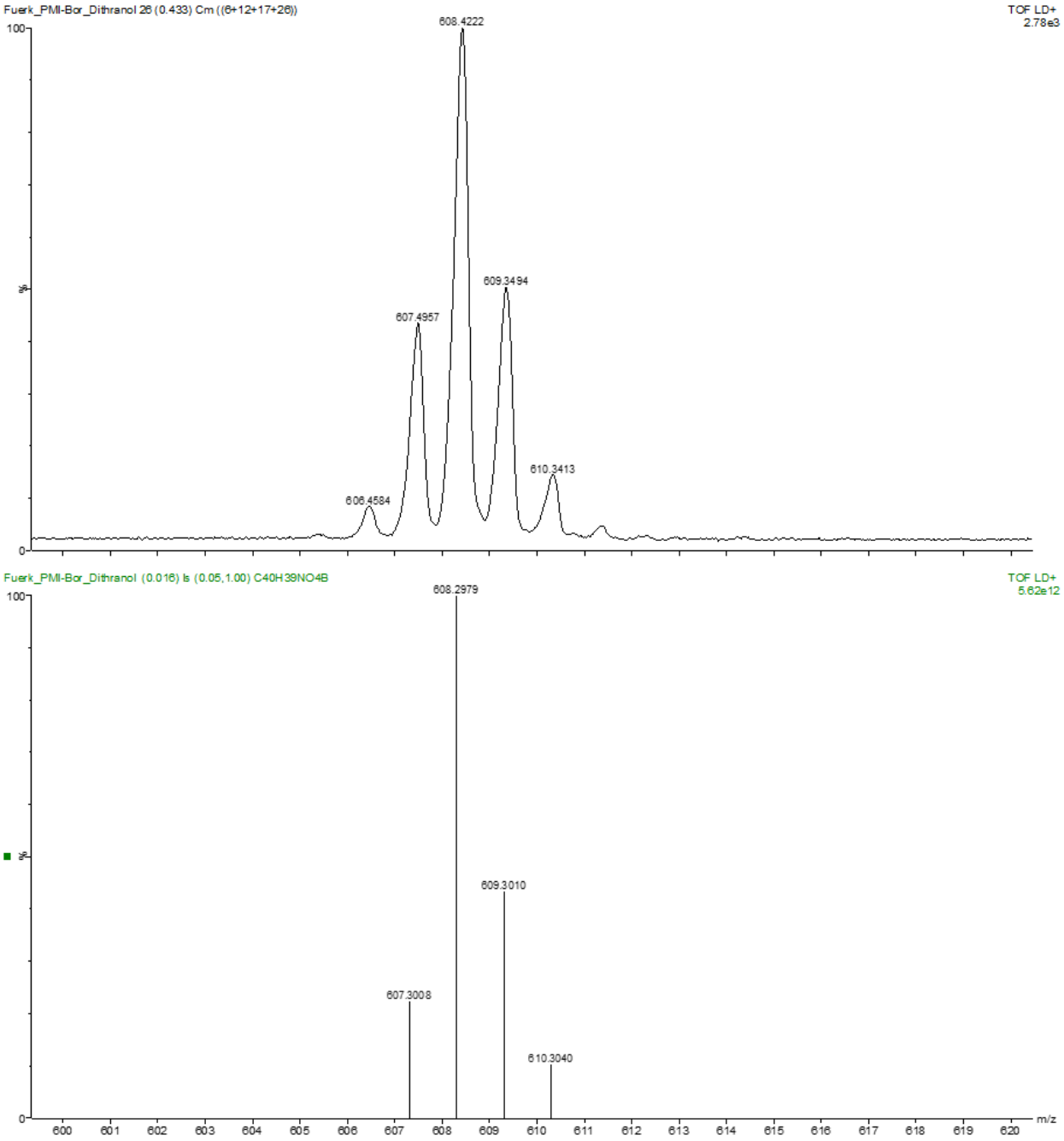

Figure 58: HR-MS spectrum of PMI-Bpin, matrix: dithranol.

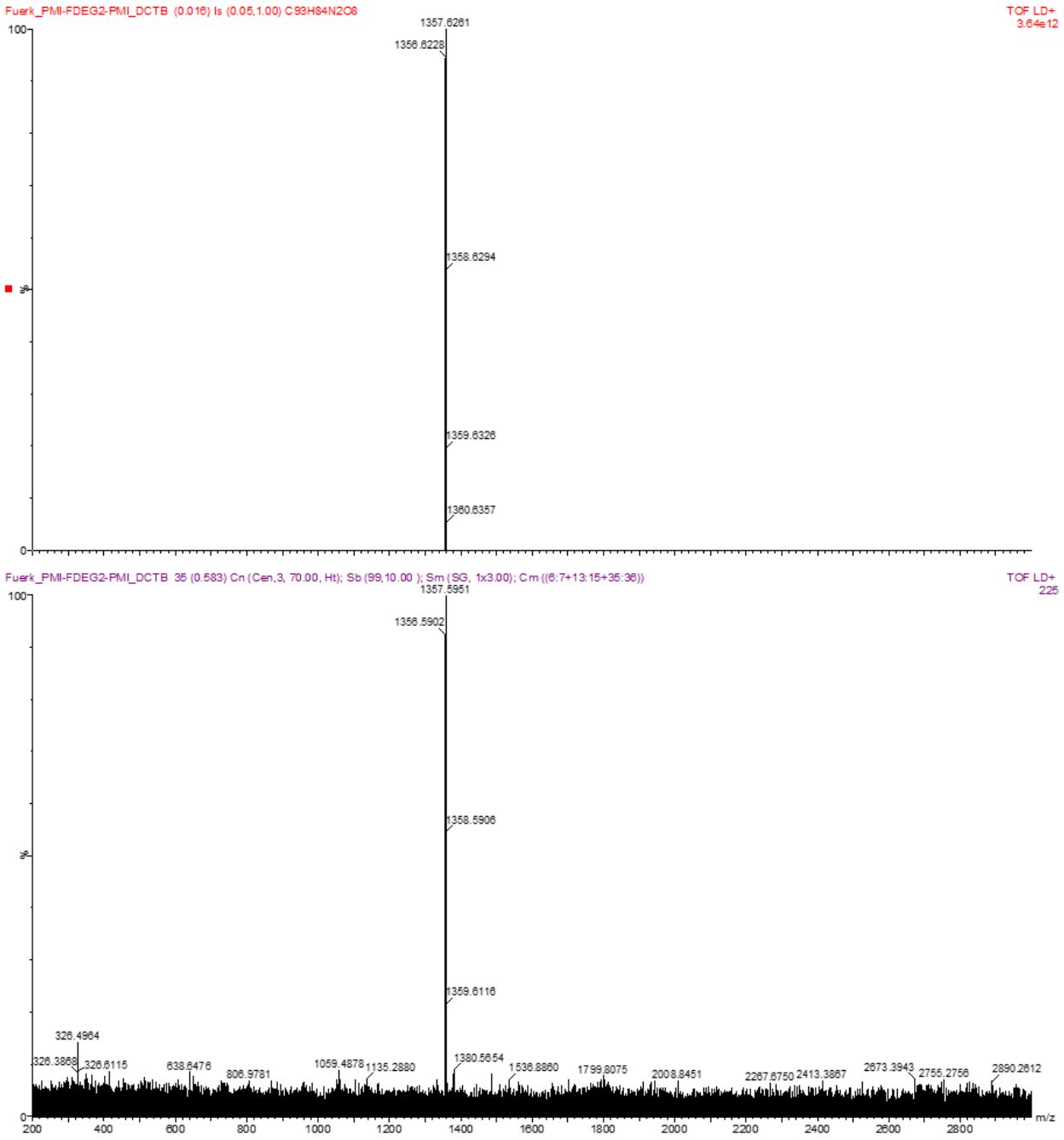

Figure 59: HR-MS spectrum of PMI-F(DEG)-PMI, matrix: DCTB.

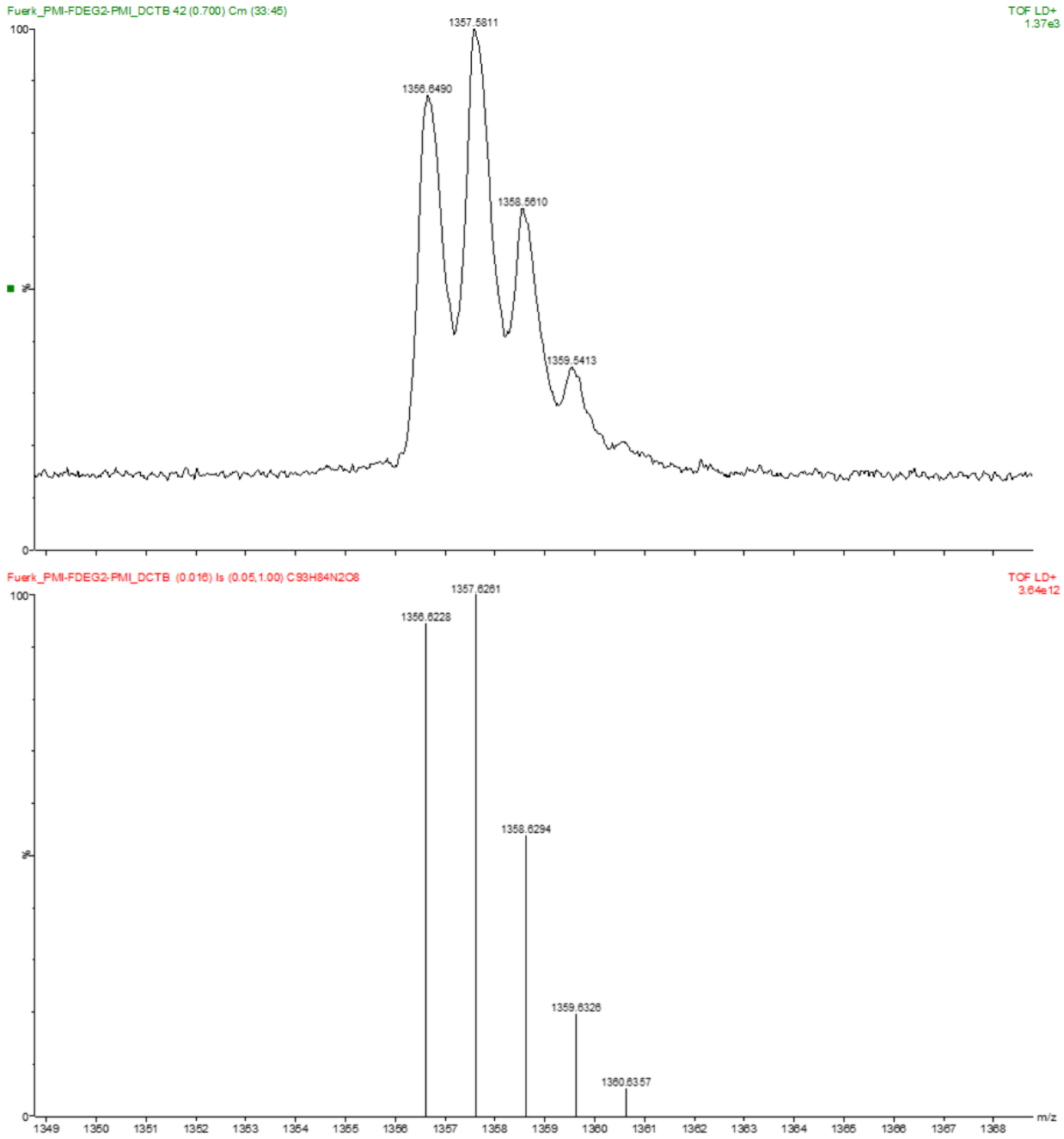

Figure 60: HR-MS spectrum of PMI-F(DEG)-PMI (zoomed to product peak), matrix: DCTB.

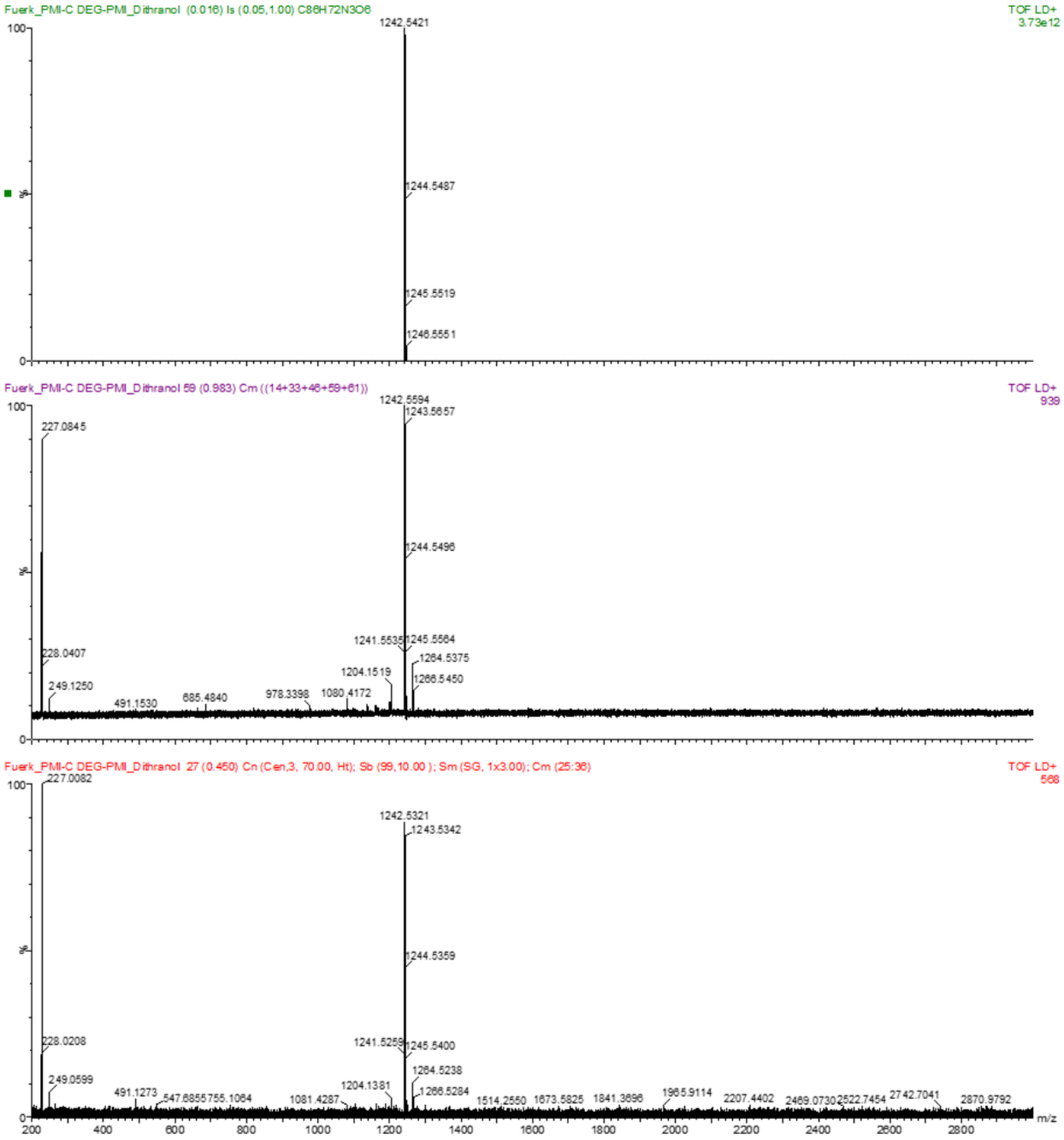

Figure 61: HR-MS spectrum of PMI-C(DEG)-PMI, matrix: dithranol.

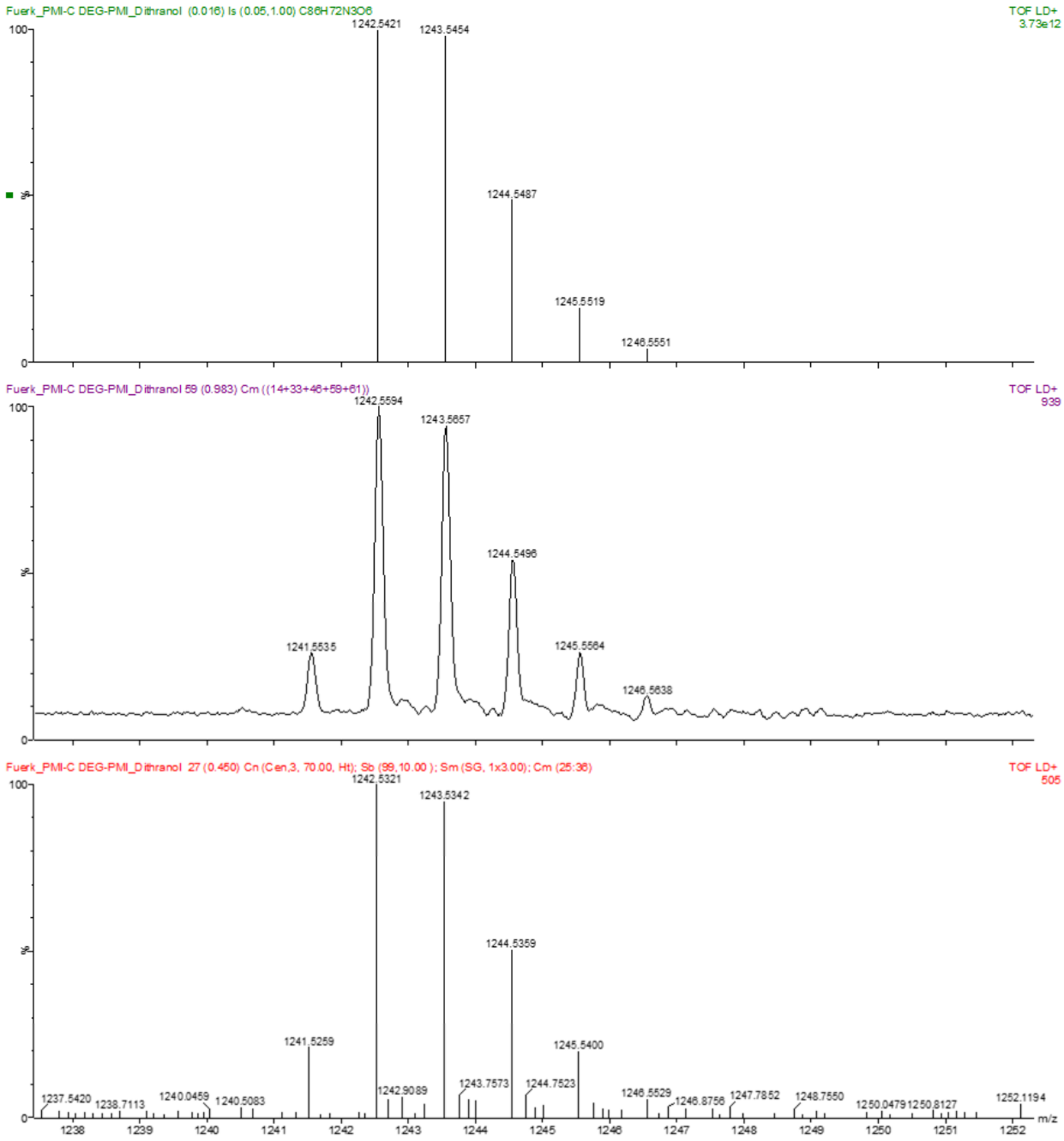

Figure 62: HR-MS spectrum of PMI-C(DEG)-PMI (zoomed to product peak), matrix: dithranol.

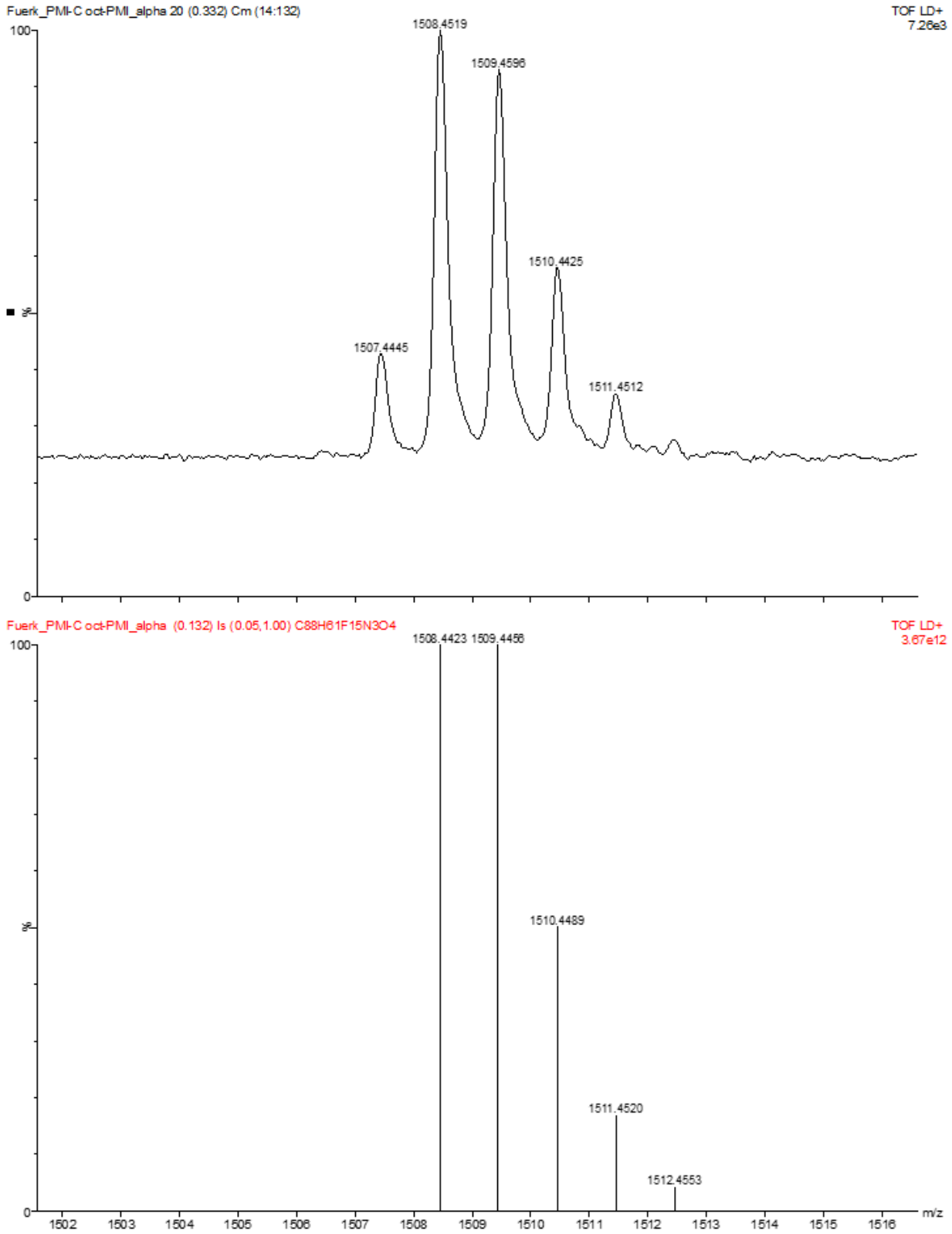

Figure 63: HR-MS spectrum of PMI-C($\mathrm{Oct_F}$(2H))-PMI, matrix: alpha.

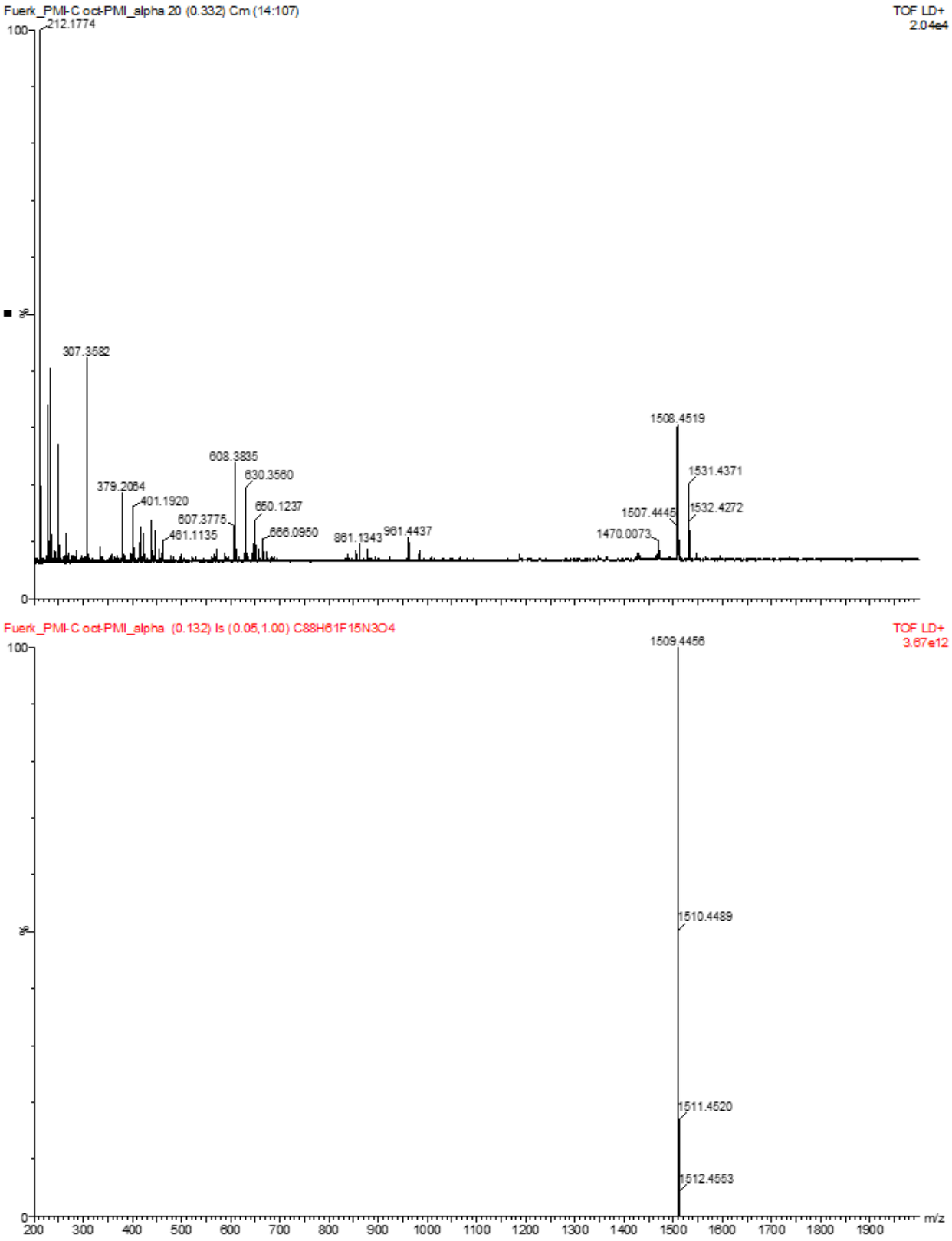

Figure 64: HR-MS spectrum of PMI-C($\mathrm{Oct_F}$(2H))-PMI (zoomed to product peak), matrix: alpha.

Infrared Spectroscopy

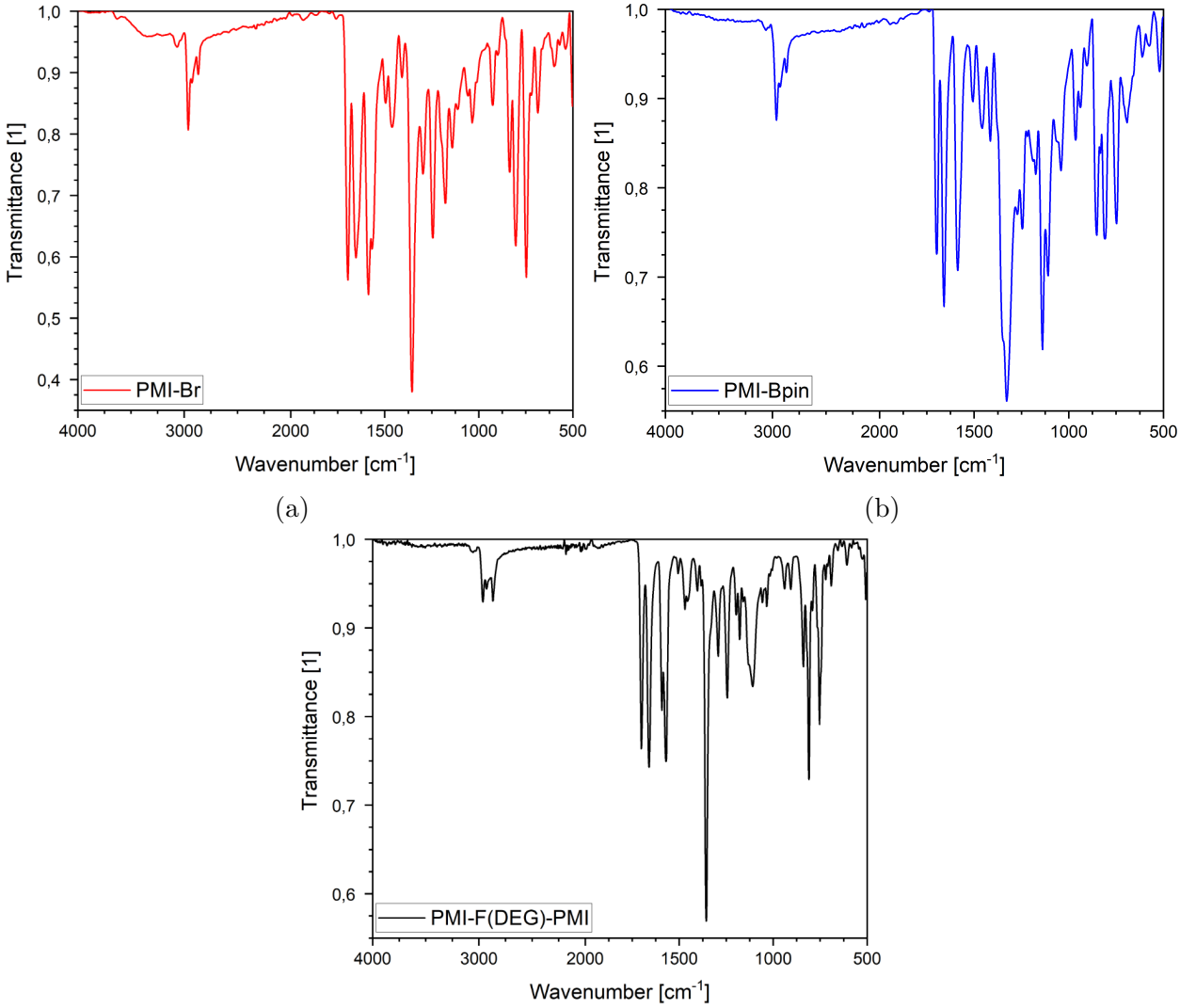

Figure 65: FT-IR spectra of (a) PMI-Br, (b) PMI-Bpin, (c) PMI-F(DEG)-PMI.